SISSA
Scuola
Internazionale
Superiore di
Studi Avanzati

Neuroscience Area – PhD course in

Neurobiology

Complexity and Versatility of Calcium Signaling and Dynamics

Candidate:

Yunzhen Li

Supervisor:

Vincent Torre

Co-supervisor:

Dan Cojoc

Academic Year 2017-21

Complexity and Versatility of Calcium Signaling and Dynamics

SISSA PhD thesis in Neuroscience by

Yunzhen Li

Supervisor

Prof. Vincent Torre

Co-supervisor

Dan Cojoc

DECLARATION

I hereby declare that this thesis represents my own work which has been done as a PhD candidate at the International School for Advanced Studies (SISSA), Trieste Italy, between November 2017 and September 2021.

This thesis is a presentation of my original research work. Wherever contributions of others are involved, every effort is made to indicate this clearly, with due reference to the literature, and acknowledgement of collaborative research and discussions.

Signature: Yunzhen Li

Date: 2021/09

Abstract

The calcium ion is a universal second messenger mediating a wide range of dynamic cellular functions, such as exocytosis, contraction, transcription, and proliferation. A hallmark of calcium signaling is the transient pulsing dynamics of cytosolic calcium concentration, which is versatile tool regulating cellular processes.

The aim of this thesis is to study the calcium signals and dynamics primarily related to mechanotransduction within rod photoreceptors, primary hippocampal neurons and glioblastoma (GBM) cells.

To study calcium dynamics in rods of Xenopus laevis, which are composed of an inner segment, IS and an outer segment, OS (IS+OS), we used the fluorescent calcium dye CaSiR-1 AM working in the near-infrared (NIR) (excitation at 650 and emission at 664 nm), which allowed us investigate calcium dynamics with an unprecedented accuracy and most importantly in semi dark-adapted conditions. The experiments showed: there are spontaneous calcium flares in functional OSs, and these flares are highly localized and are more pronounced at the OS tip; a bright flash of light at 488 nm induces a drop in intracellular calcium concentration at the OS base but often a flare at the OS tip.

We also have investigated mechanosensitivity in the rods by combining electrophysiology, optical tweezers (OTs),and biochemistry, and we show that mechanical stimulation of the order of 10 pN applied briefly to either the OS or IS evokes calcium transients. The pN force evoked calcium transients can be inhibited by application of GsMTx-4 whereas spontaneous calcium flares can be seen at tip of OS.

In primary hippocampal neurons, we employed an Oscillatory Optical Tweezers (OOT) to exert a local indentation with pN forces. We found that single local indentation evokes a transient intracellular calcium change, whereas repeated mechanical stimulations induce a more sustained and variable calcium response, which can be inhibited by the GsMTx-4 treatment. Moreover, we observed a mechanically evoked activation of the CaMKII and small G protein RhoA.

Lastly, with glioblastoma cells, we investigated the calcium flares and its

coupling with chloride dynamics in both flat and round GBM cells undergoing the mitosis primarily by using multi-channels imaging of calcium and chloride, ratiometric calcium imaging. The preliminary data showed that in normal flat cells, global calcium flares can last stably for at least one hour without significantly changing the morphology of the cell, and more importantly are able to activate chloride signals which can be unexpectedly localized. And within round cells undergoing mitosis, instead of finding calcium flares at the initial phase before the cell divides into two, calcium flares were frequently seen at the end of mitosis, which can be further increased by Piezo 1 agonist Yoda 1 to activate favorable chloride influx signals.

Introduction

I. Aims and Achievements

The universality of calcium as an intracellular messenger depends on its enormous versatility. Versatile intracellular signals operate over a wide temporal range to regulate many different cellular processes that span time scales from microseconds to hours. A basic hallmark of calcium signalling is transient dynamics of cytosolic calcium concentration. Cells have a calcium signalling toolkit with many components that can be integrated to create a wide range of spatial and temporal signals. This versatility is exploited by cells to control diverse processes.

Motivated by the versatility of calcium signaling and dynamics, this thesis focuses on exploring the calcium signals and dynamics within different types of CNS cells primarily using calcium imaging techniques combining with newly developed tools, trying to update our knowledge regarding distinct cellular processes. The calcium signals and dynamics within rod photoreceptors, primary hippocampal neurons and glioblastoma cells were investigated and discussed, separately and respectively in this PhD thesis:

1. Rod photoreceptors

Rod photoreceptors are composed of a soma and an inner segment (IS) connected to an outer segment (OS) by a thin cilium. OSs are composed of a stack of ~800 lipid discs surrounded by the plasma membrane where phototransduction takes place*(PA Liebman et al. 1982 Methods Enzymol, JC Gilliam et al. 2012 Cell)*. Intracellular calcium plays a major role in phototransduction and is more concentrated in the discs, where it can be incorporated and released. To study calcium along the OS, we used CaSiR-1 AM (excitation 650 nm, emission 664 nm) and Fura Red (excitation 440 and 480 nm, emission ~650 nm); we analyzed its intracellular dynamics in dissociated rod photoreceptors composed of an IS and an OS (IS+OS) and in small pieces of retina obtained from Xenopus laevis frogs. CaSiR-1 increases fluorescence emission upon binding calcium, while Fura Red decreases its emission following binding to calcium. The excitation with Fura Red at two wavelengths allows a quantitative estimation of intracellular calcium by what is referred to as ratiometric calcium imaging. Conversely, CaSiR-1 AM allows the study of calcium dynamics in rods under semidark-adapted conditions. Additionally, with CaSiR-1 AM, we also have investigated mechanosensitivity in

the rods by combining electrophysiology, optical tweezers (OTs),and biochemistry.

The experiments showed: there are spontaneous calcium flares in functional OSs, and these flares are highly localized and are more pronounced at the OS tip; a bright flash of light at 488 nm induces a drop in intracellular calcium concentration at the OS base but often a flare at the OS tip; Mechanical stimulation of the order of 10 pN applied briefly to either the OS or IS evokes calcium transients. The pN force evoked calcium transients can be inhibited by application of GsMTx-4 whereas spontaneous calcium flares can be seen at tip of OS.

2. Primary hippocampal neurons

Neurons have been believed to interact with each other primarily through chemical and electrical signalling. However, there exist also sensory neurons specialized to transduce mechanical stimuli, which underlies hearing, mechanical sensation and pain *(EA Lumpkin et al. 2007 Nature, N Grillet et al. 2009 Sci Signal)*. Recent investigations have shown that mechanosensitive channels (MSCs) are found almost ubiquitously in cells and tissues *(J Hao et al. 2011 Nat Protoc)*, suggesting that mechanosensitivity is widespread in the nervous system. It has been previously shown in our lab that filopodia and lamellipodia of neurons of the central nervous system exert small forces in the range of 2-50 pN. It is important, therefore, to establish whether central nervous neurons are able to sense forces in the same range of amplitude and in this case mechanical signalling could play a major role in the development and operation of neuronal networks.

Recently, our lab developed an optical tweezer (OT) method based on a tunable optical trap to apply forces in the 5-50-pN range and to measure the indentation produced in the cell and triggering changes in intracellular calcium. Here, to verify whether neurons of the central nervous system respond to mechanical stimulations comparable to those exerted by filopodia and lamellipodia and we applied mechanical forces in the range of 10-50 pN to dissociated hippocampal neurons.

We found that single local indentation evokes a transient intracellular calcium change, whereas repeated mechanical stimulations induce a more sustained and variable calcium response, which can be inhibited by the GsMTx-4 treatment. Moreover, we observed a mechanically evoked activation of the CaMKII and small G protein RhoA.

3. Glioblastoma cells

GBM has a high proliferative capacity. Genetic changes in the growth signaling that impair tightly regulated normal cell homeostasis has been widely accepted as the fundamental reason, leading to transformation of normal cells into malignant type with uncontrolled proliferative potential *(N Prevarskaya et al. 2010 Trends Mol Med)*. In this respect, ion channels were considered to play a pivotal role in tumor biology and are involved in regulation of tumor cell characteristics like uncontrolled growth *(VA Cuddapah et al. 2011 Am J Physiol Cell Physiol)*, while it suggested abnormal calcium signals and dynamics plays an important role in the uncontrolled growth *(GR Monteith et al. 2017 Nat Rev Cancer)*. On the other respect, several lines of evidence suggest that chloride (Cl^-) and potassium (K^+) channels have a major role in cell volume shrinking and swelling, fundamental steps during mitosis and replication *(CW Habela et al. 2007 Cell Cycle)*.

We have previously shown the existence of calcium flares in GBM *(X Li et al. 2020 J Cell Sci)*, we hypothesized that calcium flares and Cl^- channels could play an important role during GBM migration and mitosis. In this thesis, we are trying to investigate their roles, by using multi-channel imaging of calcium and chloride, ratiometric calcium imaging, and additionally, electrophysiological methods.

The preliminary data showed that in normal flat cells, global calcium flares can last stably for at least one hour without significantly changing the morphology of the cell, and more importantly are able to activate chloride signals which can be unexpectedly localized. And within round cells undergoing mitosis, instead of finding calcium flares at the initial phase before the cell divides into two, calcium flares were frequently seen at the end of mitosis, which can be further increased by piezo 1 agonist Yoda 1 to activate favorable chloride influx signals.

II. Research Background

1 Explorations of Calcium in Biology

1.1 Free Ionized calcium

Calcium, the 20th element in the periodic table, is the fifth most abundant element in the Earth's crust and seawater, and the single most abundant mineral in the human body *(GS Baird 2011 Clin Chim Acta)*. The adult human body contains up to 1 kg of calcium, distributed primarily in the bones as hydroxyapatite *(DH Marxhall et al. 1976 Proc Nutr Soc)*. Although most of calcium element is stably sequestered into skeleton, a small fraction readily exchanges with the body's soluble calcium fraction, which resides primarily in the extracellular fluid, with approximately equal concentrations in serum and interstitial fluids. Its location and concentration in the mammalian body are closely regulated *(GS Baird 2011 Clin Chim Acta)*. This soluble calcium is usually termed as ionized calcium, which exists in two different forms, namely, bound ionized calcium and free ionized calcium, **free calcium or Ca^{2+}** for short. The blood plasma concentration of ionized calcium is ~2.5 mM, approximately half of which is bound, largely to blood proteins including mainly albumin. Thus, extracellular free calcium concentration, $[Ca^{2+}]_{ex}$ is closely regulated at around 1.2 mM *(F Bronner 2001 ScientificWorldJournal)*.

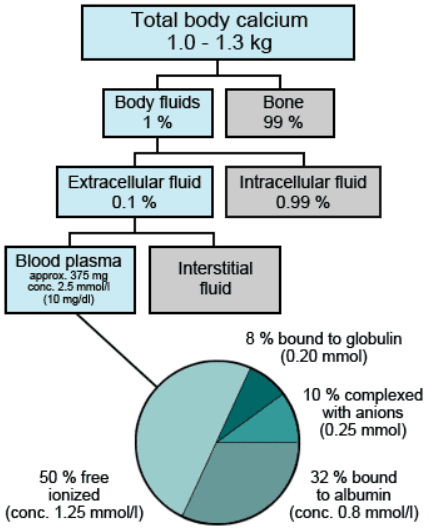

Fig. 1 Distribution of Calcium in Human Body [Image from online website: https://acutecaretesting.org/en/articles/ionized-calcium]

Within single cell, intracellular free calcium concentration, usually referring to Ca^{2+} in cytosol, $\mathbf{[Ca^{2+}]_i}$ is generally 10^4 times lower than extracellular free calcium concentration, typically, around 100nM at rest. While the concentrations inside specific intracellular compartments can differ quite markedly. The endoplasmic reticulum (ER) or sarcoplasmic reticulum (SR) in striated muscles is the largest Ca^{2+} store in the cell. The Ca^{2+} concentration in endoplasmic reticulum, $\mathbf{[Ca^{2+}]_{ER}}$ can reach ~1 mM, varying in the 200–2000μM range depending on the cell type, 10^3 or 10^4 times above cytosolic $[Ca^{2+}]_i$. Similarly, Ca^{2+} concentration in the Golgi apparatus at resting, $\mathbf{[Ca^{2+}]_{GA}}$ is as well maintained at ~0.3 mM, varying in the 200–2000μM range depending on physiological conditions ***(P Pinton et al. 1998 EMBO J, L Arenillas et al. 2016 J Clin Oncol)***. In general smooth cells, the concentration of Ca^{2+} in mitochondrial matrix, $\mathbf{[Ca^{2+}]_m}$ is within the range of 100-200nM at rest, which can be increased up to 10-500 μM when the cell is activated ***(Z Xu et al. 2016 Curr Genomics)***. The Ca^{2+} concentration in lysosome lumen, $\mathbf{[Ca^{2+}]_{ly}}$ is estimated to be about 500 μM ***(S Patel et al. 2015 Cell Calcium)***. Nucleus $\mathbf{[Ca^{2+}]_n}$ and cytosolic $[Ca2^+]_i$ are similar under resting conditions while under some active condition, $[Ca^{2+}]_n$ was shown to be higher than $[Ca^{2+}]_i$ ***(M Brini et al. 1999 Microsc Res Tech)***. Additionally, regarding comparison between Ca^{2+} and other physiological ions, please refer to the table below.

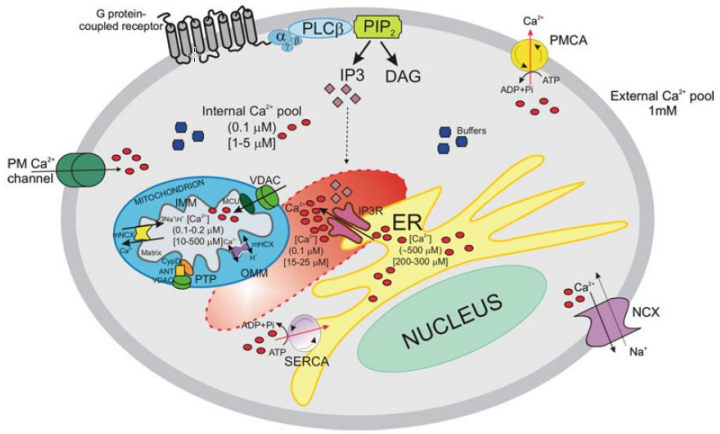

*Fig. 2 Distribution of intracellular Ca^{2+} [Image from the paper: **(Z Xu et al. 2016 Curr Genomics)**]*

ion conc. (mM)	sea water	*E. coli*	*S. cerevisiae*	mammalian cell (heart or RBC)	blood plasma
K^+	≈10	30-300	300	100	4
Na^+	≈500	10	30	10	100-200
Mg^{2+}	≈50	30-100 (bound); 0.01-1 (free)	50	10 (bound) 0.5 (free)	1
Ca^{2+}	≈10	3 (bound);100 nM (free)	2 (bound)	10-100 nM (free)	2
Cl^-	≈500	10–200 media dependent		5-100	100

Table 1 Concentration of Ca^{2+} and other physiological ions from different system [Data from http://book.bionumbers.org/what-are-the-concentrations-of-different-ions-in-cells/]

1.2 Signaling calcium

The landmark revealing the role of calcium as signaling ion was made by Sidney Ringer in 1883, who studied the contraction of isolated rat hearts and serendipitously found it necessary to add Ca^{2+} salts into the suspension medium to maintain contraction ***(S Ringer 1883 J Physiol)***. From then on, Ca^{2+}, exclusively considered as a structural element previously, could, more importantly, be carrier of signals that initiated heart contraction.

However, until in 1947, the specific role of Ca^{2+} as an intracellular cation was clearly shown by Heilbrunn and Wiercinski who found only injecting Ca^{2+} other than Na^+, K^+ or Mg^{2+} into frog muscles can initiate their contraction ***(LV Heilbrunn et al. 1947 J Cell Comp Physiol)***, which was further confirmed by the first use of Ca^{2+} chelator which can remove intracellular Ca^{2+} ***(E Bozler 1954 J Gen Physiol)***. Then, several important discoveries come into sight: 1, the binding of Ca^{2+} to myofibrils activated actomyosin. 2, isolated sarcoplasmic reticulum vesicles accumulated Ca^{2+} by using an ATP-energized system. 3, Ca^{2+} interacts troponin C, mediating myofibrillar contraction ***(S Ebashi 1961 J Chir (Paris), W Hasselbach et al. 1961 Biochem Z, S Ebashi et al. 1962 J Cell Biol, S Ebashi et al. 1965***

J Biochem).

Since then, these early discoveries above have elicited the increase of research on the signaling role of Ca^{2+}, from tens of published papers each year during early phase, to thousand papers each year at today's explosive phase. Ca^{2+} is now recognized as the most important signaling ion that accompanies cells throughout their entire lifespan, from their origin at fertilization, to their eventual demise at the end of the life cycle *(E Carafoli 2002 Proc Natl Acad Sci U S A)*.

How can ionized Ca^{2+} be evolved into signaling Ca^{2+}? Ca^{2+} is preferred as the versatile intracellular signaling ion especially to Ca^{2+}'s cousin, Mg^{2+}, which can be explained probably by the several reasons. Firstly, Ca^{2+} binds water much less tightly than Mg^{2+} and precipitates phosphate, which pushes cells to evolve ways to sequester this dangerous divalent, which reduces its cytosolic levels to sub micromolar. On the other hand, under low level of $[Ca^{2+}]_i$, Ca^{2+} is preferred by cells taking part in signal transduction due to its desirable binding energy. This contradictory characteristics of intracellular Ca^{2+}, as well as its chemical nature, could be the force driving cells develop methods to chelate, compartmentalize, or extrude it. Among them, plenty of cellular proteins have been evolved by cells to bind Ca^{2+}, termed **calcium binding proteins** with affinities varying from nM to mM, some of which simply buffer or lower Ca^{2+} levels, and others to trigger cellular processes *(DE Clapham 2007 Cell, AN Dodd et al. 2010 Annu Rev Plant Biol)*.

Then how can intracellular Ca^{2+} be chelated and sensed biologically? Ca^{2+} is usually coordinated by 6–8 oxygen atoms in its primary coordination sphere. Compared to the chemical chelator EDTA and EGTA which cage Ca^{2+} via a doublet of two amine and four carboxylate groups, binding to Ca^{2+} of natural Ca^{2+} binding proteins is mainly coordinated by the six to seven oxygen atoms of carboxyl and carbonyl groups (Fig. 3A) *(NC Strynadka et al. 1989 Annu Rev Biochem)*. The professional protein chelator of Ca^{2+} is the **EF-hand domain** (named after the E and F regions of parvalbumin) *(S Nakayama et al. 1994 Annu Rev Biophys Biomol Struct)*, which is present in hundreds of proteins. EF-hand helix-turn-helix motifs cage Ca^{2+} within a ~12 amino acid loop between two orthogonal α helices via negatively charged oxygen atoms (Fig. 3B). A variety of factors can affect the affinities of EF-hand domains for Ca^{2+} including critical amino acids in the Ca^{2+} binding loop and sidechain packing in the protein core. Calmodulin, an important intracellular Ca^{2+} sensor, has four EF-hand motifs, each with different affinities for Ca^{2+}, which are often increased by interaction with target proteins. When binding Ca^{2+}, the domains of calmodulin will change their conformations, which triggers calmodulin's Ca^{2+} sensor activities, for example, binding to a helical peptide from myosin light

chain kinase (Fig. 3B) and wrapping around basic amphipathic helices of proteins (Fig. 3C). Another common Ca^{2+} binding motif is termed as C2 domain (Fig. 3D), an ~120 amino acid segment, which binds Ca^{2+} in variable loops containing negatively charged amino acids. The scaffold is an antiparallel β sandwich with an exposed protein-interaction surface ***(W Cho et al. 2005 Annu Rev Biophys Biomol Struct, C Mathes 2007 Expert Opin Ther Targets)***.

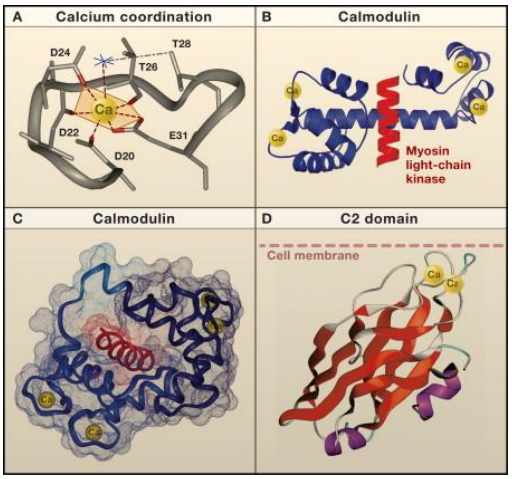

*Fig. 3 Oxygen Atoms of Amino Acids Chelate Ca^{2+} [Image from the paper:**(C Mathes 2007 Expert Opin Ther Targets)**]*

Finally, how can signaling Ca^{2+} be astonishingly versatile in sophisticated network of signaling pathways, which integrate information and regulate different cellular processes? Calcium signals usually take the form of **Ca^{2+} transient** increases in cytosolic free Ca^{2+} caused by the flux of Ca^{2+} into the cytosol either from the external medium or from subcellular compartments of higher Ca^{2+} compared with the cytosol. **Ca^{2+} dynamics** combined with different Ca^{2+} transients exist in different frequencies, durations, amplitudes and shapes, depending on the nature of the stimulus. From this perspective, stimulus specific spatio-temporal **$[Ca^{2+}]_i$ dynamics** enable the Ca^{2+} to encode stimulus-specific information as so-called calcium signature, and thus regulate processes that operate over a wide time range, from neurotransmitter release at the microsecond scale to gene transcription, which lasts for minutes and hours ***(MJ Berridge et al. 2003 Nat Rev Mol Cell Biol)***. Therefore, the plethora of diverse cellular functions or processes, typically, neuronal calcium functions, can be reflected and investigated by means of visualization and quantitative estimation of the intracellular calcium signals or $[Ca^{2+}]_i$ dynamics. Based on this conceptual knowledge, calcium imaging as the most popular method for $[Ca^{2+}]_i$ dynamics is developed rapidly, which involves two parallel processes: the development and the continuous improvement of calcium

sensors, and the development and the implementation of the appropriate instrumentation. The detailed development history of calcium imaging has been well described in many review articles ***(C Grienberger et al. 2012 Neuron, RA de Melo Reis et al. 2020 Front Neurosci)***.

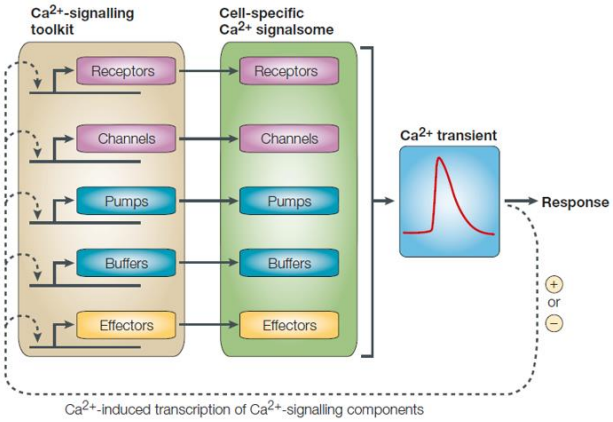

Fig. 4 Components underling versatile spatio-temporal [Ca^{2+}]$_i$ dynamics [Image from the paper: ***(MJ Berridge et al. 2003 Nat Rev Mol Cell Biol)]***

2 On Off and Tuning Mechanisms

It is widely accepted that calcium signals or [Ca^{2+}]$_i$ dynamics generated within cells involve generally three components: "on" components which contribute to the rise of calcium concentration in the cytoplasm, "off" components which are responsible to decrease and restore the evoked high calcium concentration to range of resting state, and the "tuning" components which affect the amplitude, frequency and kinetics of calcium signals ***(MJ Berridge et al. 2003 Nat Rev Mol Cell Biol)***.

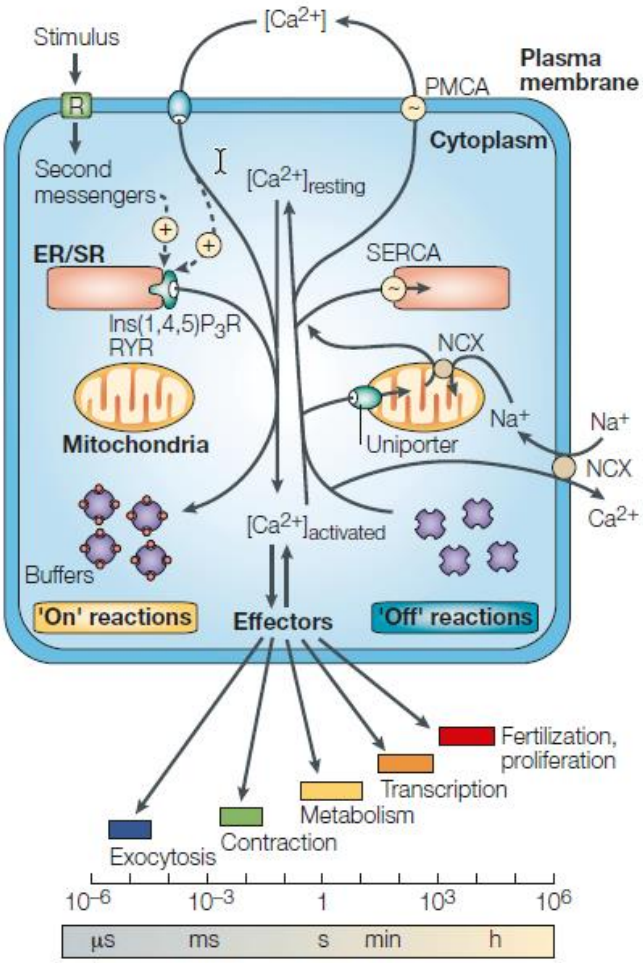

*Fig. 5 Overview of components for Ca^{2+} signals and dynamics [Image from:**(MJ Berridge et al. 2003 Nat Rev Mol Cell Biol)**]*

2.1 On components

Briefly, the calcium enters the cytoplasm through two calcium sources, extracellular source and internal stores. The latter includes many kinds of subcellular components, such as organelles like endoplasmic reticulum (ER), mitochondria, Golgi apparatus, endosomes and lysosome. Theoretically, at those separate domains with higher concentration of calcium than resting cytosolic calcium concentration could exist the "on" component. Therefore, depending on the different source of calcium, the "on" components can be variable.

2.1.1 Ca^{2+} entry from extracellular space

For the extracellular calcium, the "on" components are located on the plasma

membrane, which comprise mainly different families of channels. These families of channels can be divided into the following groups:

1. **Voltage operated calcium channels (VOCs)** which are ion channels mediating the influx of extracellular Ca^{2+} once activated by the membrane voltage or electrical potential across the membrane domains. VOCs can be divided into different types such as L type, P/Q type, N type, R type and T type, which can be further classified into subgroups based on their activation threshold: high voltage activated, intermediate voltage activated (N type and R type) and low voltage activated (T type), respectively.

The L-type calcium channel is activated by a strong depolarization voltage and inactivated with a slow time course and is expressed in neurons, endocrine, cardiac, and smooth muscle *(Tianhua Feng et al. 2018 Ion Channels in Health and Sickness)*. The N-, P−/Q-, and R-type calcium channels also require strong depolarization for activation and are expressed mainly in neurons *(TR Neelands et al. 2000 J Neurophysiol)*. The T-type calcium channel is opened with weak depolarization voltages and remains active for a short time and is widely expressed in various cell types *(L Xiao et al. 2020 Hum Cell)*.

2. **Receptor operated channels (ROCs)** which are activated by their receptors binding. Mainly, there are four types of ROCs with calcium permeability, namely, NMDA (NR1, NR2A, NR2B, NR2C, NR2D), P2X and nACh receptors, receptor of which are glutamate, ATP and acetylcholine, respectively. Ca^{2+} permeabilities of these receptors are within similar range. Of note, these receptors are abundantly expressed in the central nervous system such as glial cells and synapse domains of neurons *(Y Pankratov et al. 2014 Eur J Pharmacol)*.

3. **Second-messenger-operated channels (SMOCs)** which differs from receptor operated calcium channels regarding their activation pathway, which is controlled by other cytosolic second messengers such as cAMP or cGMP, and arachidonic acid. The corresponding SMOCs are named cyclic nucleotide gated channels (CNG) and Arachidonate-regulated Ca^{2+}-selective channel (ARC) *(RW Tsien et al. 1990 Annu Rev Cell Biol)*. CNG was firstly identified in photoreceptors and olfactory sensory neurons and later was found also to be expressed in other neurons and non-neuronal cells. CNG are encoded by six different genes, forming heterotetrameric complex consisting of two or three different types of subunits namely CNGA 1–4, CNGB 1, CNGB 3. It has been demonstrated the CNG heterotetrameric complex has special functional characteristics compared to the homotetrameric channels, hence likely generating stimulus specific Ca^{2+} signatures *(UB Kaupp et al. 2002 Physiol Rev, E Jarratt-Barnham et al. 2021 Int J Mol Sci)*. Arachidonate-regulated Ca^{2+}-selective channel

was found firstly present on the membrane of non-excitable cells, which independent of store depletion. Increasing evidences showed the role of ARC is similar to store-operated Ca^{2+} entry (SOCE). The difference between ARC and SOCE lies in that ARC channels are regulated by plasma membrane STIM1 while SOCE by means of endoplasmic reticulum STIM1. In addition, ARC channel pore is thought to be an assembly of three plasma membrane proteins, Orai1 and two Orai3 subunits *(JL Thompson et al. 2013 J Physiol)*.

4. **Transient receptor potential (TRP)** ion-channel family which mediate the transmembrane flux of cations down their electrochemical gradient, hence resulting in the rise of intracellular Ca^{2+}. TRP channels can be activated by a variety of gating mechanisms involving multiple stimuli ranging from ligand binding, voltage and temperature changes modified conformation of the channel *(IS Ramsey et al. 2006 Annu Rev Physiol, B Nilius et al. 2011 J Physiol)*. The TRP family can be subdivided into seven subfamilies: TRPC (canonial), TRPV (vanilloid), TRPM (melastatin), TRPP (polycystin), TRPML (mucolipin), TRPA (ankyrin) and TRPN (NOMPC-like), among which TRPC1–7, TRPV1–6, TRPM1–8, TRPML (mucolipidin 1,2), TRPNI (ANKTM1) are highly Ca^{2+} selective.

TRPs are expressed in almost every cell type in both excitable and non-excitable tissues. TRP channels are present in all cellular membranes, with the exception of the nuclear envelope and mitochondria. Most TRP channels are localized in the plasma membrane, where they have an essential role in the influx and/or transcellular machinery that transports Ca^{2+}, Mg^{2+} and trace metal ions, and they modulate the driving force for ion entry *(B Nilius et al. 2011 J Physiol)*.

5. **Mechanically activated ion channels** which sense and convert the physical forces into intracellular electrical or chemical signals. Such kind of channels include Piezo (Piezo1 and Piezo2), OSCA/TMEM63 channels, and membranes of TRP channels family like TRPV4, which, once activated, are able to mediate the influx of extracellular calcium *(JM Kefauver et al. 2020 Nature)*.

6. **Store operated channels (SOCs)** which are responsible for the well-known store operated calcium entry (SOCE), a process of calcium influx across the plasma membrane when ER calcium stores is emptying. Two families of channels are related to the SOCE: Orai and TRPC. In vertebrates, Orai comprises three members of the family, Orai 1-3, which share many similarities in structure and function and are all activated by calcium store emptying. Orai is gated directly by STIM1-SOAR domain binding the C-terminal and N-terminal of the channel *(C Moreno et al. 2011 IUBMB Life)*.

Some members of TRPC families are the other SOCs, among which TRPC1 was the first member proposed as SOC channel in Chinses hamster ovary cells and monkey COS cells. Afterwards, its role as the SOC channel was identified in many other human cells, such as submandibular gland cells, endothelial cells, platelets and so on. In addition to TRPC1, TRPC4, TRPC5 and TRPC6 are all recognized to be candidates as SOCs ***(JJ Lopez et al. 2020 Cells)***.

2.1.2 Ca^{2+} release from internal stores

For the internal store of calcium, the "on" components are located on the membranes of different subcellular organelles. These families of channels can be divided into the following groups depending on the organelles or subcellular domains:

1. Endoplasmic Reticulum

The endoplasmic reticulum (termed sarcoplasmic reticulum, SR, in muscle cells) is the largest intracellular Ca^{2+} store, where concentration of calcium can reach 1mM depending on the cell type. Rapid release of calcium from ER lead to significant and sustained rises of cytosolic calcium concentration, required for specific cell functions. The rapid release of ER calcium is mainly mediated through the mechanism called calcium induced calcium release (CICR), which can be briefly subdivided into two groups depending type of channels: ryanodine receptor (RyRs) mediated ca^{2+} release and inositol 1,4,5-trisphosphate (IP3) receptors (IP3Rs) mediated Ca^{2+} release. An important difference between these two types of CICR is that RyR can be gated to cause calcium release with Ca^{2+} alone, while IP3R instead causes Ca^{2+} release only in the presence of IP3, in addition to proper concentration ca^{2+}. The latter is also termed IP3 induced calcium release (IICR) ***(A Verkhratsky et al. 1996 Cell Calcium)***.

Ryanodine receptors (RyRs) are large calcium release channels, predominantly expressed in excitable cells. There are three isoforms of RyRs in mammals, RyR1-3. Of note, RyR1 are mainly expressed in skeletal muscle cells and also exist in the CNS; RyR2 are predominantly present in cardiac muscle cells, while RyR3 are expressed more ubiquitously ***(R Ma et al. 2020 Nat Chem Biol)***.

Inositol 1,4,5-trisphosphate (InsP3 or IP3) receptors are a family of ligand-gated Calcium release channels expressed predominantly in the ER from all cell types. The gating of IP3Rs is not only by IP3 but also by some other ligands, in particular cytoplasmic Ca^{2+}. The IP3Rs also comprise three isoforms: IP3R1-3, which have

similar structures but different physiological characters *(JK Foskett et al. 2007 Physiol Rev)*. Their patterns of tissue distribution are also different: IP3R1 is predominantly expressed in the central neural nervous system while IP3R2 and IP3R3 are present in a rather ubiquitous tissue expression pattern. More, the ratio between the three subtypes of IP3R expressed is specific to each cell type *(A Bartok et al. 2019 Nat Commun)*.

In addition to the channels mentioned above, polycystin-1 (PC1) and polycystin-2 (PC2) could behaves as calcium channel. In particular, PC2 is predominantly located in ER and Mutations to PC2, as well as PC1 can cause decrease in Ca^{2+} release from ER in autosomal dominant polycystic kidney disease (ADPSD). Of note, PC2 can also functionally interacts with IP3R, exerting prolonging effect to InsP3-induced Ca^{2+} transients while ER localized PC1 decreases the InsP3-induced Ca^{2+} response when binding the IP3R, suggesting a competitive relation between PC1 and PC2 for binding the InsP3R. The gating mechanism of PC is currently unclear *(FO Lemos et al. 2018 Cell Calcium)*.

2. Mitochondria

Till now, two distinct mechanisms mediate Ca^{2+} outward transport, that is, calcium efflux from mitochondria into cytosol: the Na^+-dependent ($Na^+/Li^+/Ca^{2+}$ exchanger, NCLX) which is benzodiazepines and CGP-37157-sensitive, and the Na^+-independent (H^+–Ca^{2+} exchanger) Ca^{2+} efflux which is ruthenium red-insensitive *(A Takeuchi et al. 2015 J Physiol Sci)*.

NCLX, different from its plasma counterparts NCX and NCKX, mainly mediates the Ca^{2+} extrusion in excitable cells such as pancreatic beta-cells, astrocytes, B lymphocytes and cardiomyocytes *(A Takeuchi et al. 2015 J Physiol Sci)*. This Ca^{2+} extrusion from the mitochondria is drived by the electrochemical gradient ($\Delta\Psi m$) due to Na^+ entry into the mitochondrial matrix from the cytosol. Therefore, factors contribute to mitochondrial Ca^{2+} extrusion by NCLX include the both concentrations of cytosolic Na^+ and matrix Na^+, $\Delta\Psi m$ and also the stoichiometry of NCLX *(L Boyman et al. 2013 J Mol Cell Cardiol)*. Three mammalian genes have been isolated so far, encoding for different sarcolemmal NCLX isoforms: NCLX1–3, sharing similar properties such as ionic affinities and pharmacological characteristics *(UC Hoppe 2010 FEBS Lett)*. As for the stoichiometry of the Na^+/Ca^{2+} exchange, there are controversial conclusions with two different exchange ratios: 2:1 and 3:1, which suggest electroneutral and electrogenic properties of NCLX, respectively *(L Boyman et al. 2013 J Mol Cell Cardiol)*.

In non-excitable cells like liver and kidney cells, mitochondrial Ca^{2+} efflux is mainly mediated by the H^+/Ca^{2+} exchanger (CHE). Ca^{2+} is extruded against the slight

electrochemical gradient of the inner mitochondrial membrane, with supposed exchange ratio of 2:1 (electroneutral). Of note, it seems there exist additional transport route with much stronger electrochemical gradient against which Ca^{2+} is extruded, which should be energy dependent ***(UC Hoppe 2010 FEBS Lett)***.

Till now, LETM1 is putatively thought as the gene encoding the CHE, which is still currently under debate due to its similar role related to K^+/H^+ exchanger (KHE) ***(GK Natarajan et al. 2021 Front Physiol)***.

3. Golgi apparatus (GA)

It has been clear during past decade that GA actually functions as an important internal store for calcium like ER, which involves the shaping of the calcium signals. There are some channels which are responsible for the efflux of calcium from GA. These channels include IP3Rs and RyRs, which like in ER mediate the CICR in GA. However, it appeared the kinetics of Ca^{2+} release from the GA differs from those of the ER in some way: Ca^{2+} release from the GA terminated sooner than that from the ER ***(P Pizzo et al. 2011 Cell Calcium)***.

4. Endolysosomes

Lysosomes and endosomes (endolysosomes) are small Ca^{2+} stores but importantly cooperate with other calcium storage like ER to amplify Ca^{2+} release through CICR, to influence localized Ca^{2+} signals ***(A Galione 2015 Cell Calcium)***. Of note the endolysosome is comprised of early endosomes (EEs), recycling endosomes (REs), late endosomes (LEs), and lysosomes (LYs).

The release of endolysosomal Ca^{2+} is mainly through the TRPML channel family (especially TRPM1), which includes TRPML1, TRPML2, and TRPML3 ***(X Cheng et al. 2010 FEBS Lett)***. All the TRPML channels can be activated by phosphatidylinositol 3,5-bisphosphate (PI(3,5)P2) – a phosphoinositide enriched in endolysosomes. Interestingly, TRPML1 and Drosophila TRPMLs are inhibited by phosphatidylinositol 4, 5-bisphosphate (PI(4,5)P2), the latter are PIP2 species in plasma membrane, supporting the notion that TRPMLs mainly function in endolysosomes. However, the gating mechanisms of TRPMLs under physiological conditions remain unknown, though TRPMLs pore properties have been well investigated ***(X Cheng et al. 2010 FEBS Lett, K Venkatachalam et al. 2015 Cell Calcium)***.

TRPML1 is predominantly localized on the late endosomes and the lysosomes while TRPML2 and TRPML3 are present primarily on the recycling endosomes and the early endosomes, respectively. TRPML1 is expressed ubiquitously in all tissues,

while TRPML2 and TRPML3 expressed in specific organs like thymus, spleen*(X Cheng et al. 2010 FEBS Lett, Wu Y et al. 2021 Cancers)*.

Two-pore channels (TPCs) widely expressed in endolysosomes are other channels mediating the release of calcium from endolysosomes into cytosol. TPCs can be activated by NAADP, PI(3,5)P2 and voltage. TPCs have three isoforms: TPC1-3, TPC1 and TPC3 are expressed mainly in endosomal compartments while TPC2 is localized predominantly on the lysosomal membranes *(A Raffaello et al. 2016 Trends Biochem Sci, Wu Y et al. 2021 Cancers)*.

P2X4 which belongs to ionotropic P2X-family ATP receptors can also lead to the efflux of calcium from endolysosomes. P2X4 can be gated by intraluminal ATP meanwhile P2X4 activity is inhibited by acidic luminal pH *(Wu Y et al. 2021 Cancers)*.

In addition to the channels mentioned above, several other Ca^{2+} channels have been reported to be expressed in the lysosome which could mediate Ca^{2+} release, including transient receptor potential ankyrin 1 (TRPA1), transient receptor potential melastatin 2 (TRPM2), and P/Q-type voltage gated Ca^{2+} channels *(Wu Y et al. 2021 Cancers)*.

2.2 Off components

The Ca^{2+} influx into the cytosol triggered by the on components needs to be counteracted by the efflux of Ca^{2+} mediated by the off components, so that the resting level of cytosolic Ca^{2+} can be maintain below ~200 nM. Usually the components are comprised of various pumps and exchangers, which have different forms or special counterparts depending on the locations where they are functioning, that is, plasma membrane and internal stores like different organelles.

2.2.1 Ca^{2+} extrusion across plasma membrane

1. The plasma-membrane Ca^{2+} pumps

The plasma membrane calcium ATPase (PMCA) contributes mainly to the efflux of calcium, answering the rapid rise of the cytosolic Ca^{2+} thus playing a housekeeping role in maintaining cytosolic Ca^{2+}. The pump operates with high Ca^{2+} affinity but low transport capacity, with a stoichiometry of 1:1 Ca^{2+}/ATP. PMCA pumps at resting state have low affinity with a Kd of 10-20 μM, thus are not sensitive to sub μM cytoplasmic Ca^{2+} concentrations, but PMCA pumps modulated

by factors such as calmodulin and acidic phospholipids, have a high affinity (the value of Kd: about 200 nM), nonetheless *(M Brini et al. 2011 Cold Spring Harb Perspect Biol)*. PMCAs are a four-gene (ATP2B 1-4) products, including four isoforms: PMCA1-4. Further diversity is generated by alternative splicing of transcripts at three sites (A, B and C). PMCA isoforms and variants are expressed in a tissue- and cell-specific manner. PMCA1 and PMCA4 are expressed ubiquitously while PMCA2 and PMCA3 are abundant in excitable tissues or in cells with strong calcium activities *(EF Talarico, Jr. et al. 2007 Exp Eye Res)*.

2. The Na^+-Ca^{2+} exchangers (NCXs)

NCX is a membrane spanning electrogenic antiporter, present in most cell types. NCXs perform Ca^{2+} extrusion along the electrochemical gradient of Na^+: three Na^+ ions enter the cell at cost of one Ca^{2+} ion extruded against its gradient. Of note, the exchanger can also work in reverse mode, depending on the electrochemical gradients of the substrate ions. In contrast to PMCA, NCX has a low–Ca^{2+}-affinity but a high-capacity, working effectively under large concentrations of Ca^{2+}, extruding large amounts of Ca^{2+} in a short time *(M Brini et al. 2011 Cold Spring Harb Perspect Biol)*.

In mammalian, NCXs have threes isoforms: NCX 1-3, which are encoded by three separate genes. NCX1 is mainly expressed in heart, kidney and brain, NCX2 is predominantly expressed in brain and NCX3 is present mostly in excitable tissues such as brain and skeletal muscle *(LYM Michel et al. 2014 J Biol Chem)*.

2.2.2 Ca^{2+} uptake by intracellular stores

1. Endoplasmic reticulum/ sarcoplasmic reticulum

Excessive cytosolic Ca^{2+} can be uptaken by endoplasmic reticulum/sarcoplasmic reticulum through the sarco/endoplasmic reticulum Ca2+-ATPase (SERCA), which is transmembrane ion transporter belonging to the PII-type ATPase family common with the plasma membrane Ca2+-ATPases (PMCA). SERCA re-sequesters cytoplasmic Ca^{2+} to the sarco/endoplasmic reticulum store, thereby terminating Ca^{2+}-induced signaling.

Mammalian cells express three isoforms of the pump: SERCA 1-3, encoded by three genes, ATP2A 1-3 accordingly. Among them, only SERCA3 is ubiquitously expressed while SERCA1 and SERCA2 are expressed specifically in limited types of cells, such as skeletal muscle (exclusively for SERCA1), cardiac muscle, brain, and

other tissues. Meanwhile, the total number of subtypes can reach to 10 through post-translational splice variants. All SERCA isoforms possess different affinities to calcium and specific kinetic characters, which is combined with tissue- or cell-specific expression, imparting unique properties of calcium homeostasis to certain cells *(T Boczek et al. 2021 Int J Mol Sci)*. Additionally, SERCA activity can be modulated by transmembrane proteins like phospholamban and sarcolipin *(A Raffaello et al. 2016 Trends Biochem Sci)*.

2. Mitochondria

Mitochondrial Ca^{2+} uptake from cytosol is mediated by a complex of macromolecular structure called mitochondrial calcium uniporter (MCU) complex, the composition of which may vary depending on the cell type and different epigenetic control mechanisms. The MCU complex is comprised of Ca^{2+}-selective channel (MCU) and its regulatory factors including the MCU-dominant negative beta subunit (MCUb), essential MCU regulator (EMRE), MCU regulator 1 (MCUR1) and mitochondrial calcium uptake (MICU) 1-3. Mitochondrial Ca^{2+} uptake by MCU requires a respiratory chain - generated proton gradient across the inner mitochondrial membrane (IMM), which produces mitochondrial membrane potential ($\Delta\Psi m$), which contributes to the entry of $Ca2^{+}$ across MCU *(D De Stefani et al. 2016 Annu Rev Biochem, C Cui et al. 2019 Br J Pharmacol)*.

Of note, the MCU has poor affinity to Ca^{2+} (Kd: around 10–50 μM), suggesting that under resting conditions, mitochondria may not uptake any Ca^{2+}. However, high Ca^{2+} microdomains like the ER/SR and mitochondria interface allow MCU operate effectively in local calcium signaling *(M Patron et al. 2013 J Biol Chem, J Mishra et al. 2017 Handb Exp Pharmacol, C Cui et al. 2019 Br J Pharmacol)*.

3. Golgi apparatus

Two types of Ca^{2+} -ATPase localize on the GA membrane, one is SERCA common with those present in the SR/ER membrane, and the other is secretory pathway Ca^{2+}-ATPase (SPCA), which mainly expressed on the membrane of secretory organelles like secretory vesicles. For SERCA, among the isoforms of the Ca^{2+} ATPase, SERCA2b is the principal isoform in this organelle. SPCAs have structural and mechanistic properties of SERCA except for strong preference of SPCAs also for Mn^{2+} ions. In human, there exist two SPCA isoforms: SPCA1 and SPCA2 which are encoded by ATP2C1 and ATPC2, respectively. SPCA has a high affinity to Ca^{2+}, for instance, the overall affinity to calcium of human SPCA1 is around 10 nM, more than one order lower than that of SERCA *(LH Li et al. 2013 Neurosignals)*.

The two isoforms have different expression patterns depending on the types of the tissues and cells. SPCA1 is expressed ubiquitously on the GA membranes playing a housekeeping role, with predominant expressions in epidermal keratinocytes and brain while the expression of SPAC2 is mainly in respiratory, gastrointestinal, genitourinary systems, salivary and mammary glands *(T Boczek et al. 2021 Int J Mol Sci)*.

4. Endolysosome

The identity of the pumps or exchanger mediating lysosomal Ca^{2+} uptake is still unclear. Ca^{2+}/H^{+} exchanger (CAX) was putatively recognized as the exchanger mediating the lysosomal Ca^{2+} uptake by using the proton gradient across the membrane since the first lysosomal CAX in nonplacental mammals was described by Melchionda et al. in 2016 *(E Lloyd-Evans 2016 J Cell Biol)*. Nonetheless, CAX has not been found in placental mammals so far. Additionally, Ca^{2+} pumps were putatively located on several types of acidic Ca^{2+} store while underlying molecular mechanism remains unresolved *(J Yang et al. 2019 Protein Cell)*.

2.3 Tuning components

Most of intracellular calcium element exists in bound forms by binding many kinds of intracellular proteins, which are termed as calcium binding proteins. Calcium binding proteins including calcium buffers and calcium sensors, the main difference of which lies in that calcium buffers assumingly are thought to not produce specific cellular effects but only bind and sequester the cytosolic calcium including those from extracellular space and internal stores while calcium sensors when binding the calcium can change their conformations, which permit them to interact with specific targets thus leading to changes of cellular functions.

The existence of large amount of calcium binding proteins, especially calcium buffers definitely can affect the calcium signals evoked by various kinds of stimuluses or specific cellular processes. Actually, they affect both the temporal and spatial aspects of these transient increases in Ca^{2+} *(B Schwaller 2010 Cold Spring Harb Perspect Biol)*. For example, buffering action will reduce the amplitude of a change in intracellular Ca^{2+} and prolong the decay *(SM McMahon et al. 2018 Trends Neurosci)*. Compared with calcium buffers, Ca^{2+} sensors, more likely, act as modulators of long-lived or secondary intracellular Ca^{2+} signals through calcium mobilizing mechanisms *(MJ Berridge et al. 2000 Nat Rev Mol Cell Biol)*. In other words, calcium binding proteins exert tuning effect to shape specific evoked calcium signals, which result in activations

of specific calcium signaling pathways, which has been described well by Guido C. Faas et al in paper published in 2012 ***(GC Faas et al. 2012 Biochim Biophys Acta)***. The well-studied calcium buffers include calbindin D-28, calretinin and parvalbumin. And common calcium sensors contain: calmodulin, troponin C, synaptotagmin, S100A1–12, S100B, S100C, S100P, annexin I–X, neuronal Ca2+ sensor family (NCS-1), visinin-like proteins (VILIP-1,VILIP-2,VILIP-3), hippocalcin, recoverin, K_v-channel-interacting proteins (KchIP1–3), guanylate-cyclase-activating proteins (GCAP1–3)***(MJ Berridge et al. 2003 Nat Rev Mol Cell Biol)***. The tuning effects of calcium binding proteins comes from the factors as discussed below.

The primary character for calcium buffers is the concentrations of calcium buffers which are variable depending on the types of cells. The overall strength of intracellular Ca^{2+} buffering can be characterized by the Ca^{2+}-binding ratio (kS) defined as the ratio of buffer-bound Ca^{2+} to free Ca^{2+}. The concept of the Ca^{2+}-binding ratio of endogenous buffers has proven to be useful, which now serves as a measure to compare the Ca^{2+}-buffering capacity of different cell types ***(B Schwaller 2010 Cold Spring Harb Perspect Biol, I Delvendahl et al. 2015 Proc Natl Acad Sci U S A)***. In other aspect, for a specific calcium binding protein, the buffering capacity can be characterized by calcium-binding stoichiometry for calcium-binding proteins. For example, parvalbumin containing three, and both calbindin and calretinin, consisting of six EF-hand domains, binding three, four, and five Ca^{2+} ions, respectively ***(R Fairless et al. 2019 Int J Mol Sci)***.

Calcium-binding affinities is another important parameter for a calcium buffering protein. In eukaryotic cells, affinities of hundreds of calcium binding proteins vary over a 10^6-fold range (nM to mM). For intracellular Ca^{2+}-binding proteins, such as calmodulin (CaM) or parvalbumin, the Ca^{2+}-binding affinities fall within submicromolar range, which corresponds to the resting cytosolic Ca^{2+} concentrations at ~100 nM ***(Y Zhou et al. 2013 Metallomics)***. In general, calcium binding proteins contain two well-defined Ca^{2+}-binding motifs: the EF hand and C2 domains. Taking the EF-hand motif for example, EF-hand domains are the most common Ca^{2+}-binding motifs found in proteins. Generally, affinity values of EF-hand domains for Ca^{2+} vary from micromolar to millimolar, reflecting the diversity of functions carried out by these proteins in the range of Ca^{2+} concentrations ***(M Mazumder et al. 2014 PLoS One, R Bagur et al. 2017 Mol Cell)***.

Calcium-binding kinetics of calcium binding proteins also strongly affect the spatiotemporal aspects of Ca^{2+} signals, which operate with different on-rates for calcium binding (K_{on}). The on-rates for Ca^{2+} binding vary by more than two orders of magnitude. CB-D9k and troponin C, have fast Kon rates>10^8 M^{-1} s^{-1} while on-

rates for parvalbumin can be as slow as $3* 10^{6}$ $M^{-1}s^{-1}$ under physiological conditions with Mg^{2+}. Of note, the kinetics of calcium binding proteins can be complexed by the fact that a given protein may have sites with different affinities and kinetics ***(B Schwaller 2010 Cold Spring Harb Perspect Biol)***.

The last consideration for charactering calcium binding proteins is the mobility. Mobile buffers affect the time course and spatial range of calcium signals ***(A Hernandez-Cruz et al. 1990 Science)***. The properties and functional role of mobile calcium binding proteins have been well reviewed ***(KG Baimbridge et al. 1992 Trends Neurosci, B Schwaller 2010 Cold Spring Harb Perspect Biol)***. In other hand, immobile calcium buffers also play their unique role in shaping the spatial domain of intracellular free calcium. Immobile buffers alone greatly slow the spatial spread of calcium but prolong the temporal duration of the signal instead. Mobile buffers, together with immobile buffers increase the complexity of the spatiotemporal signaling signatures, especially in the neuron, based on the relative affinities, kinetics, concentrations of the different buffers, and other factors ***(EA Matthews et al. 2015 Front Cell Neurosci)***.

It is worthy of note, in addition to calcium binding proteins, which stand for the molecular tuning component, Subcellular organelles when uptaking the cytosolic Ca^{2+} can buffer the evoked calcium transients both locally and globally, thus can be recognized as the tuning components.

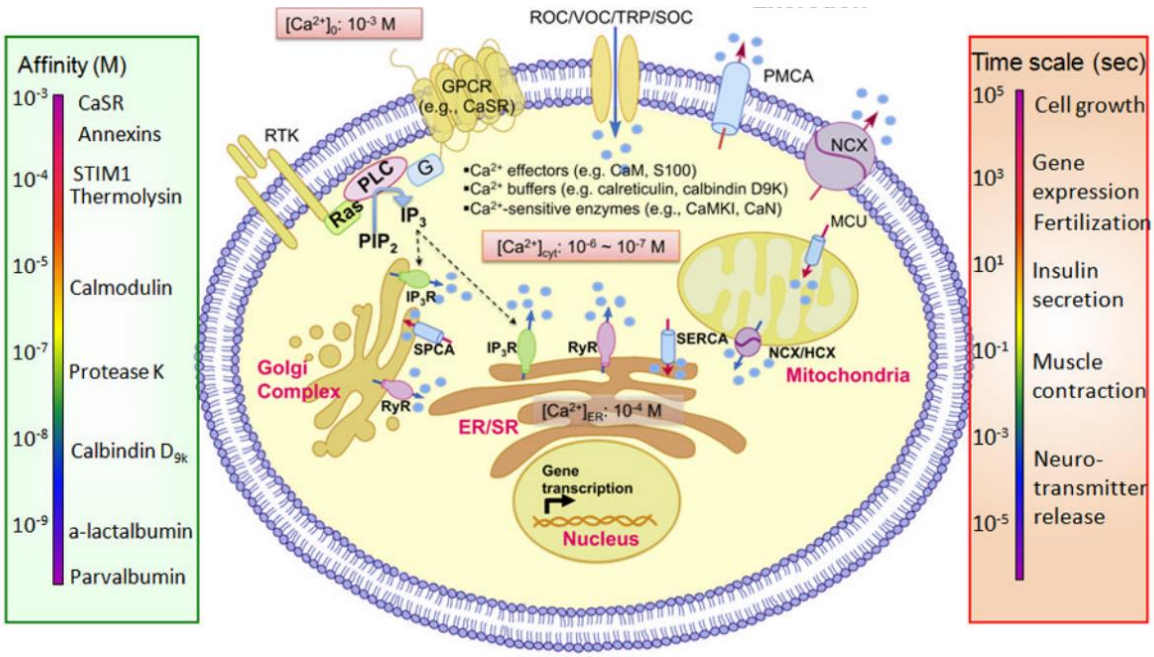

Fig. 6. Schematics of the Ca2+ signaling machinery, the range of Ca2+-binding affinities and the timescale of Ca2+ modulated activities [Image from the paper: ***(Y Zhou et al. 2013 Metallomics)****]*

3 Local and Global Ca^{2+} Signals and Dynamics

3.1 Ubiquitous mechanism of PLC-IP3 pathways

The generating of local and global signals can be well explained by a ubiquitous mechanism of PLC (phospholipase C)-IP3 pathway, which involves the activations PLC-beta and PLC-gamma by various stimuli. Taking the typical GPCR-PLC pathway for example, G-protein-coupled receptors (GPCRs), which are proteins sharing a seven alpha-helical transmembrane structure, the main function of which is transduction of extracellular stimuli through coupling to heterotrimeric G-proteins including three subfamilies(G-alpha, G-beta, and G-gamma), and the corresponding effectors. Upon being activated by the GPCR, PLC-beta stimulates the hydrolysis the membrane lipid phosphatidylinositol 4,5-bisphosphate, producing generating inositol 1,4,5-trisphosphateb (IP3). The latter then diffuse in the cytoplasm and binds to its receptors (IP3R) on the ER membrane. Binding of IP3 leads to the gating of IP3R, which induces Ca^{2+} release from the ER lumen to cytoplasm. The released Ca^{2+} in the cytoplasm moves by passive diffusion which meanwhile is limited by mobile and immobile Ca^{2+} binding proteins acting as buffers. Consequentially, a slight local calcium transient called “blip” is shaped within microdomains near the mouth of an IP3R Ca^{2+} channel, where the concentration of the Ca^{2+} is believed to be very high so that the IP3Rs nearby get ready being gated, gating open of which depends on the amount of available IP3. When IP3 is in intermediate concentration, there will be more or clustered IP3Rs around blip being gated open, which generates a bigger calcium transient termed “puff”. If high concentration of IP3 is present around the blip or puff, global calcium waves will be initiated and spread across the whole cell, even adjacent cells ***(JK Foskett et al. 2007 Physiol Rev)***.

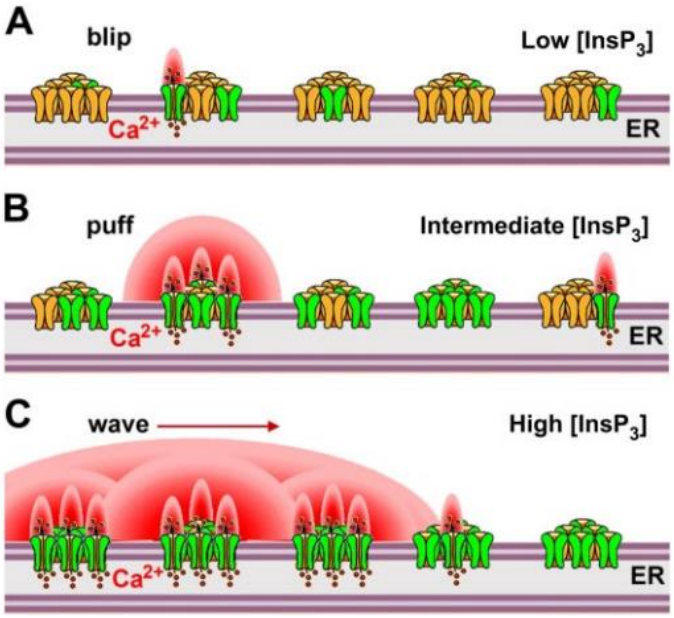

Fig. 7 Outline of local and global calcium dynamics through ubiquitous mechanism of PLC-IP3 pathways [Image from the paper: ***(JK Foskett et al. 2007 Physiol Rev)****]*

3.2 Organization of local Ca^{2+} signals

Despite typical GPCR-PLC pathway mentioned above, the local calcium signals, as the triggers and building blocks for larger global calcium spreading across the cells, usually are generated directly by the Ca^{2+}, influx especially from the on components, which are shaped, to a great extent by tuning component mentioned above. Combinations between specific tuning components and the local calcium signals by different channels define the specificity of the calcium signals, thus regulating different cellular processes. The followings are the demonstrations of the local signals induced by different types of channels, which lead to specific cellular activities.

1. Local Ca^{2+} signaling in neurons

In neurons, calcium signals in synapses represent important local calcium signals for normal neuronal functions. In presynaptic terminals, it is clear that voltage-gated Ca^{2+} channels serve as the main sources for Ca^{2+}. The channels are spatially close to vesicular protein synaptotagmin as the tuning component. Combination between these two components leads to local calcium signals which is important for neurotransmitter release. On the other hand, local postsynaptic Ca^{2+} signals are mediated by NMDA receptors and a senor complex involving PSD-95, GKAP,

Shank, and Homer. The resultant calcium sparks then induce Ca^{2+} release from IP3 receptors or RyRs, repetitive activation of which leads to generation of Ca^{2+} waves with a propagation rate of wave of approximately 70um/s ***(GJ Augustine et al. 2003 Neuron)***.

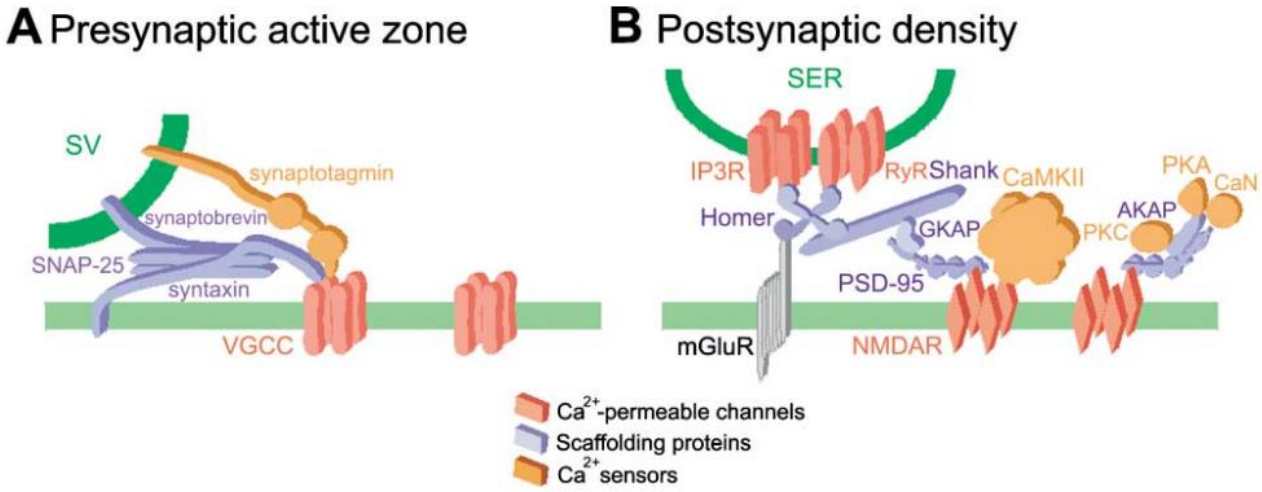

*Fig. 8 Local Ca2+ signaling in presynaptic and postsynaptic compartments [Image from the paper:**(GJ Augustine et al. 2003 Neuron)**]*

2. Local Ca^{2+} signals: STIM and ORAI proteins

It is believed that ORAI1 STIM1 coupling mediated Ca^{2+} entry mediates the formation of spontaneous Ca^{2+} microdomains observed in T cells. The local Ca^{2+} signals take place at the initial activation of the T cell receptor (TCR)/CD3 complex and CD28, leading to formation of NAADP. The latter then induce Ca^{2+} release via RyR1, the majority of which is localized in ER–PM junctions where local calcium signals are formed by very close cooperation between RYR1 mediated Ca^{2+} release, local decrease of the luminal [Ca^{2+}], STIM1/2 activation and ORAI1-evoked Ca^{2+} entry. Eventually the emerging Ca^{2+} microdomains convert into global Ca^{2+} signaling ***(B-P Diercks et al. 2020 Current Opinion in Physiology)***.

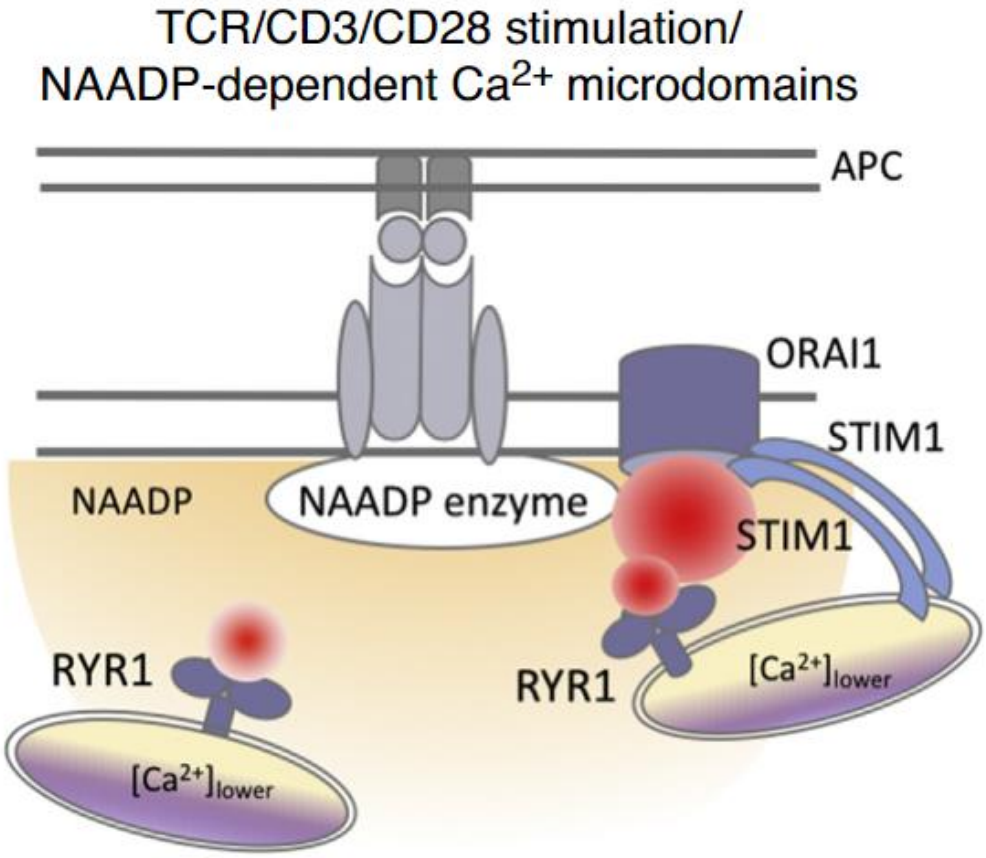

Fig. 9 Local calcium signals during activation of the T cell receptors [Image from the paper : ***(B-P Diercks et al. 2020 Current Opinion in Physiology)****]*

3. Ca^{2+} sparks underlie global Ca^{2+} signals in cardiac myocytes

In heart and skeletal muscle, the evoked Ca^{2+} sparks triggered by the Ca^{2+} influx mediated by low-voltage-activated T-type Ca^{2+} channels, these sparks induce release of Ca^{2+} from the sarcoplasmic reticulum by RyRs progressive, leading to increase in cytoplasmic Ca^{2+}. Electrogenic forward mode Na^{+}/Ca^{2+} exchange is then promoted and the resultant inward current drives the cell towards the threshold for depolarization. Spatiotemporal recruitment of Ca^{2+} sparks underlies the global Ca^{2+} signals that subsequently activate myocyte contraction ***(MD Bootman et al. 2001 Semin Cell Dev Biol).***

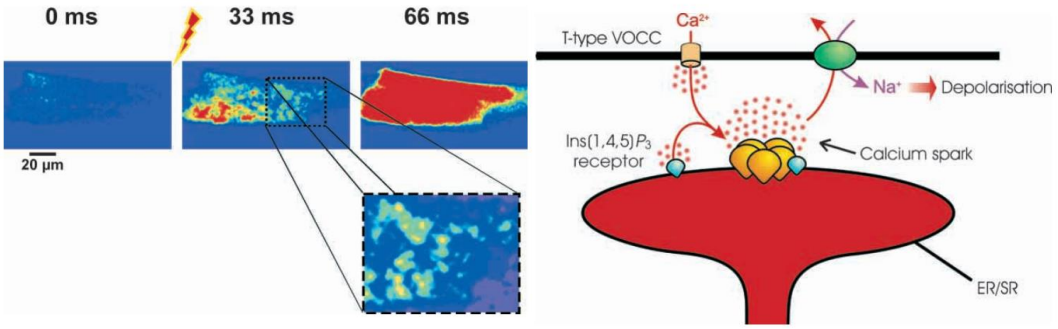

*Fig. 10 Ca^{2+} sparks underlie global Ca^{2+} signals in cardiac myocytes[Image from the paper:**(MD Bootman et al. 2001 Semin Cell Dev Biol)**]*

4 Ca^{2+} Dynamics and Cellular Processes

Changes in the intracellular concentration of Ca^{2+} control diverse cellular and physiological processes, including neurotransmitter release, hormone secretion, cell fate and gene expression. The spatiotemporal control of the intracellular Ca^{2+} concentrations through different combinations of on, off and tuning components is critical to result changes in intracellular calcium signaling required by different cellular processes. The followings are focused on review of the roles of calcium dynamics in mechanotransduction, phototransduction, and cancer progression like glioma malignancy.

4.1 Ca^{2+} dynamics and mechanotransduction

Cells perceive forces through a variety of molecular sensors, which convert mechanical cues into electrochemical signals, a process termed as mechanotransduction. The primary sensors that mediate mechanotransduction are ion channels, especially those named mechanosensitive channels, which usually play a role of on components, that is, converting the mechanical forces into cytosolic influx of Ca^{2+}. Combining with specific tuning component, different patterns of calcium signals will be generated, thus regulating specific processes of mechanotransduction.

4.1.1 The on components

1. MscL, MscS and MscS-like channels

This group of channels are mainly expressed in the prokaryotic cells, consisting of s mechanosensitive channel large conductance (MscL) and mechanosensitive channel small conductance (MscS), and their homologues in archaea and plants (MscS-like channels). Among them, mechanosensitive channel large conductance (MscL) is non-selective and opens its large pore like the iris of a camera in response to membrane tension; mechanosensitive channel small conductance (MscS) is structurally different from MscL, activated by lower threshold of pressure *(JM Kefauver et al. 2020 Nature)*.

2. Piezo 1 and Piezo 2

The Piezo family is a recently identified group of non-selective cationic mechanotransduction sensors shown to be physiologically relevant in mammals. Piezo channels can be activated by various kinds of mechanical stimuli, such as shear stress using a microfluidic chamber, stretching the membrane by applying positive or negative pressure through a patch-clamp recording electrode or by poking the membrane using a blunt glass pipette *(T Parpaite et al. 2017 Curr Biol)*.

3. OSCA/TMEM63 channels

OSCA/TMEM63 channels are inherently mechanosensitive channels conserved across plants and animals. OSCAs and their mechanosensitive animal homologues TMEM63A and TMEM63B are activated at a high threshold relative to PIEZO channels. Of note, TMEM63A is thought to be expressed in tissues that experience mechanical forces such as kidney and stomach, while TMEM63B is mainly present in the nervous system as well as in the heart, skeletal muscle, and stomach *(SE Murthy et al. 2018 Elife, JM Kefauver et al. 2020 Nature)*.

4. Transient receptor potential channels

Transient receptor potential (TRP) channels often exhibit polymodal gating by chemicals, signaling lipids and physical stimuli. Not all TRP channels directly sense mechanical cues. TRPA1 is known as mechanosensor in C. elegans *(KS Kindt et al. 2007 Nat Neurosci)*. C. elegans TRP-4 is also believed to be bona fide mechanosensitive channel, as proved by mutagenesis studies *(L Kang et al. 2010 Neuron)*. Additionally, Drosophila NOMPC or TRPN1 was recently proved to be a mechanotransduction channel subunit for gentle-touch sensation *(Z Yan et al. 2013 Nature)*.

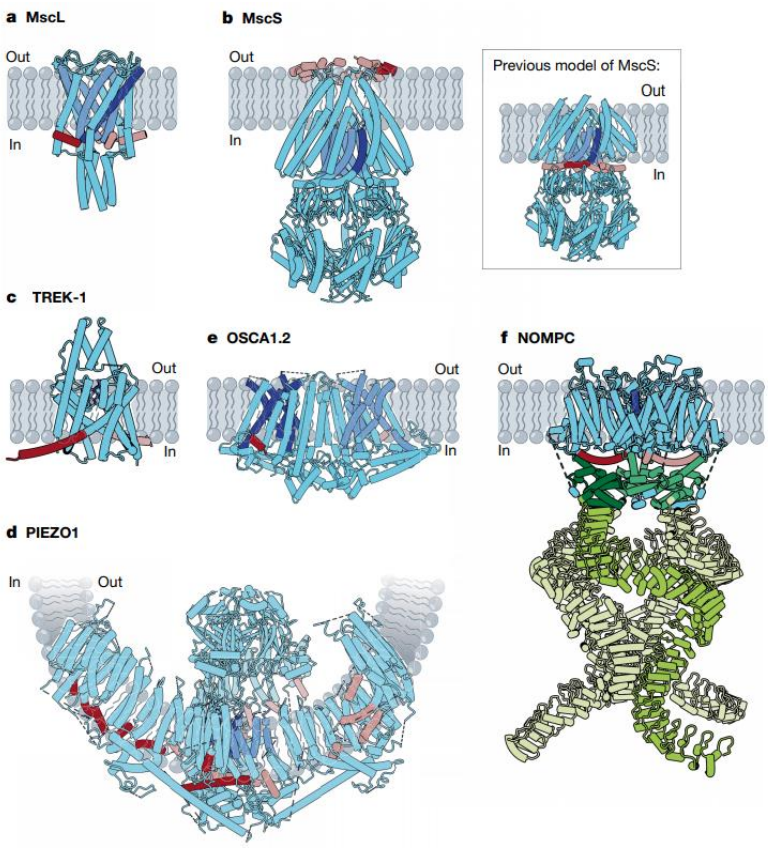

Fig. 11 Structures of mechanically activated ion channels [Image from the paper: ***(JM Kefauver et al. 2020 Nature)****]*

4.1.2 The tuning components

In addition to introduction of the on components above, which initialize the mechanosensitivity, it is important to discuss how the combinations between on components and tuning components realize the specific mechanotransduction process for certain biological function. The following is to show the examples in which tuning components together with on components regulate certain mechanotransduction process.

1. **Chondrocyte mechanotransduction pathways in posttraumatic osteoarthritis pathogenesis**

During Chondrocyte senses the extracellular mechanical forces, mechanosensitive ion channels including TRPV4 and Piezo family channels increase intracellular Ca^{2+} concentrations, which is buffered by mitochondria. Excessive intra-mitochondrial Ca^{2+} can lead to mitochondrial dysfunction, which promotes oxidative stress,

inflammatory signaling and cell apoptosis. Consequentially, mechanical inputs and inflammatory signaling produce more matrix-degrading enzymes, further deteriorating this situation, ultimately leading to chronic pathological outcomes that escalate joint dysfunction and pain in osteoarthritis ***(ML Delco et al. 2021 Nat Rev Rheumatol)***.

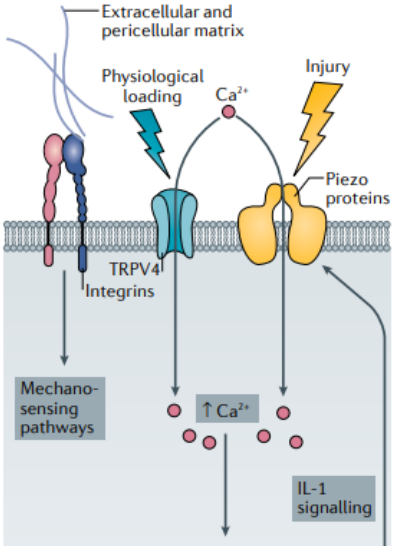

Fig. 12 chondrocyte mechanotransduction pathways in posttraumatic osteoarthritis pathogenesis [Image from the paper: ***(ML Delco et al. 2021 Nat Rev Rheumatol)****]*

2. Piezo1 coupling to calpain for integration of vascular architecture with physiological force

The physical forces regulate the structure and function of endothelial cells. During this process, Piezo1 channels function as sensors of frictional force (shear stress) , calcium influx due to Piezo1 activation is thought to bind to and activate calpain. The latter plays roles in focal adhesion turnover and endothelial cell alignment to shear stress organization via proteolytic cleavage of actin cytoskeletal and focal adhesion proteins ***(J Li et al. 2014 Nature)***.

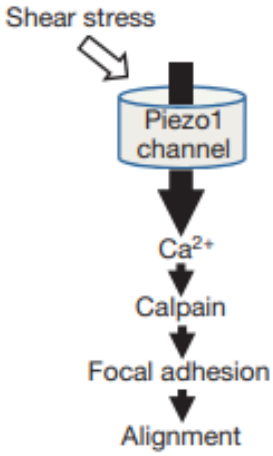

Fig. 13 Piezo1 coupling to calpain [Image from the paper: ***(J Li et al. 2014 Nature)****]*

3. Piezo1 mediates the stretch-induced progression of prostate cancer

In this case, the mechanical gating of the overexpressed Piezo1 in prostate cancer cells leads to Ca^{2+} influx which bind correspond effector molecules to trigger the activation of both Akt and mTOR, increasing the expression of cyclin D1 and CDK4 (the cell cycle key factors). From this respect, these intracellular signal transduction cascades may support the progression of prostate cancer ***(D De Felice et al. 2020 Cancers (Basel))***.

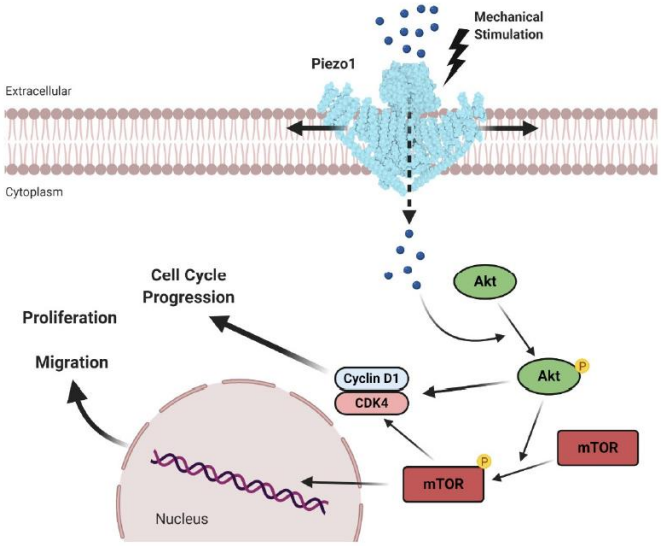

Fig. 14 Piezo1 mediates the stretch-induced progression of prostate cancer [Image from the paper: ***(D De Felice et al. 2020 Cancers (Basel))****]*

4.2 Ca^{2+} dynamics and phototransduction

Phototransduction, the process by which a photon of light is changed to an electrical signal, occurs in the photoreceptors. Retinal photoreceptors in all vertebrates are the rods and cones. Rods are responsible for dim-light vision due to the ability to detect and signal the absorption of a single photon while cones are less sensitive to light but adapt to steady light much more effectively than rods, thus responsible for bright-light vision. In rod photoreceptors, phototransduction takes place at the outer segment compartment filled with disks where visual pigments absorb light, initiating phototransduction cascades.

4.2.1 On off and tuning components in OS

$[Ca^{2+}]i$ of rod outer segment in darkness is thought to range from ~300 to ~ 500 nM, significantly higher than ~100nM in common cells. These Ca^{2+} levels are high enough to regulate the phototransduction machinery in the outer segment and transmitter release in the inner segment meanwhile are sufficiently low to avoid the neurotoxicity by higher Ca^{2+} concentration.

To maintain such constant resting Ca^{2+} concentration needs specialized on off and tuning components discussed below.

1. On components

Ca^{2+} entry of the rod outer segment is mediated by the CNG channels in darkness, which are kept open by the second messenger of phototransduction, cGMP. The concentration of cGMP is in turn regulated by dynamic equilibrium between synthesis (by a guanylyl cyclase, GC) and hydrolysis (by a phosphodiesterase, PDE). Of note, in the dark, CNG channels gated by cGMP allow a steady inward current, called the dark current, ~20% of which is contributed by Ca^{2+} influx, the rest by Na^{+} ***(S Das et al. 2021 Pflugers Arch)***.

CNG channels are heterotetrameric ion channels expressed in the OS membrane of rods and also cones. Rod photoreceptor CNG channel is composed of CNGA1 and long isoform of CNGB1 (CNGB1a) subunits expressed in a 3:1 ratio, whereas, in cone photoreceptors, CNG channel consists of CNGA3 and CNGB3 subunits in a 1:1 ratio ***(S Das et al. 2021 Pflugers Arch)***.

2. Off component

Currently, Ca^{2+} is extruded from the outer segment by two pathways, one is mediated by rod-specific Na^{+}/Ca^{2+}, K^{+} exchanger (NCKX1), which exchanges $4Na^{+}$ for one Ca^{2+} and one K^{+} and has been considered as the main pathway for Ca^{2+} extrusion; the other is through a NCKX-independent mechanism which was revealed recently from NCKX knock out mice ***(F Vinberg et al. 2018 Sci Rep)***.

3. Tuning component

Calcium binding proteins including buffers and sensors in rod outer segment are believed to bind and sequester up to 99% of Ca^{2+} which enters the cell through CNG channels. The buffering capacity of rod outer segment in the dark is estimated to be 20. The apparent diffusion coefficient of Ca^{2+} in rod outer segment cytoplasm, is calculated to be ~15 $\mu m^2 s^{-1}$, is similar to that measured in other systems ***(K Nakatani et al. 2002 Biophys J)***. This value is consistent with the effect of a low-affinity, immobile buffer reported to be present in the rod outer segment, suggesting the tuning components exert significant delay for the radial propagation of changes of Ca^{2+} ***(K Nakatani et al. 2002 Biophys J)***.

The tuning component contain plenty types of calcium binding proteins including calmodulin, recoverin, guanylyl cyclase activating proteins (GCAPs), parvalbumin, calbindin, calretinin ***(D Krizaj et al. 2002 Front Biosci)***.

4.2.2 Ca^{2+} dynamics and light responses

Within rod outer segment, the concentration of Ca^{2+} is change with the light responses. Light the responses of rod outer segment start from the activation of photo-transduction. The activation of the light-sensitive G-protein coupled receptor (R*) results in the activation of the G protein transducin which in turn, activates the effector enzyme phosphodiesterase (PDE6), leading to increased hydrolysis of cGMP and the consequent closure of CNG channels. Since Ca^{2+} extrusion through NCKX1 continues, the Ca^{2+} within rod outer segment decreases. Therefore, intracellular Ca^{2+} tends to drop down upon light responses, Interestingly, the Ca2+ concentration decline is biphasic, probably related to the presence of more than one Ca^{2+} buffer in the rod outer segment. Of note, Ca^{2+} concentration is not able to track the light-sensitive current. Actually, the light sensitive current recovers faster than the Ca^{2+} concentration, which is poorly understood. Anyway, the calcium dynamic with light response is important for recovery and adaptation following continuous light exposure ***(S Das et al. 2021 Pflugers Arch)***.

4.2.3 Modulation role of Ca^{2+} dynamics

The rapid light adaptation in rods is mediated primarily by change in the level of calcium driven by light. Calcium modulates the phototransduction cascades of rods through a timely feedback mechanism, which drives the prompt termination of the flash responses and shifts sensitivity of the photoreceptors to function over a wide dynamic range, hence mediating their adaptation to background light. This feedback between calcium changes and phototransduction can be reflected in following aspects.

1. Modulation of guanylyl cyclase activating proteins (GCAPs) by calcium

The most important factor which affects the adaptation of rods photoreceptors is the synthesis rate of cGMP by GCs, which is regulated by the Ca^{2+}-binding proteins GCAP1 and GCAP2. High Ca^{2+} in the dark will inhibit activation of GCs due to Ca^{2+} binding of GCAPs, while decreased Ca^{2+} caused by light response will cause the dissociation of Ca^{2+} from GCAPs which bind Mg^{2+} instead, accelerating the synthesis rate of cGMP by GCs. Consequently, more CNG channels are kept opened under the new illumination condition, which drives the faster recovery of the dark current, hence extending the functional range of photoreceptors ***(F Vinberg et al. 2018 Sci Rep)***.

2. Modulation of recoverin by calcium

The lifetime of the photoactivated visual pigment is controlled by the rhodopsin kinase. The latter is regulated by recoverin which inhibits rhodopsin kinase when binding Ca^{2+} under high Ca^{2+} concentration in darkness. This inhibit result in delayed visual pigment phosphorylation. The low level of Ca^{2+} under light adaptation will make and maintain more active kinases and lead to faster turnover of functional visual pigment ***(F Vinberg et al. 2018 Sci Rep)***.

3. Modulation of CNG channels by calcium

Another mechanism by which calcium modulates the light response is related to the conductance of the CNG channels, which can be indirectly regulated by Ca^{2+}. Since the CNG channels contain binding site for Ca^{2+}-Calmodulin, calmodulin binds with Ca^{2+} at high level of Ca^{2+} and occupy the CNG channels, causing decreasing conductance of the CNG channels. On the other hand, calmodulin is released from the channel in low Ca^{2+} during light adapted condition, the affinity of the channel for cGMP then will be kept relatively high, eventually increasing the

dark current ***(F Vinberg et al. 2018 Sci Rep)***.

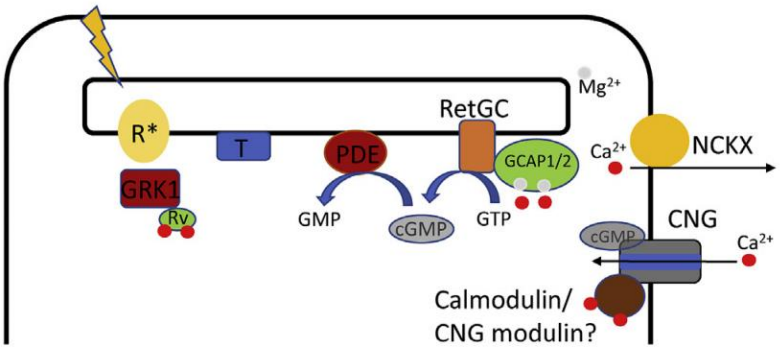

Fig. 14 Mechanisms of modulation of the phototranstuction in rods by calcium [Image from the paper: ***(F Vinberg et al. 2018 Sci Rep)****]*

4.3 Ca^{2+} dynamics and glioma malignancy

Gliomas are tumors that arise from glial precursor cells originating from the brain and the spinal cord, which can be classified four grades based on the clinical diagnostic criteria of the World Health Organization (WHO): grade I/II (low grade) and grade III/IV (high grade). Particularly, Grade IV gliomas are predominantly glioblastoma multiforme (GBMs), the most malignant glioma, which a highly undifferentiated and progresses very aggressively.

More and more evidences show that Ca^{2+} play significant roles in various aspects of cancers. Ca^{2+} dynamics controlled by the on, off and tuning components is often exploited by cancer cells like gliomas as tools to promote notably their proliferation and invasion. Different types of tumors may have their distinct ways to make use of the combinations of on, off and tuning components to enhance malignancy. The follow is the introduction the on, off and tuning components involving the glioma malignancy, with a focus on those related to glioblastoma (especially, U87 MG cells) malignancy.

4.3.1 On components

1. TRPC6 channels

It was reported that some members of TRPC family channels are related to cell cycle progression and in the development of human glioma. Based on assessment

of TRPC6 protein and mRNA expression in in human glioma cell including U87 MG, functional TRPC6 was found overexpressed and inhibition of TRPC6 activity suppressed cell growth and clonogenic ability, induced cell cycle arrest at the G2/M phase, suggesting TRPC6 channels were essential for glioma development via regulation of G2/M phase transition *(X Ding et al. 2010 J Natl Cancer Inst)*.

2. T-type Ca^{2+} channels

Endostatin is a C-terminal proteolytic fragment of collagen XVIII with promising antitumor properties. Using cell proliferation and migration assays, patch clamp and Western blot analysis, it was shown the endostatin could be modulated by T-type Ca2+ channels, thus mediating the antitumor effect of endostatin through inhibiting the proliferation and migration of human glioblastoma U87 MG cells, which is consistent with the results from the other group at the same time *(G Santoni et al. 2012 Br J Pharmacol, Y Zhang et al. 2012 Br J Pharmacol)*.

Of note, recently, a murine GBM xenograft via subcutaneous injection of U87 MG GBM cells was generated as the animal model to study the effect of T-type Ca2+ channels on the tumor size. The result showed that tumor size was reduced when Ca(v)3.1 expression was silenced, which is accompanied by transcriptional downregulation of p62/SQSTM1 and deficient autophagy *(A Visa et al. 2019 Cancer Res)*.

3. Store Operated Channels

As an ER Ca2+ sensor and activator of SOCE, STIM1 was reported to be overexpressed in in a panel of human glioblastoma cell lines including U251, U87 MG and U373, with highest expression in U251. Specific downregulation of STIM1 inhibited U251 cell proliferation by arresting cell cycle in G0/G1 phase *(G Li et al. 2013 J Exp Clin Cancer Res)*.

Interestingly, another investigation on the roles SOCs in the modeled micro-gravity (MMG) mediated inhibit of cell proliferation and attenuate the metastasis potential in U87 MG cells showed that MMG stimulation inhibited the invasion and migration potentials of U87 MG cells by downregulating the expression of Orail and sequentially decreasing the SOCE *(ZX Shi et al. 2015 Biochem Biophys Res Commun)*.

4. TRPM7

Aberrant expression of the TRPM7 channel has been linked to GBM functions, using the human GBM cell line U87 MG, TRPM7 activator naltriben on GBM viability, migration, and invasiveness was investigated using whole-cell patch-clamp technique, cell migration and invasion assays, as well as Western

immunoblots. It was proved that naltriben enhanced the MAPK/ ERK signaling pathway, suggesting upregulating TRPM7 activities contributes to migration and invasion of GBM *(R Wong et al. 2017 Oncotarget)*. Importantly, the subsequent experiments with treatment of waixenicin A (a specific TRPM7 antagonist) showed a reduction of GBM cell viability, migration, and invasion of GBM cell lines U87 MG or U251.Further, on an intracranial xenograft GBM mouse model treated with the drug showed there was increased cleaved caspase 3 activity, alongside reduction in Ki-67, cofilin, and Akt activity in vivo *(R Wong et al. 2020 Cell Calcium)*.

4.3.2 Off components

1. Na^+/Ca^{2+} exchanger (NCX)

The expression of NCX in glioblastoma cells was significantly higher than in normal human astrocytes. The role of the NCX on the effect on human glioblastoma growth was investigated combining with use of SKF 96365, a well-known suppressor of human glioblastoma. Using assays on cell cycle and cell viability, Western blot, Ca^{2+} imaging, patch clamp recordings and siRNA gene knockdown, it was demonstrated that the effect of SKF 96365 primarily resulted from enhanced reverse operation of the Na^+/Ca^{2+} exchanger (NCX), causing the intracellular Ca^{2+} accumulation and cytotoxicity, thus leading to arresting the glioblastoma cells in the S and G(2) phases and activating p38-MAPK and JNK *(M Song et al. 2014 Br J Pharmacol)*. This result, to some extent, is consistent with previous studies which proved that in human glioblastoma cells including U87 MG, the killing effect of certain drugs which specifically suppresses human malignant glioma among normal astrocytes was at least also mediated by sodium-calcium exchanger by disrupted the Ca^{2+} extrusion, though different mechanisms are involved *(W Harley et al. 2010 Brain Res, Y Shono et al. 2010 Cell Mol Neurobiol)*. Of note, latest research has proved that the growth of glioblastoma cells is suppressed by blockade of the forward Na^+/Ca^{2+} exchangers through Ca^{2+}-mediated cell death, which was confirmed by various kinds of approaches in vitro like patch-clamp recording, Ca^{2+} imaging, flowcytometry, and Western blot, as well as in vivo in which systemic administration of bepridil inhibited growth of brain-grafted glioblastoma *(HJ Hu et al. 2019 Br J Pharmacol)*.

2. SERCA

It was found the resting $[Ca^{2+}]_i$ and basal Ca^{2+} influx is increased in glioblastoma cell lines compared with human primary astrocytes. And the ER Ca^{2+} store was found to be increased in both GBM cell lines and in primary GBM cells. Meanwhile,

inhibition of SERCA function revealed a fundamental difference in intracellular Ca^{2+} homeostasis in tumor cells compared with normal human astrocytes, which are required to elucidate the underlying molecular differences ***(GG Kovacs et al. 2005 Am J Physiol Cell Physiol)***.

3. MCU

Latest research showed that mitochondrial Ca^{2+} uniporter (MCU) is overexpressed, which is associated with unusual $[Ca^{2+}]_i$ elevation in GBM including U87 MG cells. The roles of MCU in GBM malignancy was confirmed by a series of experiments involving MCU silencing which decreases proliferation and alters $[Ca^{2+}]_i$ dynamics in U87 MG GBM cells, and MCU overexpression which increases $[Ca^{2+}]_i$ elevation in human astrocytes (HAs), thus suggesting expression level of MCU, involving in intracellular Ca^{2+} regulation, influences GBM cell proliferation, contributing to GBM malignancy ***(X Li et al. 2020 J Cell Sci)***.

4.3.3 Tuning components

1. Calmodulin

Calmodulin (CaM) is an important calcium sensor, many studies have revealed CaM is involved in regulating cell proliferation, programmed cell death, and autophagy in cancer. Particularly, CaM is strongly associated with the invasive nature of GBM since it is found that CaM concentration was obviously related to the invasive capacity of and invadopodia formation by different GBM cell lines, which can be suppressed by a small hairpin RNA or a pharmacological inhibitor targeting CaM. CaM knockdown even exerted a strong anti-invasive effect on GBM in vivo ***(T Li et al. 2018 Cell Death Dis)***.

2. Annexin

Annexin is a Ca^{2+}-binding cytoskeletal protein expressed on the surface of endothelial cells, macrophages, mononuclear cells and various types of cancer cells. In various types of cancer, the expression of members of the annexin family is dysregulated. Annexin-1 (ANXA1) is frequently amplified in primary gliomas involving in proliferation, differentiation and apoptosis. It was shown primary glioblastomas had a higher annexin-1 expression level compared with secondary glioblastomas, suggesting that annexin-1 upregulation in astrocytoma may contribute to tumor progression ***(J Schittenhelm et al. 2009 Mod Pathol)***. In addition to annexin 1, it has been also reported that Annexin 2A (ANXA2) is overexpressed in

GBM and positively correlates with tumor aggressiveness and patient survival *(F Maule et al. 2016 Oncotarget)*. Recently, it was revealed that, in U87 MG cells, knockdown of ANXA2 inhibited the proliferation and decreased phosphorylated signal transducer and activator of transcription 3 and cyclin D1 expression, leading to impedance of the G1 to S phase transition *(L Chen et al. 2019 Oncol Rep)*. Latest research suggested the overexpression of ANXA2 promotes proliferation of glioma cells by forming a GPC1/c-Myc positive feedback loop, which could be a potential biomarker for predicting prognosis of glioma patients *(X Li et al. 2021 Cell Death Dis)*.

In addition to tuning components above, other calcium binding proteins are potent modulators involving glioblastoma malignancy, such as S100A9 *(N Huang et al. 2013 Eur J Cancer Prev)*, S100A4 *(K Takenaga et al. 2007 Neurobiol Dis, D Aguilar-Morante et al. 2015 Oncotarget)*, S100B *(E Dagdan et al. 2011 Am J Med Genet B Neuropsychiatr Genet)*, Sorcin *(B Shabnam et al. 2018 Transl Oncol)*.

Results

Calcium flares and compartmentalization in rod photoreceptors

(MS Published in *PNAS*)

Calcium flares and compartmentalization in rod photoreceptors

Yunzhen Li[a,1], Fabio Falleroni[a,1], Simone Mortal[a,1], Ulisse Bocchero[a,1,2], Dan Cojoc[b], and Vincent Torre[a,c,3]

[a]Neurobiology Department, International School for Advanced Studies (SISSA), Trieste 34136, Italy; [b]Institute of Materials, National Research Council of Italy (CNR), 34149 Trieste, Italy; and [c]Joint Laboratory of Biophysics and Translational Medicine, Institute of Systems Medicine (ISM)–SISSA, 215123 Suzhou, Jiangsu, P. R. China

Edited by Gordon L. Fain, University of California, Los Angeles, CA, and accepted by Editorial Board Member Jeremy Nathans July 20, 2020 (received for review March 14, 2020)

Rod photoreceptors are composed of a soma and an inner segment (IS) connected to an outer segment (OS) by a thin cilium. OSs are composed of a stack of ∼800 lipid discs surrounded by the plasma membrane where phototransduction takes place. Intracellular calcium plays a major role in phototransduction and is more concentrated in the discs, where it can be incorporated and released. To study calcium dynamics in rods, we used the fluorescent calcium dye CaSiR-1 AM working in the near-infrared (NIR) (excitation at 650 and emission at 664 nm), an advantage over previously used dyes. In this way, we investigated calcium dynamics with an unprecedented accuracy and most importantly in semidark-adapted conditions. We observed light-induced drops in $[Ca^{2+}]_i$ with kinetics similar to that of photoresponses recorded electrophysiologically. We show three properties of the rods. First, intracellular calcium and key proteins have concentrations that vary from the OS base to tip. At the OS base, $[Ca^{2+}]_i$ is ∼80 nM and increases up to ∼200 nM at the OS tip. Second, there are spontaneous calcium flares in healthy and functional rod OSs; these flares are highly localized and are more pronounced at the OS tip. Third, a bright flash of light at 488 nm induces a drop in $[Ca^{2+}]_i$ at the OS base but often a flare at the OS tip. Therefore, rod OSs are not homogenous structures but have a structural and functional gradient, which is a fundamental aspect of transduction in vertebrate photoreceptors.

photoreceptors | calcium | phototransduction

Rod outer segments (OSs) are composed of a stack of ∼800 lipid discs surrounded by the plasma membrane where the phototransduction machinery is located (1, 2). The OS is connected to the soma through a narrow structure called the cilium (3), providing an electrical connection so that electrical signals generated in the OS are transmitted to the soma. The soma is composed of an inner segment (IS) containing the nucleus and from which the synaptic terminals protrude. The OS is not a well-mixed compartment and appears to be rather inhomogeneous: The composition of the disk membrane varies from the base of the OS (where new discs are synthesized) to its tip (where old discs are continuously shed) (4–8).

The complex dynamics of disk renewal and the changes in disk composition along the OS suggest a variable efficiency of phototransduction. Indeed, some classic (9, 10) and more recent (11) works have shown that the amplitude of the single photoresponse and of the maximal photoresponse is higher at the base and two to three times smaller at the OS tip (12). The unequal sensitivity along the OS could be related to the availability of metabolic energy in the form of NADPH. Indeed, Miyagishima et al. have shown that the recovery of sensitivity after light stimuli is slower at the OS tip than at its base (13). Furthermore, localized light-induced changes in cGMP and Ca^{2+} concentrations decay along the OS from the point of stimulation, suggesting a mechanism that limits the spread of adaptation to light (14).

In this context, Ca^{2+} plays a fundamental role in regulating light adaptation (15, 16), recovery after pigment bleaching (17, 18), and OS structural stability (19, 20). To study calcium along the OS, we used CaSiR-1 AM (excitation 650 nm, emission 664 nm) (21) and Fura Red (excitation 440 and 480 nm, emission ∼650 nm); we analyzed its intracellular dynamics in dissociated rod photoreceptors composed of an IS and an OS (IS+OS) and in small pieces of retina obtained from *Xenopus laevis* frogs. CaSiR-1 increases fluorescence emission upon binding calcium, while Fura Red decreases its emission following binding to calcium. The excitation with Fura Red at two wavelengths allows a quantitative estimation of intracellular calcium by what is referred to as ratiometric calcium imaging (22). Conversely, CaSiR-1 AM allows the study of calcium dynamics in rods under semidark-adapted conditions.

This dye has only recently been used to investigate Ca^{2+} in rod photoreceptors (23). In rods loaded with CaSiR-1, we directly observed a light-induced drop in fluorescence, with kinetics very similar to that of photoresponses recorded electrophysiologically. Therefore, it is possible to follow calcium dynamics using an excitation light at 650 nm, which reduces the amplitude of a saturating photoresponse induced by a flash of light at 488 nm of approximately ∼30–40%. The use of CaSiR-1 allowed us to study Ca^{2+} in rods with unprecedented accuracy and resolution and in semidark-adapted conditions.

Our experiments highlight several properties of rods: First, OSs have a strong gradient not only in responsiveness but also in $[Ca^{2+}]_i$, which is higher at the tip than at the OS base; second, in

Significance

Rod photoreceptor outer segments (OSs) are specialized ciliary architectures. Our imaging experiments reveal three properties of rods. First, intracellular calcium and key proteins have a concentration varying from the OS base to the tip. At the OS base, $[Ca2+]_i$ is approximately 80 nM and increases up to ∼200 nM at the OS tip; second, there are spontaneous calcium flares in functional OSs, and these flares are highly localized and are more pronounced at the OS tip; third, a bright flash of light at 488 nm induces a drop in $[Ca2+]_i$ at the OS base but often a flare at the OS tip. This structural and functional gradient of the phototransduction machinery is a fundamental aspect of transduction in vertebrate photoreceptors.

Author contributions: U.B. and V.T. conceived and discussed the idea; F.F., S.M., U.B., and V.T. designed research; Y.L., F.F., S.M., and U.B. performed research; Y.L., F.F., S.M., and U.B. analyzed data; and S.M., U.B., D.C., and V.T. wrote the paper.

The authors declare no competing interest.

This article is a PNAS Direct Submission. G.L.F. is a guest editor invited by the Editorial Board.

[1]Y.L., F.F., S.M., and U.B. contributed equally to this work.

[2]Present address: Photoreceptor Physiology Group, National Eye Institute (NEI), NIH, Bethesda, MD 20892.

[3]To whom correspondence may be addressed. Email: torre@sissa.it.

This article contains supporting information online at https://www.pnas.org/lookup/suppl/doi:10.1073/pnas.2004909117/-/DCSupplemental.

semidark-adapted conditions, it is possible to observe spontaneous calcium flares, i.e., highly localized increases in $[Ca^{2+}]_i$ in healthy and functional rods; third, at the OS tip, a bright flash of light often induces a calcium flare and not a drop in $[Ca^{2+}]_i$.

Results

Strong Calcium Gradient in the Rod OS. When a dark-adapted retinal rod of a small piece of retina loaded with CaSiR-1 was briefly illuminated with 650-nm light, the rod ISs appeared rather bright (*SI Appendix*, Fig. S1*A*). However, the OSs displayed a gradient of fluorescence that increased in intensity from the base to the tip of the rod (*SI Appendix*, Fig. S1*A*). When the CaSiR-1–loaded retinas were mechanically dissociated, the observation dish was full of isolated OS, which were uniformly bright (*SI Appendix*, Fig. S1*B*). The OSs that were still attached to the IS (IS+OS) displayed the same gradient of fluorescence observed in intact rods, which was more intense at the tip and decreased toward the base (Fig. 1*A*). The profile of fluorescence was similar in IS+OS rods across preparations, but the level of fluorescence at the base varied (Fig. 1*B*). IS+OS rods showing a clear gradient in CaSiR-1 fluorescence were usually functional: Illuminating these rods with a brief flash of light at 488 nm, we were able to measure a transient decrease of the emitted fluorescence on the order of 0.02–0.05 *DF/F* ((fluorescence at time t − fluorescence at time 0)/fluorescence at time 0), which was an indication of a light-induced drop in intracellular calcium (Fig. 1*C*). The time course of the change in *DF/F* was reminiscent of that observed in electrical recordings of photoresponses (23) (*SI Appendix*, Fig. S2*A*).

The steady light at 650 nm used to excite CaSiR-1 was approximately equivalent to 480 $R^*{\cdot}rod^{-1}{\cdot}s^{-1}$ and reduced the circulating dark current by ∼30–40% (*SI Appendix*, Fig. S2*B*), indicating that CaSiR-1 allowed resolution of calcium dynamics in semidark-adapted conditions. The ratio between functional IS+OS rods and the total rods present in the preparations, shown in Fig. 1*D*, indicates that our samples were relatively homogeneous across the experiments. Isolated OS or IS+OS rods not showing the brightness gradient along the OS (Fig. 1 *E* and *F*) did not show any light response and were considered nonfunctional (Fig. 1*H*). To check whether the brightness gradient seen in the OS of IS+OS rods was caused by a different loading, we repeated the same experiment by loading retinas with Fura Red. In this case, the fluorescence was brighter at the base and decreased toward the tip (Fig. 1*G*). Experiments of ratiometric calcium imaging using Fura Red indicate that in light-adapted conditions, $[Ca^{2+}]_i$ is approximately ∼80 nM at the base and ∼200 nM at the tip (*SI Appendix*, Fig. S3) and that its mean value is in the range of what has been previously reported (24). These results show that $[Ca^{2+}]_i$ is not homogeneous inside the rod OS and has a strong gradient.

Strong Gradient of Light Responsiveness. We stimulated isolated IS+OS rods with diffuse light at 488 nm (Fig. 2*A*) and measured CaSiR-1 fluorescence emitted at the base (Fig. 2 *B* and *E* dark red), the center (Fig. 2*B*, orange), and at the tip (Fig. 2*B*, green). We observed a clear light-induced decrease in *DF/F* in each rod compartment, but the drop in *DF/F* was larger at the base than at the tip ($(DF/F)_{base} - (DF/F)_{tip}$, or gradient in responsiveness for simplicity) (Fig. 1*C*) ($n = 15$; $P < 0.001$). This gradient in responsiveness along the OS is in agreement with the drop in sensitivity observed with electrical recordings with localized spots of light, along the OS (11). Interestingly, the drop in responsiveness was larger in intact rods from pieces of retina (hereafter referred to as "intact retinal rods") (Fig. 2 *D–F*), suggesting an important role for the integrity of the retinal tissue. In some of these rods, following a flash at 488 nm, no visible decrease in

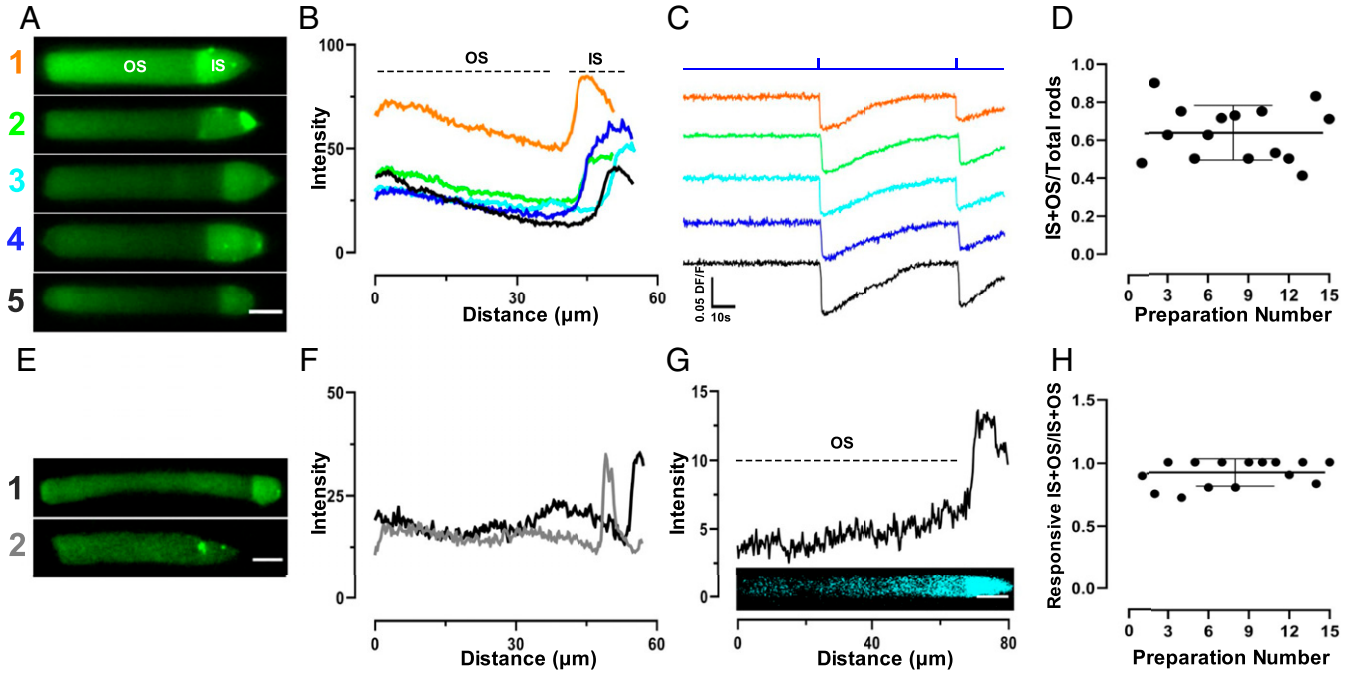

Fig. 1. Light-evoked calcium drops in IS+OS rods. (*A*) Fluorescence images of isolated IS+OS rods loaded with CaSiR-1. The IS is usually brighter than the OS. (*B*) Fluorescence intensity profile for the five IS+OS rods shown in *A*. (*C*) Light-evoked fluorescence drops evoked by a flash of light of 1 s, eliciting ∼2,100 R* per rod at 488 nm at the times indicated by the blue trace at the top of the image. The slight decrease of *DF/F* observed at the second flash of light is caused by dye bleaching. In *A–C*, the same color corresponds to the same rod. (*D*) Ratio of the number of isolated IS+OS over the total number of rods present in the preparations ($n = 15$ experiments, 0.6368 ± 0.145). (*E*) Example of two unresponsive rods. (*F*) As in *B* but for two IS+OS shown in *E*. (*G*) Fluorescence intensity profile for an IS+OS rod loaded with Fura Red in light-adapted conditions. *Top* is the intensity profile, and at *Bottom* is the fluorescence image. In this case, the base of the OS is brighter than the tip. (Scale bars, 10 μm.) (*H*) Responsiveness ratio between IS+OS rods ($n = 15$ experiments, 0.92 ± 0.108).

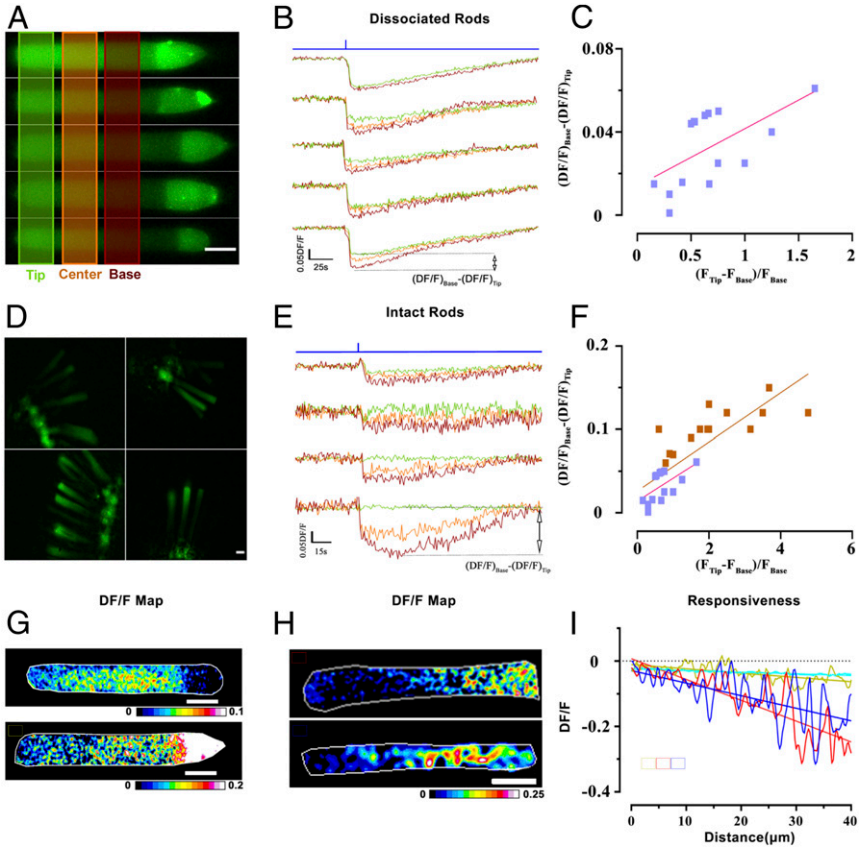

Fig. 2. Gradient of light-evoked calcium drops. (*A*) Rods fluorescence images of Fig. 1*A*. The green (tip), orange (center), and dark red (base) semitransparent stripes indicate the regions of the OS. (*B*) Light-evoked *DF/F* drops, for five rods in *A*, at the tip, center, and base (traces colors as stripes in *A*). The evoked *DF/F* of the three regions are superimposed. Light stimulus of 1 s, eliciting ~2,100 R* per rod. (*C*) Relation between calcium gradient ($DF/F_{base} - DF/F_{tip}$) and response gradient ($(F_{tip} - F_{base})/F_{base}$) for $n = 15$ rods. The straight red line is a linear fit given by $y = 0.02075 \times x + 0.03047$ (R^2: 0.3431). Fluorescent images pieces of retina loaded with CaSiR-1 (*D*): DF/F for intact retinal rods ($n = 4$) at the base, center, and tip with diffuse illumination and the same color coding as in *B* (*E*). (*F*) Fit for intact retinal rods ($n = 15$, brown points) superimposed over the graph in *C*; the straight brown line is a linear fit given by $Y = 0.02945*X + 0.02607$ (R^2: 0.6707). (*G*) Gradients of responsiveness of two dissociated rods (scale bar *DF/F*). (*H*) Gradients of responsiveness of two rods from pieces of retinas. (*I*) Dependence of responsiveness (*DF/F*) along the OS length for *G* and *H*. (Scale bars, 10 μm.).

fluorescence was detected at the tip of the OS (Fig. 2*E*, green trace). However, a clear decrease in fluorescence was observed at the base of the OS (Fig. 2*E*, dark red trace) ($n = 15$; $P < 0.001$).

Collected data from 15 IS+OS rods and 15 intact retinal rods showed that the drop in responsiveness was correlated to the relative amplitude of increase of the fluorescence emitted by CaSiR-1 ($(F_{tip} - F_{base})/F_{base}$) at the OS tip (Fig. 2 *C* and *F*), mirroring the increase of $[Ca^{2+}]_i$ measured with Fura Red (Fig. 1*G* and *SI Appendix*, Fig. S3). A better visualization of the gradient in responsiveness is obtained by the map of *DF/F*, where *F* is the fluorescence in a time window of 1 s before the light flash at 488 nm and *DF* is the fluorescence drop caused by the light in a time window of 1 s centered around the time of maximum fluorescence drop. This map was obtained in dissociated rods (Fig. 2*G*) and in rods from pieces of retinas (Fig. 2*H*), showing a clear gradient in responsiveness falling at the center of the OS. From these maps, we obtained the profile of responsiveness along the OS by averaging the values of *DF/F* along the direction perpendicular to the OS (Fig. 2*I*).

To analyze in greater detail the time course of the light-induced calcium changes, we averaged the light-induced drop in fluorescence over the first five photoresponses. The emitted fluorescence and possibly $[Ca^{2+}]_i$ fell with a fast and a slower component (*SI Appendix*, Fig. S2 *A–C*), as predicted from the model of ref. 16. The fast drop in calcium was caused by the closure of light-sensitive channels permeable to Ca^{2+} ions, and the slower component was associated with the dynamics of intracellular (native and exogenous, such as the introduced dye) Ca^{2+} buffers.

The experiments illustrated in Figs. 1 and 2 were obtained with diffuse illumination at 488 nm. To explore the response to highly localized flashes of light, we used a confocal microscope allowing illumination with blue light at 488 nm of specific regions of the OS (see colored boxes in Fig. 3 *A* and *B*, *Left*). When we illuminated a region of ~5 × 5 μm^2 at the base (Fig. 3*A*), we observed a clear light-induced calcium decrease, whereas no response at the center or at the tip of the OS was detected. We also illuminated the bright IS with the same light, and we could not detect any light-induced fluorescence decrease (Fig. 3*B*). We constructed a map of responsiveness along the OS when the same spot of illuminating light was moved along its axis. Data collected from six experiments showed that with confined illumination, there was a marked decrease in responsiveness from the base to the tip of the OS (Fig. 3*C*) ($n = 6$; $P < 0.001$). The trend of responsiveness obtained with localized illumination was similar to that obtained with diffuse illumination, but in this case the change in fluorescence was measured in localized regions.

Spontaneous Calcium Flares. During imaging recordings (~8–15 min) of the fluorescence emitted by CaSiR-1, we observed spontaneous calcium flares i.e., spontaneous bursts of increased

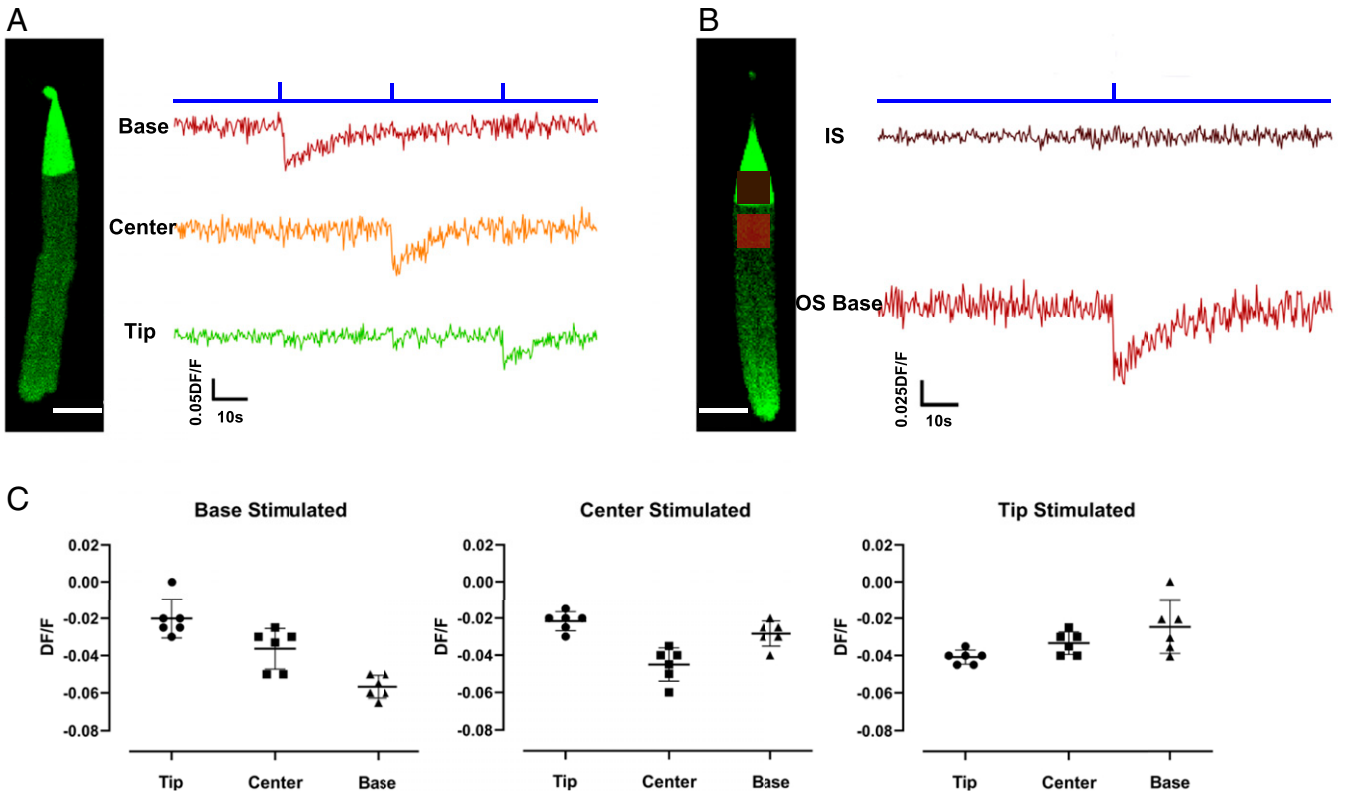

Fig. 3. Calcium drops in response to localized illuminations. (*A*) The fluorescence image shows an example of an IS+OS rod loaded with CaSiR-1 and the colored boxes indicate where the localized illumination of 1 s at the base (dark red), center (orange), and tip (green), eliciting ~1,500 R* per rod was applied. Colored traces were obtained from averaging fluorescence changes inside the boxes on the *Left* with the same color. The blue line indicates the timing of the localized illumination. (*B*) As in *A* but for a localized illumination of the IS (brown) and the OS base (dark red). (*C*) Quantification of the *DF/F* changes in response to localized stimuli ($n = 6$; base stimulation *DF/F*: $mean_{base}$ −0.057 ± 0.002 SEM, $mean_{center}$ −0.036 ± 0.004 SEM, $mean_{tip}$ −0.020 ± 0.004 SEM; center stimulation *DF/F*: $mean_{base}$ −0.028 ± 0.003 SEM, $mean_{center}$ −0.045 ± 0.004 SEM, $mean_{tip}$ −0.022 ± 0.002 SEM; tip stimulation *DF/F*: $mean_{base}$ −0.024 ± 0.006 SEM, $mean_{center}$ −0.033 ± 0.002 SEM, $mean_{tip}$ −0.041 ± 0.002 SEM; Student's *t* test $mean_{tip}$ (tip stimulation) vs. $mean_{base}$ (base stimulation) $P < 0.001$). (Scale bars, 10 μm.)

fluorescence, both in isolated rods (Fig. 4 *A* and *B*) and in intact retinal rods (Fig. 4*C*). These flares (see red stars in Fig. 4*A*) occurred more often at the tip than at the center or base of the rods, and only occasionally spontaneous flares were seen at the base of the rods. The rods that exhibited calcium flares were functional, and a bright flash at 488 nm induced the expected drop in intracellular calcium (Fig. 4*A*). Calcium flares in isolated rods (Fig. 4*B*) and in intact retinal rods (Fig. 4*C*) had a similar amplitude, occurred preferentially at the tip, and occasionally could also be seen in the IS (see bottom traces in Fig. 4 *B* and *C*).

Calcium flares could be triggered by light flashes at 488 nm. In the experiment illustrated in Fig. 4 *D* and *E*, diffuse light flashes induced the usual drop in intracellular calcium at the base of the OS (dark red trace), but at the center of the OS, we measured a large increase in *DF/F* of ~0.45 (orange trace in Fig. 4*E*) (*SI Appendix*, Fig. S4). The occurrence of these flares was not associated with the death of the rod, as after the appearance of one flare, it was still possible to observe a light-induced calcium decrease (Fig. 4 *D* and *E*). The calcium flare occurring in the middle of the OS remained localized and did not propagate to the neighboring portion of the OS. Similarly, flares occurring in the IS did not propagate in any appreciable way into the OS. In several of these experiments, we collected not only fluorescence images (Fig. 4 *F*, *Left*) but also bright field images (Fig. 4 *F*, *Right*) of the rod, verifying the physical integrity of the rod during and after a calcium flare. We mapped the localization of both flares, spontaneous as well as induced by a 488-nm flash light along the OS and collected data from 30 experiments, showing that these flares occurred primarily at the tip of the OS (Fig. 4*G*). Flares were similar in dissociated (Fig. 4*H*) and intact rods (Fig. 4*I*) (*SI Appendix*, Fig. S5). Therefore, transient and spontaneous bursts of $[Ca^{2+}]_i$ occurring in the OS, primarily at its center and tip, occurred in healthy rods with similar properties in dissociated and intact retinal rods. It is possible, however, that these $[Ca^{2+}]_i$ flares occur at locations inside the OS where the phototransduction pathways physiologically lose their efficiency.

Coupling of Calcium in the OS and IS. The OS and IS are connected by the cilium, which allows the transmission of electrical signals generated in the OS to the IS (25). The cilium also allows the migration of large proteins synthesized in the nucleus necessary for the maintenance of the biological integrity of the OS (26). Therefore, it is of interest to see how changes in intracellular calcium occurring in the OS or IS propagate through the cilium. We recently showed that a single stimulation or a train of three mechanical stimulations of ~15 pN locally applied either to the IS or OS induce a transient and localized increase in $[Ca^{2+}]_i$ (23). Therefore, it is possible to induce localized transient increases in $[Ca^{2+}]_i$ by mechanical stimulations and by light flashes, allowing the propagation of $[Ca^{2+}]_i$ transients through the cilium to be investigated. As shown in Fig. 5, localized increases in $[Ca^{2+}]_i$ caused by the mechanical stimulation of either the OS (Fig. 5*A*) or the IS (Fig. 5*B*) do not propagate across the cilium. Similarly, a green light at 488 nm induces a drop in $[Ca^{2+}]_i$ at the base of the OS, which does not propagate to the IS

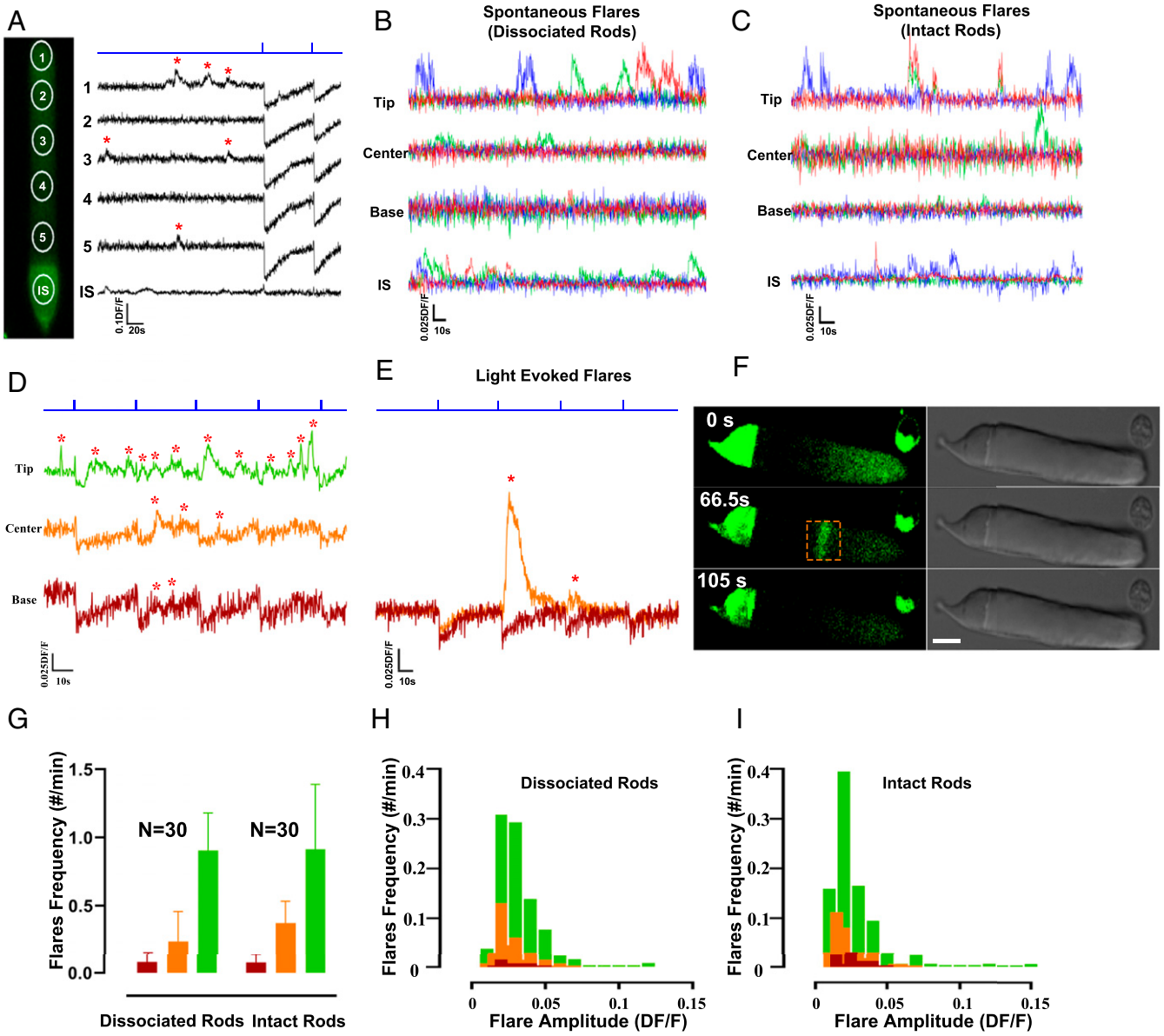

Fig. 4. Calcium flares. (*A*) IS+OS loaded with CaSiR-1. DF/F from five regions circled, showing spontaneous flares (red stars). Immediately after, two light-evoked *DF/F* drops. Light flashes of 1 s, eliciting ~2100 R* per rod; timing indicated by blue trace. (*B* and *C*) Magnification of the *DF/F* changes induced by spontaneous flares in isolated rods (*B*) and in rods from pieces of retina (*C*). Different colors represent different rods. (*D*) Spontaneous flares and light-evoked drops of *DF/F* at the tip, center, and base of an intact rod. (*E*) Light-evoked calcium flares. Light flashes in *A*. (*F*) Fluorescence and DIC images before, during, and after the calcium flare shown in *E*. The calcium flare (red box) remained localized and the rod remained unaltered. (Scale bar, 10 μm.) (*G*) Occurrence of calcium flares in isolated rods and pieces of retinas. Dissociated IS+OS $n = 30$, flare frequency: $\text{mean}_{\text{base}}$ 0.081 ± 0.03 SEM, $\text{mean}_{\text{center}}$ 0.238 ± 0.089 SEM, mean_{tip} 0.905 ± 0.112 SEM, $P < 0.001$ tip vs. base; intact retinal rods $n = 30$, flare frequency: $\text{mean}_{\text{base}}$ 0.077 ± 0.024 SEM, $\text{mean}_{\text{center}}$ 0.372 ± 0.066 SEM, mean_{tip} 0.914 ± 0.194 SEM, $P < 0.001$ tip vs. base. (*H* and *I*) Frequency of spontaneous calcium flares with an amplitude equal to DF/F at tip (green), center (orange), and base (dark red) in dissociated IS+OS ($n = 30$) and pieces of retinas ($n = 30$).

(Fig. 5*C*). Therefore, the cilium acts as a powerful blocker of calcium propagation flow between the OS and IS. The blockage of calcium propagation across the cilium could be caused by buffering organelles around it (27). Therefore, we tested the buffering ability of mitochondria by using the MitoTracker mitochondrial label. We found clusters of mitochondria in the IS close to the cilium (a comparison of the bright field images with the Red staining of mitochondria is shown in Fig. 5*D*). A similar observation has already been made in cones where mitochondria form a dense cluster that acts as a diffusion barrier between the OS and the IS (28). These mitochondria were mobile and moved by 1–3 microns per minute, remaining localized in the IS. However, a bright flash of light at 488 nm (see the blue arrow in Fig. 5*E*) drove the mitochondrial motion in a direction opposite to the location of the cilium and the OS (Fig. 5 *E*, *F*, *J*, and *K*) (*SI Appendix*, Fig. S6). These results suggest that mitochondria in the rod IS could be the molecular structures impeding the flow of intracellular calcium between the OS and IS and that their location could be modified by light.

Structural and Functional Gradient in the OS. To confirm and analyze the presence of the structural gradient along the OS, we examined the longitudinal profile of some components of the cytoskeleton and of the cell membranes. We found that the concentration of actin (Fig. 6 *A*, *D*, and *G*); tubulin (Fig. 6 *B*, *E*, and *H*), and cholesterol (Fig. 6 *C*, *F*, and *I*) along the OS is not

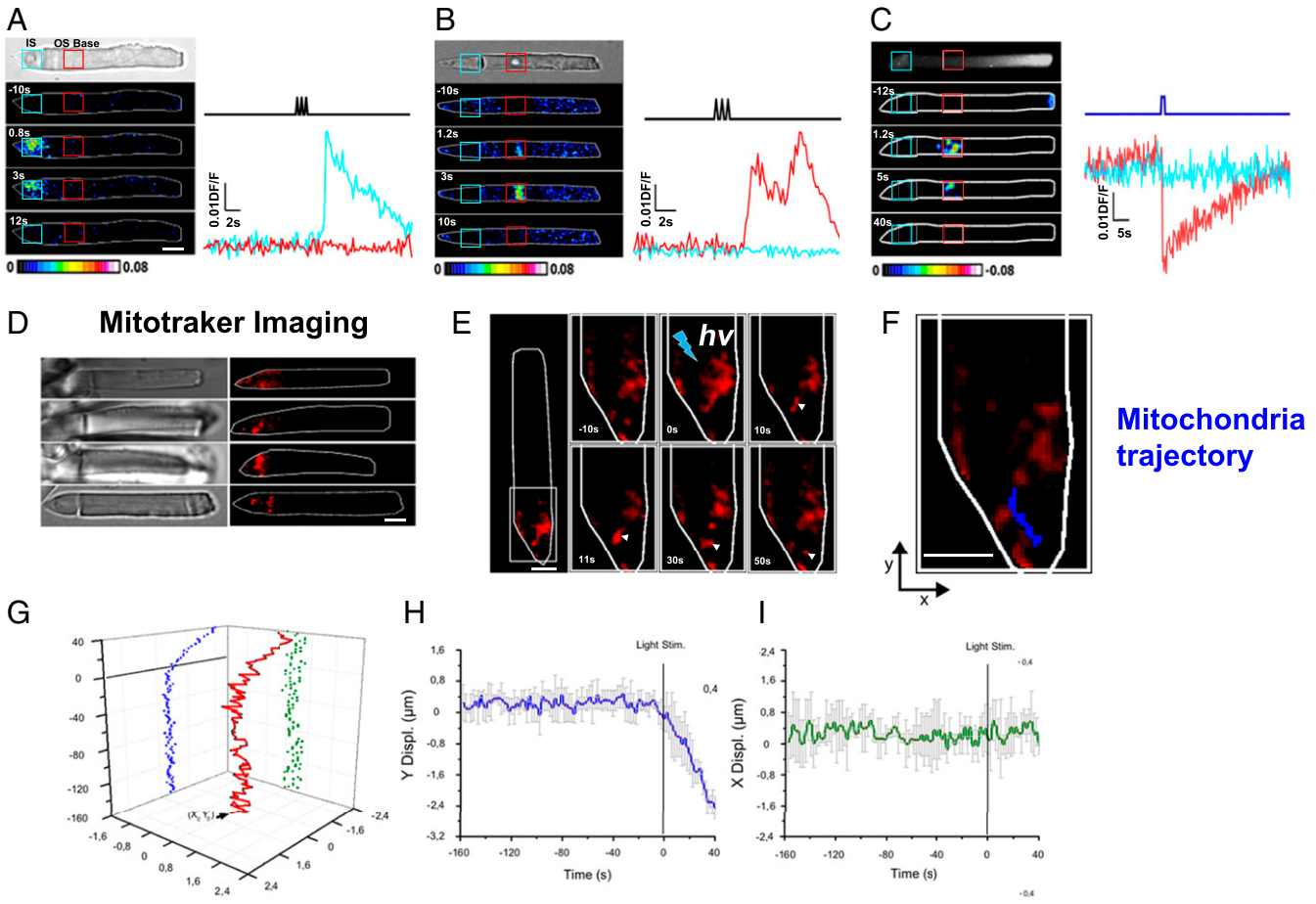

Fig. 5. Compartmentalization of calcium dynamics between IS and OS. (*A*) *DF/F* transients evoked by a mechanical stimulation of the IS. The force was ~8 pN for each mechanical pulse. Bright-field image at *Top*. Below, *DF/F* maps before, during, and after the stimulus, with respective timing. (*B*) As in *A*, but for the OS. (*C*) Localized light stimulation of the OS base with a 488-nm light pulse of 1 s, equivalent to ~2,100 R* per rod. (*D*) Map of MitoTracker labeling indicating the localization of mitochondria in four rods: bright-field images (*Left*) and the fluorescence emitted by Mitotracker (*Right*). (*E*) Images of mitochondria over ~1 min and the effect of a bright flash of diffuse light at 488 nm. (*F*) In blue, the trajectory of mitochondria following a light stimulation of 1 s and ~2100 R* per rod. (*G*) Three-dimensional plot of mitochondria trajectory (*x*, *y*, Time), horizontal bar indicates the light stimulus. (*H*) Average mitochondria displacement on the *y* axes. The vertical bar represents the light stimulus onset (blue trace is the mean, and the bars represent the SEM) ($n = 5$). (*I*) As in *H*, but for the *x* axes ($n = 5$). (Scale bars, 10 µm.)

homogeneous and that immunolabeling of these molecules is more evident at the OS base and less evident at the OS tip. Therefore, OS is not only functionally inhomogeneous but also structurally inhomogeneous, and some hints of structural non-uniformity are present in the distribution profiles of proteins and lipids obtained by combining serial sectioning of the retina with quantitative mass spectrometry (29). The spatial resolution of these profiles, however, is not adequate to establish in a conclusive way the existence of gradients of structural proteins inside the OS, and similar data with better spatial resolution are needed.

Discussion

Our work reveals and confirms that several functional (Figs. 1–5) and structural properties (Fig. 6) of the rod OS vary longitudinally: there is a sharp gradient of $[Ca^{2+}]_i$, responsiveness, the occurrence of calcium flares, and the structural components of OS (summarized in Fig. 7). Early (29) and more recent electron micrographs (30) of the rod OS show a perfect stack of discs in the OS, which have the same shape and geometrical dimensions from the base to its tip. In contrast with these pictures, however, the rod OS is not a homogeneous structure and displays both a functional and a structural gradient, where new discs are synthetized and shed (31). The present manuscript also describes a—to some extent—unexpected feature of the rod OS: the existence of spontaneous and light-induced calcium flares, i.e., highly localized increases in $[Ca^{2+}]_i$.

Calcium Flares. The observation of 488-nm light-induced flares of $[Ca^{2+}]_i$ (see Fig. 4 and see *SI Appendix*, Figs. S4 and S5) at the center and tip of the rod OSs, both in isolated rods and in intact retinal rods, is remarkable and unexpected. However, it has been previously shown that upon light stimulation, calcium can be released from the discs (19, 20). This evidence suggests that light stimuli can transiently and locally increase $[Ca^{2+}]_i$ in the OS. The calcium flares described here were observed using the fluorescent dye CaSiR-1, which works when excited at 650 nm and, therefore, not under conditions of dark adaptation. Indeed, calcium flares can also appear during imaging recordings of the fluorescence emitted by CaSiR-1, and their occurrence is random (Fig. 4 *B* and *C*). It is possible, therefore, that the observed calcium flares occur as a consequence of the activation of rhodopsin on the discs: Indeed, on some occasions, we observed that following several minutes of continuous stimulation at 650 nm, light flashes at 488 nm induced calcium flares more frequently, as shown in the recording of *SI Appendix*, Fig. S4 *A* and *B*. During electrical recordings in dark-adapted conditions, we did not

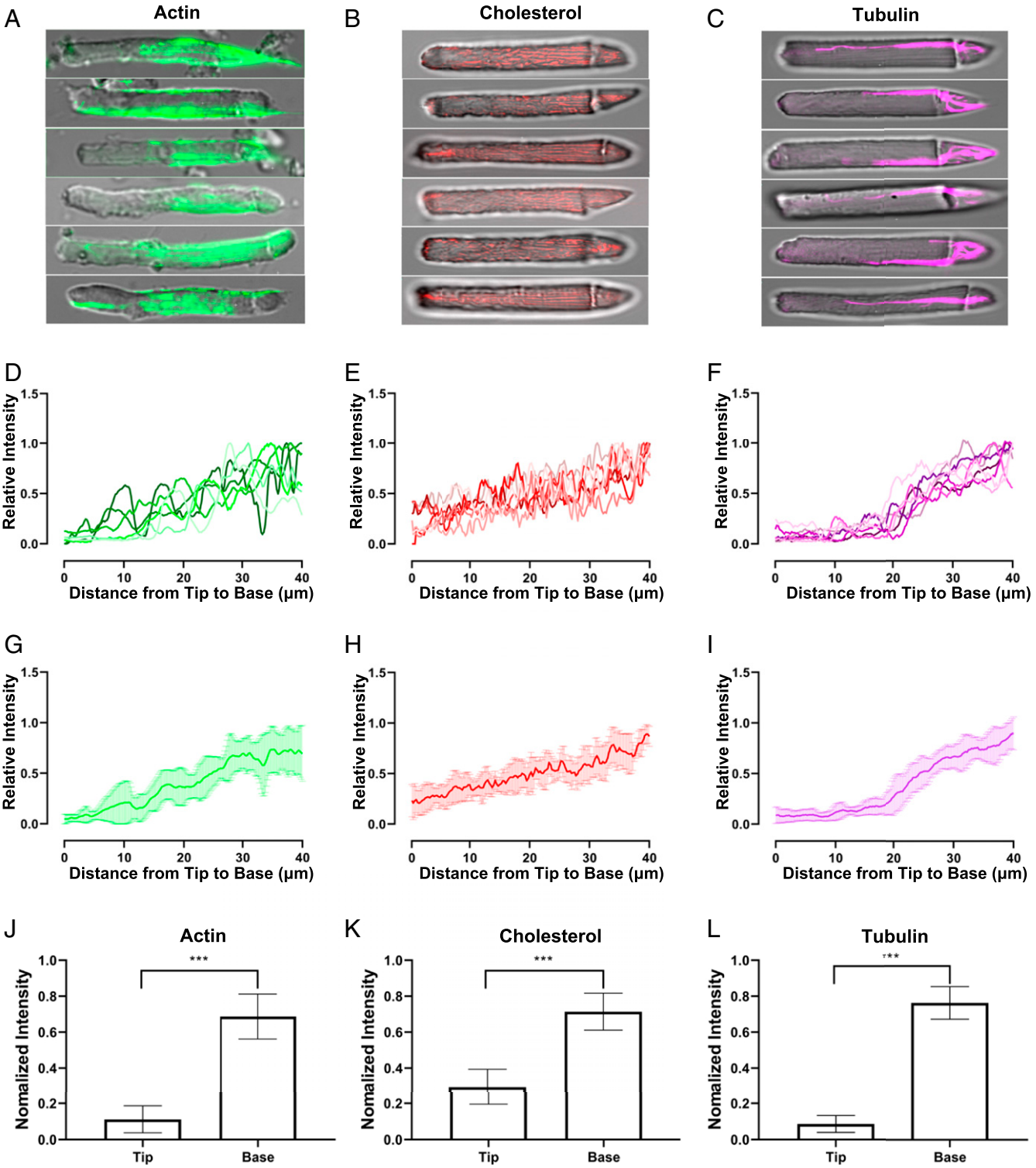

Fig. 6. Actin, tubulin, and cholesterol gradients in rods OSs. (*A*) IS+OS rods, stained with phalloidin. (*B*) As in *A*, but rods were stained with Bodipy marker. (*C*) As in *A*, but rods were stained with tubulin marker. (*D*) Normalized intensity profile obtained from the six representative IS+OS rods in *A*, from the OS base to the tip. (*E*) Same as in *D* but for the cholesterol staining in *B*. (*F*) Same as in *D* but for the tubulin staining in *C*. (*G*) Averaged intensity profile obtained from the six representative IS+OS rods in *A*. (*H*) Same as in *G* but for the cholesterol staining in *B*. (*I*) Same as in *G* but for the tubulin staining in *C*. (*J*) Quantification of the actin staining intensity profile. Base and tip average intensity were 0.687 ± 0.051 SEM and 0.112 ± 0.030 SEM, respectively ($n = 8$; *t* test $P < 0.001$). (*K*) As in *J* but for the cholesterol staining. Base and tip average intensity were 0.714 ± 0.039 SEM and 0.295 ± 0.037 SEM, respectively ($n = 9$; *t* test $P < 0.001$). (*L*) As in *J* but for the tubulin staining. Base and tip average intensity were 0.762 ± 0.034 SEM and 0.086 ± 0.018 SEM, respectively ($n = 7$; *t* test ***$P < 0.001$).

observe any event that could be attributed to the spontaneous calcium flares described in Fig. 4. We are not able to establish whether calcium flares occur in the complete absence of any light stimulation, because they are detected with a fluorescent dye—i.e., CasIR—requiring an excitation light in the near-infrared perceived by the rods.

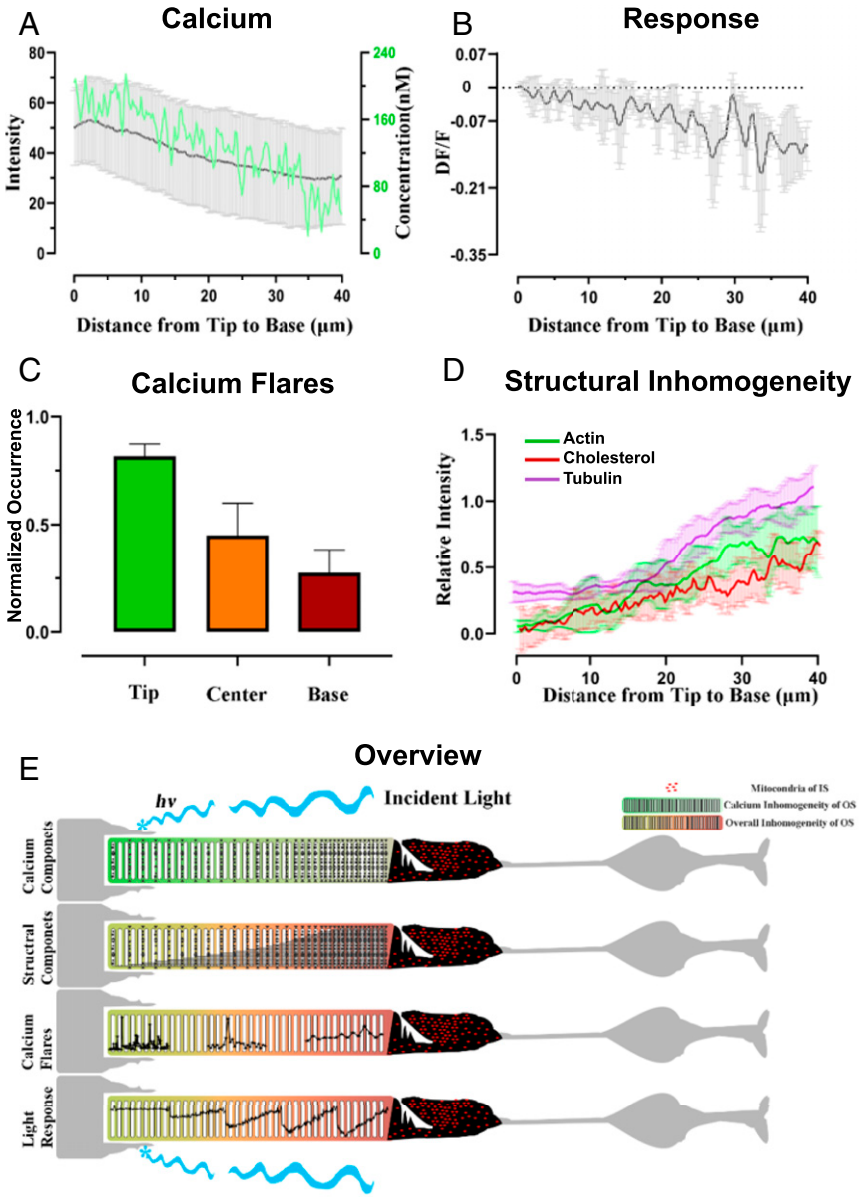

Fig. 7. Structural and functional gradients in OS. (*A*) The gradient of $[Ca^{2+}]_i$ obtained in light-adapted conditions using Fura Red (right axis and see *SI Appendix*, Fig. S3) and of the emitted CaSiR-1 fluorescence in semidark-adapted conditions (left axis) ($n = 8$). (*B*) The gradient of responsiveness ($n = 10$). (*C*) The distribution of calcium flares ($n = 60$; $mean_{base}$ 0.275 ± 0.063 SEM, $mean_{center}$ 0.450 ± 0.087 SEM, $mean_{tip}$ 0.817 ± 0.033 SEM). (*D*) The gradient of actin, tubulin, and cholesterol (see also Fig. 6). (*E*) Summary of the functional and structural gradients presents in the rod OS.

Calcium flares at the OS tip can be triggered by a flash of light at 488 nm, and in these circumstances the same flash of light induces a drop of $[Ca^{2+}]_i$ at the OS base (Fig. 4 *E* and *F*).

Our imaging experiments show that these calcium flares always appear tangentially to the OS and do occur in a restricted longitudinal portion of the OS (Fig. 4*F*). These results suggest that calcium flares colocalize with discs inside the OS, indicating that they probably originate from the discs. We rarely observed light-induced calcium flares at the OS base, which usually appeared only at the center and tip of the OS. We propose, therefore, that calcium flares are part of the disk renewal and shedding process and could signal retinal pigmented epithelium cells to trigger phagocytosis of aged and shedding discs (19, 32, 33).

Longitudinal Inhomogeneity of Rod Outer Segments and Disk Turnover. There are several previous reports indicating heterogeneity in rod OSs, reviewed by Koch and Dell'Orco (34), which has been ascribed to natural aging and renewal of OSs. Several observations indicate that the proteins involved in transduction and adaptation are assembled in complexes forming highly ordered structures that interact with the supporting disk membranes and the local cellular architecture (24, 32). Key proteins involved in phototransduction, such as rhodopsin, transducing, and phosphodiesterase, operate over the discs and are very close to the plasma membrane, where cyclic nucleotide gated channels are located. Indeed, the efficiency of the phototransduction machinery depends on the structural properties of the discs (34, 35), which are affected by the renewal and shedding processes occurring at the base and tip of OSs, respectively. Moreover, the gradient of concentration/abundancy of structural proteins along the OS (Fig. 7*D*) is likely to be the consequence of the renewal and shedding process. In this view, the presence of a functional and structural gradient along the length of

the OS (Fig. 7) is not surprising, in agreement with previous investigations based on the use of Lucifer Yellow (36) and the dye FM1-43 (20).

Calcium Compartmentalization. Previous reports (14, 37) using Ca^{2+} Green and Fura 2 in isolated OSs and in isolated IS+OSs have not detected a calcium gradient in the OS, as observed here (Fig. 1 and *SI Appendix*, Fig. S3). This discrepancy is likely caused by the use of CaSiR-1, which works in the near IR and allows us to verify whether isolated IS+OS are functional. Indeed, we were able to observe a photoresponse, i.e., a light-induced drop in intracellular calcium. We did not observe a calcium gradient in nonfunctional IS+OSs (Fig. 1). The sharp brightness difference in fluorescence observed in functional rods (Fig. 2) between the IS and the base of the OS suggests that there is no or limited fusion of the inner and outer segment membranes (38). Our ratiometric analysis of calcium concentration in the IS+OS indicates that the levels of calcium measured in the IS are 65 ± 2.63 nM, a value in the range of what was previously reported (39). Therefore, the strong fluorescence observed in IS+OS loaded with CaSiR-1 AM possibly reflects a calcium concentration at the physiological level.

A remarkable feature of calcium dynamics in rods is the relative isolation of the OS and IS (Fig. 5). Calcium changes that have initiated either in the IS or in the OS do not easily propagate through the cilium connecting the OS and the IS, which is known to provide electrical coupling (27). The strong compartmentalization of calcium dynamics between the IS and OS is likely to be caused by the high density of mitochondria present in the IS near the cilium (Fig. 5*D*), which act as a powerful buffer of $[Ca^{2+}]_i$ and, thus, as a barrier for the diffusion of intracellular calcium between the OS and IS. Calcium flares originating in the OS do not diffuse easily along the OS, as could be expected in the restricted free space inside the OSs. Indeed, the presence of the inner segment affects the localization of proteins already present in the outer segment. In support of this view (Fig. 2), intact rods from a piece of retina have a much reduced and often almost absent photoresponse at the tip. This observation indicates that proteins present in the IS and nucleus affect properties of the phototransduction cascade in the OS. Interestingly, based on a recent study conducted in zebrafish (40), it was reported that variations in calcium in the mitochondria of cone photoreceptors can influence both phototransduction and the metabolism of these neurons. Moreover, it has been shown that mitochondria strictly regulate calcium concentration inside rod photoreceptors and that an imbalance in their membrane potential leads to apoptosis (41). We have not observed calcium flares in isolated OS, and we believe that the renewal process of discs observed in intact and functional rods occurs because discs deteriorate and flares—in our view—are linked to their renewal.

In the rod OS, there is a powerful mechanism for the extrusion of Ca^{2+} consisting of Na^+: Ca^{2+}, K^+ (NCKX1), which has been characterized in great detail (15). It has been shown that rods in which the gene encoding NCKX1 has been knocked out are functional to some extent (42). This observation suggests the existence of additional molecular mechanisms able to extrude calcium from the interior of the OS. A high density of these molecular mechanisms in the OS can be a barrier impeding the longitudinal diffusion of intracellular calcium. The extrusion of Ca^{2+} from the rod OS is mediated by the Na^+: Ca^{2+}, K^+ exchanger (43). In darkness, the extrusion of one Ca^{2+} and one K^+ requires the entry of four Na^+ ions (44). Na^+ ions entering the OS through the light-sensitive channels are extruded by the Na^+/K^+-ATPase located in the IS (15); therefore, the concentration of intracellular Na^+ is higher at the tip than at the base, where there is a sink for Na^+. There are no known Na^+ buffers, and the Na^+ diffusion coefficient is ∼1,900 $\mu m^2 \cdot sec^{-1}$, which is much larger than that of cGMP. We expect Na^+ to diffuse freely within most of the OS, and we do not expect a large Na^+ gradient for most of the OS length. However, given the steep dependence of the activity of the Na^+: Ca^{2+}, K^+ exchanger on the Na^+ concentration, even a shallow Na^+ gradient within the OS could be responsible for the calcium gradient we observed within the OS. This shallow Na^+ gradient is expected to have only a small effect on the amplitude of the photoresponse, which depends linearly on the Na^+ gradient.

Given the functional and structural gradient of the phototransduction machinery (Fig. 7), in order to maximize the detection of photons, it is convenient that photons arriving from the external world impinge first on the OS base. Indeed, this could be one of the reasons for the geometrical arrangement of the retina inside the eye in which photons travel through the entire retina before reaching the rods: In this way, the first encountered rhodopsin molecules are those located at the OS base that efficiently initiate phototransduction.

Methods

Immunofluorescence. Single-rod staining was obtained by fixing the retina in paraformaldehyde solution at 4% for 60 min at 22–25 °C. The tissue was then permeabilized with a solution of phosphate-buffered saline (PBS) with 0.1% Triton X-100. A PBS solution with bovine serum albumin at 1% was used to block not-specific binding sites. Then, the retina was washed with cold PBS three times for 5 min each. The incubation of the retina with Phalloidin (Life Technologies, A12379, Ringer solution 1:4,000) at room temperature for 1 h allowed the visualization of the actin in the tissue. Single rods were then obtained by mechanical dissociation and examined with a confocal microscope (NIKON A1R) equipped with 488-nm and 640-nm excitation lasers, 40× objective (N.A. 0.75) and 60× oil immersion objective (N.A. 1.40).

Isolation of Photoreceptors and Electrical Recordings. The experiments described in this paper followed the guidelines of the International School for Advanced Studies ethics committee and the Italian and European procedures for animal care (d.l. 116/92; 86/609/C.E.). Male and female frogs of the species *X. laevis* were dark adapted overnight, anesthetized with tricaine, and euthanized under dim red light. Their eyes were dissected as previously reported (45). Single rods consisting of an IS+OS were obtained by gentle mechanical dissociation of a small piece of retina, cut from the whole with surgical scissors. The integrity of the isolated retinal rods was maintained immersing them in Ringer solution containing (in mM): 110 NaCl, 2.5 KCl, 1 $CaCl_2$, 1.6 $MgCl_2$, and 3 Hepes-NaOH, 0.01 EDTA, and 10 glucose (pH 7.7–7.8 buffered with NaOH). The experiments were performed at 22–25 °C, and the salts and chemicals were purchased from Sigma-Aldrich.

The recording of rod photoreceptors light response (*SI Appendix*, Fig. S2) were obtained as previously described (45). The Axopatch 200A (Molecular Devices, LLC) was used in voltage clamp mode to record the sensory neurons currents, which were digitized at 10 kHz and low-pass filtered at 20 Hz. The filtering and the correction of the baseline was done with Clampfit 10.3 (Molecular Devices). To activate phototransduction, brief (10-ms) blue laser light pulses at 491-nm wavelength (Rapp OptoElectronic) emerged from a 10× objective of an inverted microscope (Olympus IX71; Olympus Corporation). The resulting circular spot of ∼60 μm in diameter was used to stimulate uniformly the rods. Two cameras (Hamamatsu ORCA-Flash 4.0, Hamamatsu Corporation; and Jenoptic ProgRes MF, JENOPTIK I Optical Systems, Goeschwitzer) were used to visualized the cells to avoid changing the objectives (11).

Calcium Imaging and Other Fluorescence Imaging. Retinas were immersed in the Ringer solution described in the previous section and loaded with a final concentration of 5 μM of the cell-permeable calcium dye CaSiR-1 AM (previously Goryo chemicals; currently it is the BioTracker 664 NIR Ca^{2+} Dye, Millipore Sigma) at room temperature (22–25 °C) for 45 min. After incubation, the retinas were washed three times, for 5 min each time, allowing the intracellular deesterification of the dye. Small pieces of retinas were mechanically dissociated as described above and the isolated rods were transferred into a light sealed chamber. The chamber was then placed on the stage of an Olympus IX-81 inverted microscope equipped with a light-emitting diode (LED) illumination system (X-Cite XLED1 from Excelitas Technologies), which was used for both calcium imaging (650-nm light) and light stimulations (488 nm). The experiments were performed at room temperature (between 22 and 25 °C), and the images were acquired using Micromanager software with an Apo-Fluor 60×/1.4 N.A. objective, at a sampling rate of 5 Hz for 3–10 min.

Mitotracker imaging (Life Technologies, M7512) was performed on very fresh retinas, which were immersed in Ringer solution and loaded with a final concentration of the dye of 100 nM, at 22–25 °C for 45 min in darkness. Then, they were mechanically dissociated, and the fluorescence was imaged using

560-nm LED excitation, on an Olympus IX-81 inverted microscope system. For tubulin tracker imaging (Life Technologies, T34077), we used the same incubation protocol as for the mitotracker imaging, but the final concentration of the dye was 200 nM and the incubation period lasted 1 h at 22–25 °C. The fluorescent imaging was done with a confocal microscope (NIKON A1R) and a laser at 640-nm excitation light. The objective used to visualize the cells were the 40× objective (N.A. 0.75) and 60× oil immersion objective (N.A. 1.40) mentioned previously. Cholesterol imaging was performed using the Bodipy dye (Life Technologies, C12680). Retinas were loaded as described above, but with a final dye concentration of 100 nM, and incubated in darkness for over 3 h or overnight at 4 °C. The imaging was performed with the same Nikon confocal microscope, but with an excitation laser at 514-nm wavelength. For Fura Red (Life Technologies, F3020) ratiometric calcium imaging, the dye was used at a final concentration of 5 μM in Ringer solution, and retinas were incubated for 1 h in darkness at 22–25 °C. The 488-nm LED excitation was chosen for general fluorescent imaging, and 440 nm/480 nm was used for the ratiometric experiments. For the localized light stimulations, the Nikon confocal microscope was set under the acquisition controls of A1plus stimulation. Excitation laser was set at low intensity as the stimulation light. Under non-diffused 488-nm light stimulation, the regions of interest were drawn as needed on the desired rods for local stimulations of light and then added into the serial acquisition phases. The frame time was set as less than 150 ms.

Mechanical Stimulation Using the Oscillatory Optical Trap. The mechanical stimulation of the photoreceptors was performed as previously described (46). Briefly, a polystyrene bead of 3.5 μm in diameter (G. Kisker GbR) was manipulated with an oscillatory optical trap, obtained using a Focused Tunable Lens (FTL) (EL-10-30-NIR-LD, Optotune AG). The bead was moved above the rods and sealed to the membrane. Rods stimulation was achieved precisely by tuning the FTL to change the vertical position of a bead trapped with the infrared laser. A sinusoidal pulse was sent from the computer to the FTL controller, which resulted in the oscillation of the lens and the change of the focal plane of the trapped bead. This technique allowed a confined indentation of the rods' membrane. A complete description of the method and of all of the components used can be found in the citations (46).

Data and Statistical Analysis. The *DF/F* of calcium imaging experiments was quantified using a custom Matlab code (MathWorks, Inc.) and ImageJ software v1.6 (NIH). All of the results here described are presented as mean ± SEM. The Student's *t* test (GraphPad Prism 7, GraphPad software) was used to quantify the statistical significance of the results.

Data Availability. All study data are included in the article and supporting information. All of the data used to plot panels are available in Dataset S1.

ACKNOWLEDGMENTS. We thank Daniele Dell Orco, Hugh Robinson, and Vadim Arshavsky for their useful and critical reading of the manuscript. This work was supported by funds from Regione Friuli-Venezia Giulia (Italy) for the project "GLIOBLASTOMA–Infiltrazione nei gliomi: nuovo target terapeutico"; 3315 Innovative Teams Program of Ningbo–China, Zhejiang Provincial Natural Science Foundation of China Grant LQ17C100001; and Natural Science Foundation of Ningbo City Grant 2017A610256.

1. P. A. Liebman, H. L. Weiner, R. E. Drzymala, Lateral diffusion of visual pigment in rod disk membranes. *Methods Enzymol.* **81**, 660–668 (1982).
2. I. Nir, M. O. Hall, The ultrastructure of lipid-depleted rod photoreceptor membranes. *J. Cell Biol.* **63**, 587–598 (1974).
3. J. C. Gilliam *et al*., Three-dimensional architecture of the rod sensory cilium and its disruption in retinal neurodegeneration. *Cell* **151**, 1029–1041 (2012).
4. W. J. Spencer *et al*., Photoreceptor disc membranes are formed through an Arp2/3-dependent lamellipodium-like mechanism. *Proc. Natl. Acad. Sci. U.S.A.* **116**, 27043–27052 (2019).
5. O. P. Kocaoglu *et al*., Photoreceptor disc shedding in the living human eye. *Biomed. Opt. Express* **7**, 4554–4568 (2016).
6. K. Boesze-Battaglia, T. Hennessey, A. D. Albert, Cholesterol heterogeneity in bovine rod outer segment disk membranes. *J. Biol. Chem.* **264**, 8151–8155 (1989).
7. K. Boesze-Battaglia, A. D. Albert, Cholesterol modulation of photoreceptor function in bovine retinal rod outer segments. *J. Biol. Chem.* **265**, 20727–20730 (1990).
8. K. Boesze-Battaglia, S. J. Fliesler, A. D. Albert, Relationship of cholesterol content to spatial distribution and age of disc membranes in retinal rod outer segments. *J. Biol. Chem.* **265**, 18867–18870 (1990).
9. J. L. Schnapf, Dependence of the single photon response on longitudinal position of absorption in toad rod outer segments. *J. Physiol.* **343**, 147–159 (1983).
10. T. D. Lamb, P. A. McNaughton, K.-W. Yau, Spatial spread of activation and background desensitization in toad rod outer segments. *J. Physiol.* **319**, 463–496 (1981).
11. M. Mazzolini *et al*., The phototransduction machinery in the rod outer segment has a strong efficacy gradient. *Proc. Natl. Acad. Sci. U.S.A.* **112**, E2715–E2724 (2015).
12. D. A. Baylor, T. D. Lamb, Local effects of bleaching in retinal rods of the toad. *J. Physiol.* **328**, 49–71 (1982).
13. K. J. Miyagishima, M. C. Cornwall, A. P. Sampath, Metabolic constraints on the recovery of sensitivity after visual pigment bleaching in retinal rods. *J. Gen. Physiol.* **134**, 165–175 (2009).
14. M. Gray-Keller, W. Denk, B. Shraiman, P. B. Detwiler, Longitudinal spread of second messenger signals in isolated rod outer segments of lizards. *J. Physiol.* **519**, 679–692 (1999).
15. L. Lagnado, L. Cervetto, P. A. McNaughton, Calcium homeostasis in the outer segments of retinal rods from the tiger salamander. *J. Physiol.* **455**, 111–142 (1992).
16. S. Forti, A. Menini, G. Rispoli, V. Torre, Kinetics of phototransduction in retinal rods of the newt Triturus cristatus. *J. Physiol.* **419**, 265–295 (1989).
17. A. P. Sampath, H. R. Matthews, M. C. Cornwall, G. L. Fain, Bleached pigment produces a maintained decrease in outer segment Ca2+ in salamander rods. *J. Gen. Physiol.* **111**, 53–64 (1998).
18. A. Majumder *et al*., Exchange of cone for rod phosphodiesterase 6 catalytic subunits in rod photoreceptors mimics in part features of light adaptation. *J. Neurosci.* **35**, 9225–9235 (2015).
19. G. L. Fain, W. H. Schröder, Light-induced calcium release and re-uptake in toad rods. *J. Neurosci.* **10**, 2238–2249 (1990).
20. C. Chen, Y. Jiang, Y. Koutalos, Dynamic behavior of rod photoreceptor disks. *Biophys. J.* **83**, 1403–1412 (2002).
21. T. Egawa *et al*., Development of a far-red to near-infrared fluorescence probe for calcium ion and its application to multicolor neuronal imaging. *J. Am. Chem. Soc.* **133**, 14157–14159 (2011).
22. M. Oheim *et al*., New red-fluorescent calcium indicators for optogenetics, photoactivation and multi-color imaging. *Biochim. Biophys. Acta* **1843**, 2284–2306 (2014).
23. U. Bocchero *et al*., Mechanosensitivity is an essential component of phototransduction in vertebrate rods. *PLoS Biol.* **18**, e3000750 (2020).
24. G. M. Ratto, R. Payne, W. G. Owen, R. Y. Tsien, The concentration of cytosolic free calcium in vertebrate rod outer segments measured with fura-2. *J. Neurosci.* **8**, 3240–3246 (1988).
25. T. D. Lamb, E. N. Pugh, Phototransduction in vertebrate rods and cones: Molecular mechanisms of amplification, recovery and light adaptation. *Handb. Biol. Phys.* **3**, 183–255 (2000).
26. T. Burgoyne *et al*., Rod disc renewal occurs by evagination of the ciliary plasma membrane that makes cadherin-based contacts with the inner segment. *Proc. Natl. Acad. Sci. U.S.A.* **112**, 15922–15927 (2015).
27. H. Khanna, Photoreceptor sensory cilium: Traversing the ciliary gate. *Cells* **4**, 674–686 (2015).
28. M. M. Giarmarco, W. M. Cleghorn, S. R. Sloat, J. B. Hurley, S. E. Brockerhoff, Mitochondria maintain distinct Ca2+ pools in cone photoreceptors. *J. Neurosci.* **37**, 2061–2072 (2017).
29. F. S. Sjöstrand, The ultrastructure of the outer segments of rods and cones of the eye as revealed by the electron microscope. *J. Cell. Comp. Physiol.* **42**, 15–44 (1953).
30. S. Nickell, P. S. H. Park, W. Baumeister, K. Palczewski, Three-dimensional architecture of murine rod outer segments determined by cryoelectron tomography. *J. Cell Biol.* **177**, 917–925 (2007).
31. M. M. LaVail, Rod outer segment disk shedding in rat retina: Relationship to cyclic lighting. *Science* **194**, 1071–1074 (1976).
32. P. Nunes, N. Demaurex, The role of calcium signaling in phagocytosis. *J. Leukoc. Biol.* **88**, 57–68 (2010).
33. S. Zumerle *et al*., Intercellular calcium signaling induced by ATP potentiates macrophage phagocytosis. *Cell Rep.* **27**, 1–10.e4 (2019).
34. K.-W. Koch, D. Dell'Orco, Protein and signaling networks in vertebrate photoreceptor cells. *Front. Mol. Neurosci.* **8**, 67 (2015).
35. T. G. Wensel, Signal transducing membrane complexes of photoreceptor outer segments. *Vision Res.* **48**, 2052–2061 (2008).
36. B. Matsumoto, J. C. Besharse, Light and temperature modulated staining of the rod outer segment distal tips with Lucifer yellow. *Invest. Ophthalmol. Vis. Sci.* **26**, 628–635 (1985).
37. D. Krizaj, D. R. Copenhagen, Compartmentalization of calcium extrusion mechanisms in the outer and inner segments of photoreceptors. *Neuron* **21**, 249–256 (1998).
38. E. Townes-Anderson, Intersegmental fusion in vertebrate rod photoreceptors. Rod cell structure revisited. *Invest. Ophthalmol. Vis. Sci.* **36**, 1918–1933 (1995).
39. T. Szikra, D. Krizaj, The dynamic range and domain-specific signals of intracellular calcium in photoreceptors. *Neuroscience* **141**, 143–155 (2006).
40. R. A. Hutto *et al*., Increasing Ca^{2+} in photoreceptor mitochondria alters metabolites, accelerates photoresponse recovery, and reveals adaptations to mitochondrial stress. *Cell Death Differ.* **27**, 1067–1085 (2020).
41. L. He, A. T. Poblenz, C. J. Medrano, D. A. Fox, Lead and calcium produce rod photoreceptor cell apoptosis by opening the mitochondrial permeability transition pore. *J. Biol. Chem.* **275**, 12175–12184 (2000).
42. F. Vinberg, J. Chen, V. J. Kefalov, Regulation of calcium homeostasis in the outer segments of rod and cone photoreceptors. *Prog. Retin. Eye Res.* **67**, 87–101 (2018).
43. L. Cervetto, L. Lagnado, R. J. Perry, D. W. Robinson, P. A. McNaughton, Extrusion of calcium from rod outer segments is driven by both sodium and potassium gradients. *Nature* **337**, 740–743 (1989).
44. L. Lagnado, L. Cervetto, P. A. McNaughton, Ion transport by the Na-Ca exchange in isolated rod outer segments. *Proc. Natl. Acad. Sci. U.S.A.* **85**, 4548–4552 (1988).
45. U. Bocchero, B. M. Tam, C. N. Chiu, V. Torre, O. L. Moritz, Electrophysiological changes during early steps of retinitis pigmentosa. *Invest. Ophthalmol. Vis. Sci.* **60**, 933–943 (2019).
46. F. Falleroni, V. Torre, D. Cojoc, Cell mechanotransduction with piconewton forces applied by optical tweezers. *Front. Cell. Neurosci.* **12**, 1–11 (2018).

Mechanosensitivity for phototransduction in vertebrate rods

(MS Published in *Plos Biology*)

PLOS BIOLOGY

RESEARCH ARTICLE

Mechanosensitivity is an essential component of phototransduction in vertebrate rods

Ulisse Bocchero[1☯¤], Fabio Falleroni[1☯], Simone Mortal[1☯], Yunzhen Li[1], Dan Cojoc[2], Trevor Lamb[3], Vincent Torre[1,4,5]*

1 Neurobiology Department, International School for Advanced Studies, Trieste, Italy, **2** Institute of Materials, National Research Council of Italy (CNR), Trieste, Italy, **3** Eccles Institute of Neuroscience, John Curtin School of Medical Research, The Australian National University, Canberra, Australia, **4** Cixi Institute of Biomedical Engineering, Ningbo Institute of Materials Technology and Engineering, Chinese Academy of Sciences, Zhejiang, China, **5** Center of Systems Medicine, Chinese Academy of Medical Sciences, Suzhou Institute of Systems Medicine, Suzhou Industrial Park, Suzhou, China

☯ These authors contributed equally to this work.
¤ Current address: Photoreceptor Physiology Group, NEI, NIH, Bethesda, Maryland, United States of America
* torre@sissa.it

OPEN ACCESS

Citation: Bocchero U, Falleroni F, Mortal S, Li Y, Cojoc D, Lamb T, et al. (2020) Mechanosensitivity is an essential component of phototransduction in vertebrate rods. PLoS Biol 18(7): e3000750. https://doi.org/10.1371/journal.pbio.3000750

Academic Editor: Samer Hattar, National Institutes of Health, UNITED STATES

Received: January 31, 2020

Accepted: June 26, 2020

Published: July 15, 2020

Peer Review History: PLOS recognizes the benefits of transparency in the peer review process; therefore, we enable the publication of all of the content of peer review and author responses alongside final, published articles. The editorial history of this article is available here: https://doi.org/10.1371/journal.pbio.3000750

Data Availability Statement: All relevant data are within the paper and its Supporting Information files.

Funding: The entire study was funded by the International School for Advanced Studies. VT

Abstract

Photoreceptors are specialized cells devoted to the transduction of the incoming visual signals. Rods are able also to shed from their tip old disks and to synthesize at the base of the outer segment (OS) new disks. By combining electrophysiology, optical tweezers (OTs), and biochemistry, we investigate mechanosensitivity in the rods of *Xenopus laevis*, and we show that 1) mechanosensitive channels (MSCs), transient receptor potential canonical 1 (TRPC1), and Piezo1 are present in rod inner segments (ISs); 2) mechanical stimulation—of the order of 10 pN—applied briefly to either the OS or IS evokes calcium transients; 3) inhibition of MSCs decreases the duration of photoresponses to bright flashes; 4) bright flashes of light induce a rapid shortening of the OS; and 5) the genes encoding the TRPC family have an ancient association with the genes encoding families of protein involved in phototransduction. These results suggest that MSCs play an integral role in rods' phototransduction.

Introduction

Photoreceptors are thought to be specialized cells devoted to the transduction of the incoming visual signals. Following strong illumination, rod outer segments (OSs) from mice [1] and fly photoreceptors [2,3] have been reported to increase their length and contract respectively, but rod OSs from frogs shrink their length by about 0.4–0.6 μm [4]. In addition, rod photoreceptors are known to shed old disks from their tip and to synthesize new disks at the base of the OS. These observations indicate the existence of mechanical machinery within rod OSs, but its action and role in phototransduction are completely unknown.

Mechanosensitive channels (MSCs) [5] have been found in olfactory sensory neurons [6] and possibly are expressed in many—if not all—neurons of the central nervous system. In

received the funding. The funders had no role in study design, data collection and analysis, decision to publish, or preparation of the manuscript.

Competing interests: The authors have declared that no competing interests exist.

Abbreviations: AM-ester, acetoxymethyl ester; BSA, Bovine Serum Albumin; CaSiR-1, Calcium ion detecting probe based on silicon rhodamine; CNGB, Cyclic Nucleotide-Gated ion channel Beta; CNR, National Research Council of Italy; FTL, Focused Tunable Lens; GC, guanylyl cyclase; GRK, G-protein receptor kinase; GsMTx-4, M-theraphotoxin-Gr1a; IR, infrared; IS, inner segment; Mb, megabase; MSC, mechanosensitive channel; Mya, million years ago; OOT, oscillatory optical trap; OS, outer segment; OTs, optical tweezers; QPD, quadrant photodetector; TRP, transient receptor potential; TRPC, transient receptor potential canonical; Tsat, saturation time; WB, western blot; 2R WGD, 2 rounds of whole-genome duplication.

bacteria, MSCs are thought to play a major role in maintaining osmotic equilibrium across their membrane especially upon hypoosmotic conditions; in these conditions, the opening of poorly selective MSCs contributes to the control of osmotic equilibrium [7–9]. MSCs in eukaryotic cells can be activated by light mechanical forces in the 10-pN range [10].

There are now several classes of ion channels implicated in the eukaryotic mechanotransduction machinery, including Piezo 1 and 2 channels [11] and transient receptor potential channels, referred as TRP channels. TRP channels form a superfamily of cation-selective ion channels located in cell membranes that are involved in various sensory modalities such as chemoreception, thermoreception, mechanoreception, and photoreception. TRP channels were discovered more than 3 decades ago in photoreceptors of fruit flies (*Drosophila*) [12–15]. The TRP superfamily in animals contains at least 7 families, comprising around 30 subfamilies, and the majority of these isoforms are expressed in vertebrates. Vertebrate TRPC channels (C for canonical) are so named because they are most closely related to the canonical TRP channels involved in *Drosophila* phototransduction. There are 7 subfamilies of vertebrate TRPCs, of which TRPC1, 4, and 5 are very closely related, as will be considered subsequently [14].

TRP channels are nonselective permeable cationic channels with a selectivity ratio Ca^{2+}/Na^{+} that varies between the different family members [16]. Within the TRPC family, TRPC1 and TRPC6 have been reported to be activated directly by membrane stretch and curvature [17].

By combining electrical recordings, optical tweezers (OTs), and biochemical tools, we demonstrate in the present manuscript that 1) weak mechanical stimulation—of the order of 10 pN—applied briefly to either the OS or inner segment (IS) evokes a clear calcium transient; 2) inhibition of MSCs decreases the duration of photoresponses to bright flashes, and the magnitude of this effect increases with flash intensity; 3) bright flashes of light induce a rapid shortening—of the order of 200–300 nm—of the rod OS; and 4) the genes encoding the TRPC family of MSCs appear to have an ancient association with the genes encoding 3 families of protein that are directly involved in phototransduction in the rod OS. We also show that the MSCs TRPC1 and Piezo1 are present abundantly in rod ISs. Our analysis, together with 2 proteomic studies investigating the protein composition of the disks [18] and of the OSs [19], does not support their expression in OSs.

Results

To investigate mechanosensitivity in rod photoreceptors, we decided to use OTs [20], which were used previously in our laboratory to trigger calcium transients in response to very weak forces in the 10-pN range [10]. Application of this approach requires the rods to be held in an environment of high mechanical stability, for example, lying on a rigid substrate. This makes it extremely difficult to simultaneously record their electrical responses, using either suction or patch pipettes. Instead, we chose to measure the functionality of rods through an infrared (IR) calcium dye, a Calcium ion detecting probe based on silicon rhodamine (CaSiR-1) [21]. Specifically, we loaded retinas using the acetoxymethyl ester (AM-ester) of this dye (see Methods), and then we mechanically dissociated individual rod photoreceptors and/or OSs. We viewed the preparation using IR illumination at 750 nm and an IR-sensitive video camera attached to the microscope. Then, from regions of interest, we recorded the fluorescence emitted by CaSiR-1 upon excitation with a 650-nm light (Fig 1A). This established that OSs lacking an IS fluoresced intensely (Fig 1A, left inset) and showed further that this fluorescence was not reduced by illumination with blue light. Thus, isolated OSs were unresponsive to blue light.

More nearly intact rods, in which the OS remained connected to at least part of its IS (i.e., OS + IS), fell into 2 categories. On the one hand, we found 1 category of "unresponsive" cells

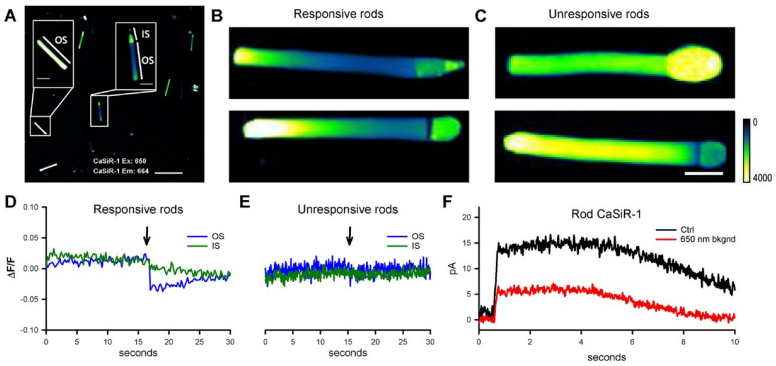

Fig 1. Fluorescence emitted by the calcium-sensitive indicator, CaSiR-1, incorporated into rods isolated from the *Xenopus laevis* retina. (A) Isolated rods in a dish, stained with CaSiR-1 excitation: 650 nm and emission: 664, showing a mixture of rods comprising both isolated OSs (left) and IS + OS (right) (scale bar, 50 μm). (B) Intact rods comprising an IS + OS typically display a pronounced longitudinal gradient of fluorescence, with the base of the OS quite dim. These 2 rods were responsive to blue light, as typified by panel D. The color scale from 0 to 4,000 is a linear scale. (C) Some ISs + OSs exhibited fairly uniform high fluorescence along the OS and were unresponsive to blue light (491 nm), as typified by panel E (scale bar is 10 μm for all the images). (D) Photoresponses from an IS + OS of the kind shown in panel B, from a ROI corresponding to 100 × 300 pixels of the OS (blue trace) and from an ROI corresponding to the IS (green trace). (E) No photoresponse was seen from the OS of ISs + OSs of the kind shown in panel C. (F) Suction pipette recordings in response to stimulation by bright blue flashes (approximately 2,500 photoisomerization [R^*]) from an IS + OS loaded with CaSiR-1, in the absence (black trace) and in the presence (red trace) of the intensity of 650-nm light used for calcium imaging in the other panels. CaSiR-1, Calcium ion detecting probe based on silicon rhodamine; IS, inner segment; OS, outer segment; ROI, region of interest.

https://doi.org/10.1371/journal.pbio.3000750.g001

that showed no change in fluorescence upon exposure to blue light (Fig 1E). These cells were characterized by approximately uniform fluorescence along the OS, at a moderate to high level, and often showed a high level of fluorescence in the IS (Fig 1E, n>80). A second category of cells exhibited a marked gradient of fluorescence along the OS, with the basal section fluorescing only weakly (Fig 1A, right inset, and Fig 1B; $n > 50$). The emitted fluorescence of the CaSiR dye at the OS tip of IS + OS was usually 4 times larger than at its base so that the base appeared darker than the tip. Such cells exhibited a distinct drop in OS fluorescence in response to blue light (Fig 1D, blue trace; $n = 10$; see also S1 Fig). We hypothesize that this second category represents functional rods that exhibited a light-induced decrease in OS free intracellular calcium concentration as a result of the combination of activation of the phototransduction cascade and the existence of a circulating "dark current" driven by the ion gradients maintained by IS metabolism [22]. The longitudinal gradient in OS calcium concentration is likely to arise from the combination of 2 mechanisms: 1) the gradient of Na^+–Ca^{2+}–K^+ exchanger activity along the OS and 2) the gradient in Na^+ ion concentration caused by longitudinal diffusion of Na^+ ions towards the "sink" for intracellular Na^+ provided by Na-K-ATPase activity in the IS [23]. For the unresponsive cells (and for isolated OSs), it is plausible that there is a physical disconnect between the IS and OS that disrupts the maintenance of the required low Na^+ ion concentration in the OS.

For our experiments using OTs, we conclude from the results above that we can identify the functionality of rods lying on a rigid substrate: the cells need to have been preloaded with CaSiR-1, and then their emitted fluorescence is viewed upon excitation with 650-nm light. Functional rods display a pronounced longitudinal gradient of emitted fluorescence, with the basal end appearing dark.

In separate electrophysiological experiments we measured the effect of the 650-nm excitation light on the circulating current of functioning rods measured by presentation of a bright flash (Fig 1F). Compared with dark-adapted conditions (black trace), the circulating current in

the presence of the 650 nm excitation light (red trace) was reduced to about 40% (response amplitude 14 ± 2.5 pA in darkness and around 5.5 ± 2 pA with excitation; $n = 7$). From comparison with the effect of blue light, we conclude that the 650-nm light used to excite CaSiR-1 was approximately equivalent to about 500 R*/rod/s. Therefore, our measurements of changes in calcium concentration elicited by mechanical stimulation were performed during the equivalent of dim to moderate illumination of the rod, and we refer to this as "semi-dark-adapted" conditions.

Mechanosensitivity of rods

Using the criteria developed above, we identified responsive isolated rods that had been loaded with the calcium-sensitive dye CaSiR-1, and we applied mechanical stimuli of approximately 10 pN to either the OS or the IS by means of an oscillatory optical trap (see S2 Fig and [10]). In semi-dark–adapted conditions, a mechanical pulse applied to a silica bead contacting the IS (Fig 2A) evoked a local increase in fluorescence (Fig 2B), with a magnitude Delta Fluorescence over the resting Fluorescence (DF/F) that could reach around 0.2 in 10–20 s (Fig 2C). The increase in fluorescence began with little delay from the mechanical stimulus (270 ms ± 80, $n = 12$), and the fluorescence signal remained localized to the IS, with no propagation to the OS (Fig 2B). Comparable results were obtained when the stimulating bead was touching the OS (Fig 2E): upon mechanical stimulation, the fluorescence increased locally (Fig 2F), reaching peak in about 10 s (Fig 2G), after a delay of no more than approximately 300 ms (Fig 2H). Collected results from 8 experiments on the IS and 8 experiments on the OS indicate a peak

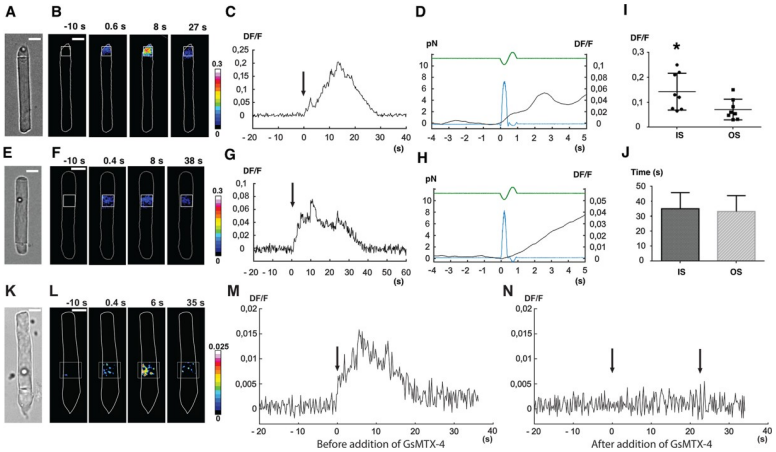

Fig 2. Calcium response of *X. laevis* rods (OS + IS) to weak mechanical stimulation applied in the vertical direction (i.e., orthogonal to the plane of the images in A, E, K). (A) A trapped bead in contact with the tip of the rod IS, under bright-field IR imaging. (B) Fluorescence change (DF/F) images, showing the ROI used to quantify the fluorescence change versus time. (C) Time course of the evoked DF/F change from the ROI in B. Mechanical stimulation was applied at time 0, as indicated by the arrow. (D) Trace from panel C on an expanded time base, additionally showing the FTL driving command (green trace) used to move the trapped bead, and the resulting force pulse (blue trace); the force applied to the IS was about 8 pN. (E, F, G, and H) As in A, B, C, and D but for mechanical stimulation of the rod OS. (I) Collected results for peak DF/F (mean ± SD) induced by mechanical stimulation for IS and OS, respectively (S1 Data). (J) Mean duration of calcium transients for IS and OS, respectively (S2 Data). Significance was determined with a two-tailed Student *t* test with $p < 0.05$. A calcium transient was detected when DF/F was above 0.004, approximately equivalent to 5-fold the background noise. Termination of detected transients was taken to occur when DF/F decreased below 0.004. (J, K, L, M, and N) As in E, F, and G but for mechanical stimulation before (M) and after (N) an exposure to GsMTx-4. In panels B, F, and L of Fig 2, the color maps indicate DF/F after spatial averaging over a window of 3 × 3 pixels. In subsequent panels (C, D, G, H, and M, N), DF/F was computed over the region indicated by the white boxes in panels B, F, and L. FTL, Focus Tunable Lens; GsMTx-4, M-theraphotoxin-Gr1a; IR, infrared; IS, inner segment; OS, outer segment; ROI, region of interest.

https://doi.org/10.1371/journal.pbio.3000750.g002

fluorescence increase (DF/F) of 0.14 ± 0.07 and 0.07 ± 0.04, respectively (Fig 2I and statistically different with $p < 0.05$), whereas the mean duration of these transients was around 35.1 s ± 10.7 in the IS and 33.2 s ± 10.6 in the OS (Fig 2L). The increase of intracellular calcium could have come across the plasma membrane or from internal stores or from both. In the case of the OS, "internal stores" encompasses possible fluxes from within the disks.

In several experiments, we repeated the same mechanical stimulation at least 3 times, and we observed a decline in the magnitude of the response (S3 Fig); it is possible that an initial fast component remained unchanged and that a second, larger component declined, but this is not clear from the results. To determine whether a similar phenomenon could have been initiated by attachment of the bead, we also conducted experiments monitoring the calcium signal along with bead position and force measurement during bead attachment (S4 Fig). We conclude from these experiments that when the bead attaches to the membrane, there is no major response or reaction in the cell.

In 3 experiments in which mechanical stimulation of the OS evoked a calcium transient, application of 10 μM M-theraphotoxin-Gr1a (GsMTx-4) abolished the response to subsequent mechanical stimulation (Fig 2N). These results indicate compartmentalization of calcium dynamics within the rod cytoplasm, and they suggest that rods are indeed mechanosensitive, i.e., that they express channels that can be activated by direct mechanical stimulation.

Light-induced changes in rod OS length

Given that *Xenopus* rods respond to mechanical stimuli, we decided to test whether they also exhibited changes in OS length upon illumination, such as the shrinkage of about 0.4–0.6 μm reported by Lu and colleagues [4,24]. We chose to use OTs because of their high sensitivity, on the order of 1–10 nm, and rapid temporal resolution, in the millisecond range [20]; see also Methods and S4 Fig. We used the OT to position a 3.5-μm polystyrene bead above the tip of a rod OS and then gently lowered the bead until it made contact with the OS (Fig 3A), and then established good adhesion, as indicated by a decrease of the noise in the quadrant photodetector (QPD) trace [10]. Once the bead has sealed to the tip of the OS in this way, its precise

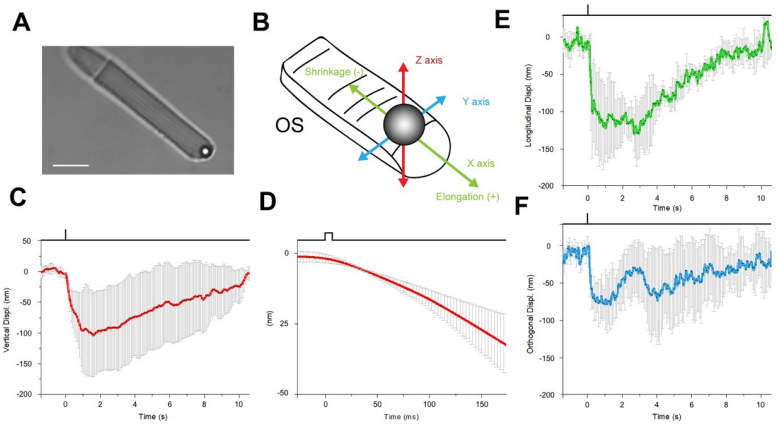

Fig 3. Mechanical response of an *X. laevis* rod to light flashes. The position of a bead sealed against the tip of the rod OS is monitored with OTs (see Methods). Following a bright flash of 491 nm, equivalent to about 10^4 R*, a transient shrinkage is observed. (A) Bright-field IR image, showing a trapped bead in contact with the tip of the rod OS (scale bar, 10 μm). (B) Detail of the 3D tracking system. (C) Light-induced shifts in the *Z* axis of the trapped bead (downward is negative). (D) Expansion of the time base in E to examine the delay between light stimulus and bead movement. (E) Bead displacement along the direction of the rod OS (shrinkage is negative, and elongation is positive). (F) Bead displacement in the direction perpendicular to the rod OS axis. Data are representative of mean ± SD of 5 different experiments. IR, infrared; OS, outer segment; OTs, optical tweezers.

https://doi.org/10.1371/journal.pbio.3000750.g003

position (monitored by the OTs) provides a measure of the length of the OS so that any light-induced changes in OS length are recorded as displacements of the bead. We were able to measure the bead displacement in the X, Y, and Z directions, and we could then express the motion in terms of a longitudinal displacement in the X, Y plane along the direction of the OS (monitoring OS shrinkage or elongation) and a displacement along the vertical *Z* axis (see Fig 3B).

Fig 3 shows bead displacements in response to brief flashes delivering around 2,500 R*/rod. We consistently observed a light-induced shortening of the OS on the order of 100–200 nm in different experiments, as indicated by the significant shift in the axial and orthogonal position of the bead in contact with the tip of the OS after the onset of the light stimulus (Fig 3E and 3F). The delay to the onset of the bead displacement was about 50 ms (Fig 3D, mean 42.5 ms ± 12, $n = 5$). The shortening was transient, and in all experiments the bead returned to its original position within about 10 s, which is similar to the recovery of the electrical response to a flash of this intensity.

To avoid the possibility of artifacts caused by the OTs method, we decided to use conventional video imaging to measure the light-induced shrinkage of OS length. Thus, we turned off the IR laser used for optical trapping and used IR video imaging to visualize rods in pieces of retina (Fig 4). In this way, we could measure OS shrinkage under conditions in which the OS motion was not restrained by the adhesion with the substrate. We compared bright-field time-lapse images recorded before and after a stimulus, and we computed the kymographs (Fig 4B) along the segments indicated in A. Following bilinear interpolation (Fig 4C), we obtained the intensity profile of the rod tips before and following the bright flash of light (Fig 4D), from

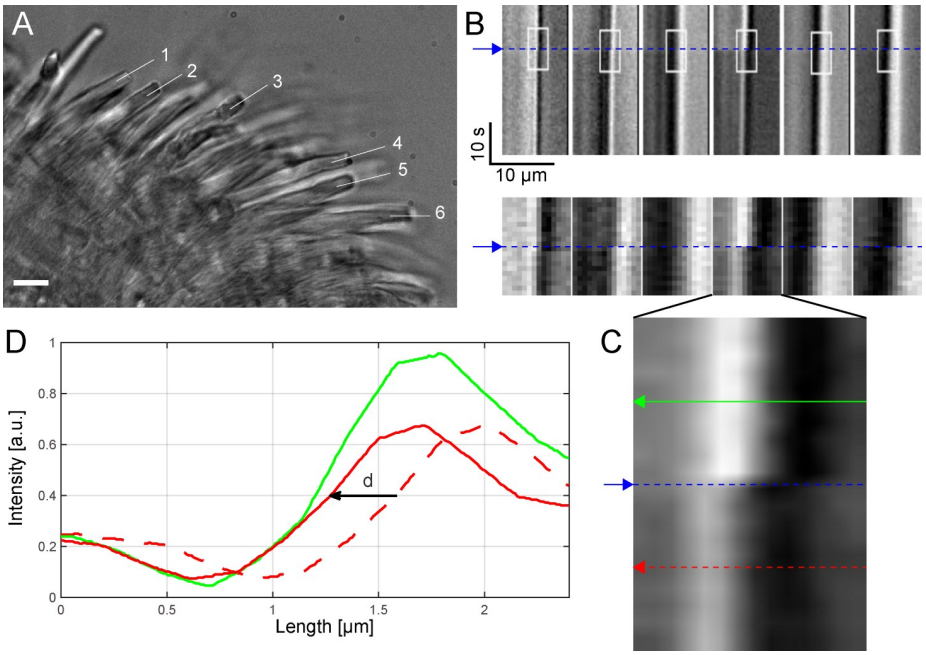

Fig 4. Light-induced shrinkage of intact rods in pieces of retina. (A) One frame from the movie (SI) showing a piece of retina with rods (scale bar, 10 μm). (B) Kymographs calculated along linear segments at the tip of the rods labeled with numbers from 1 to 6 in A show a shift, d: {d1 = 0.24, d2 = 0.32, d3 = 0.12, d4 = 0.31, d5 = 0.28, d6 = 0.33} μm in the intensity profile after the flash (blue line), confirming rod shrinkage. Small ROIs (white rectangles with size = 14 × 20 pixels) are selected and zoomed in the second row. (C) Bilinear interpolation of 1 ROI over a grid 20× bigger (280 × 400 pixels) than the original and 2 lines selected before and after the flash and used to calculate the shift d with subpixel precision. (D) Intensity profiles (green and dotted red) before and after flash. The shift d is calculated to minimize the difference between the intensity profiles (solid red and green lines) (S3 Data). a.u., arbitrary unit; ROI, region of interest.

https://doi.org/10.1371/journal.pbio.3000750.g004

which we calculated the OS shrinkage with subpixel resolution (see Methods) and found it varying from 120 up to 330 nm. OTs provide higher spatial resolution measurement of the time course of the light-evoked OS shrinkage but under conditions in which OS are restrained at some extent. Live cell imaging allows a measurement of OS shrinkage under more physiological conditions but at a much lower temporal resolution, i.e., of 500 ms.

The combination of these 2 approaches confirms that flashes delivering approximately 2,500 R*/rod trigger a rapid transient shortening—within 10–20 ms from the flash delivery—of *X. laevis* rods, similar to that reported recently in [4,24], in which it was referred to as transient retinal phototropism. The comparison of the rising phase of the photoresponse and of the time course of OS shortening shows that these 2 processes are fast, occurring with a similar delay from the onset of the light flash (see S5 Fig).

Rod photoresponses in the presence of MSC inhibitor

Given that rod photoreceptors show mechanosensitivity, we investigated the role of MSCs in phototransduction by recording rod photocurrents with a suction pipette and then applying the MSC inhibitor GsMTx-4 [25]. GsMTx-4 is a small peptide obtained from a spider venom and has been shown to inhibit several MSCs from both the Piezo and TRP families [26,27]. It is thought to act at the interface between the lipids in which the MSC is embedded [28], thereby reducing the effective magnitude of the mechanical stimulus acting on the MSC gate; thus, GsMTx-4 is a gate modifier rather than a specific ion pore blocker. According to Gnanasambandam and colleagues [28], GsMTx-4 is stabilized by lysine residues and occupies a small fraction of the surface area in unstressed membranes. When applied tension reduces lateral pressure in the lipid phase, those residues penetrate deeper, acting as "area reservoirs," leading to partial relaxation of the outer monolayer, thereby reducing the effective magnitude of the stimulus acting on the gate of the MSC.

We delivered GsMTx-4 using a second similar pipette connected to a picospritzer and positioned 50–100 μm from the OS of the recorded rod (Fig 5A). Prior to drug exposure, presentation of bright flashes of about 2,500 R*/rod [29] triggered suppression of the rod circulating current for 5 s (Fig 5B and 5C). When the inhibitor was gently injected into the bath, using around 4 psi of pressure, the OS of the recorded rod was displaced from its original position (compare upper and lower panels in Fig 5A), signaling the arrival of GsMTx-4. The same illumination then elicited photoresponses of shorter duration (compare black and red traces in Fig 5C; $n = 13$). Subsequently, after the injection of GsMTx-4 had been terminated, the photoresponses recovered their original time course (compare black and blue traces). When the same experiment was repeated in the absence of GsMTx-4 in the pipette but with a similar degree of OS displacement, no significant shortening of photoresponses was observed (Fig 5D and 5E; $n = 15$).

We analyzed the effect of GsMTx-4 on photoresponses to flashes with intensity ranging from dim (5 R*/rod) to bright (2,500 R*/rod); compare black and red traces in Fig 5F and 5G ($n = 10$ rods). Application of the MSC inhibitor had negligible effect on photoresponses to dim flashes ($n = 7–10$; Fig 5H), and it had relatively little effect for flashes of intermediate intensity (Fig 5F, 5G and 5I). It was only for flashes of saturating intensities (i.e., greater than approximately 100 R*/rod) that the time course was shortened by GsMTx-4, and for these saturating flashes, the magnitude of the response shortening increased with increasing flash intensity (see Fig 5I). We also analyzed photoresponses to steps of light lasting 20 s in control conditions and in the presence of GsMTx-4, and the rising and falling phases of these photoresponses were rather similar (see S6 Fig). Although the GsMTx-4 trace is very slightly smaller than the control, this might readily be explicable in terms of a slight rundown in the cell's circulating current.

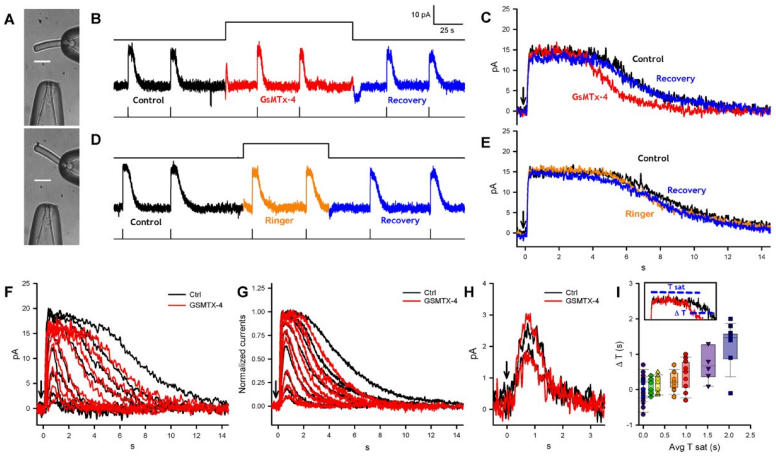

Fig 5. The effect of MSC blocker GsMTx-4 on photoresponses from *Xenopus* rods. (A) IS of a rod trapped in a recording pipette and a glass pipette connected to a picospritzer, containing GsMTx-4. Upon the activation of the picospritzer, the rod OS was tilted and returned to its initial position (scale bar, 20 μm). (B) The photocurrent elicited by flashes of about 2,500 R*/rod before, during, and after an exposure to GsMTx-4 lasting 120 s. (C) Exposure to GsMTx-4 (red trace) shortens the duration of the bright-flash photoresponse by more than 1 s compared with those obtained immediately before (black) and immediately after (blue) exposure to GsMTx-4; mean duration (measured as the difference in time between 50% of the falling phase and 50% of the rising phase of the response) 4.7 ± 1.8 s in control and 3.4 ± 1.3 s in GsMTx-4 ($p < 0.001$). (D and E) As in B and C, but the picospritzer injected Ringer solution. Mean duration 6.2 ± 1.7 s in control and 5.9 ± 1.9 s in Ringer (ns). (F) Comparison of photoresponses in control conditions (black traces) and in the presence of GsMTx-4 (red traces) for 1 cell exposed to flash of approximately 5, 10, 25, 50, 100, 250, 500, 1,000, and 2,500 R*/rod. (G) As in F, but in this case each trace was averaged over photoresponses obtained from 6–7 different rods. The amplitude of the maximal photoresponse was normalized to unity for recordings both in Ringer (black traces) and in the presence of GsMTx-4 (red traces). (H) The effect of GsMTx-4 on dim flash photoresponses for one cell; the flash intensities were 5 and 10 R*/rod ($n = 6–7$). (I) Relation between the GsMTx-4-induced shortening (ΔT) of photoresponse duration and the Tsat of the response. For 250, 500, 1,000, and 2,500 R*/rod, the shortened time courses were of 0.3 s, $p < 0.05$; 0.5 s, $p < 0.01$; 0.7 s, $p < 0.05$; and 1.3 s, $p < 0.001$, respectively. In all experiments, the concentration of GsMTx-4 in the picospritzer pipette was 5 μM, we estimate that at the rod OS was in the micromolar range; $n = 6–7$ (S4 Data). GsMTx-4, M-theraphotoxin-Gr1a; IS, inner segment; MSC, mechanosensitive channel; OS, outer segment; Tsat, saturation time.

https://doi.org/10.1371/journal.pbio.3000750.g005

Relationship of the *TRPC1* gene to the genes underlying vertebrate phototransduction

We examined gene synteny for both *TRPC1* and *PIEZO1*, and we discovered that the *TRPC1* gene is closely associated with several genes that encode proteins involved in the vertebrate phototransduction cascade. In particular, *TRPC1* is clearly a member of the paralogon that comprises the visual GRKs, the arrestins, and the visual GCs (guanylyl cyclases). We also found suggestive evidence that *PIEZO1* and *PIEZO2* may be located on another paralogon that includes the Cyclic Nucleotide-Gated ion channel Beta 1 (*CNGB1*) and *CNGB3* genes that encode cyclic nucleotide-gated ion channel (CNGC) β-subunits; this possibility deserves future examination.

The syntenic relationship between the TRPCs and the 3 other families of genes mentioned above is summarized in Fig 6; note that, for purposes of illustration, we have chosen to show just 4 families and just 2 species from the larger set presented in S8 Fig. Each column represents the remaining members of the quartet of genes that were generated from a single ancestral gene through 2 rounds of whole-genome duplication (2R WGD) in a protovertebrate organism some 500 million years ago (Mya). Each row shows a region of either 1 or 2 chromosomes in an extant organism, and where 2 regions are shown, this is presumed to be the result of chromosomal rearrangements over 500 My. Examination of the larger data set in S7 Fig

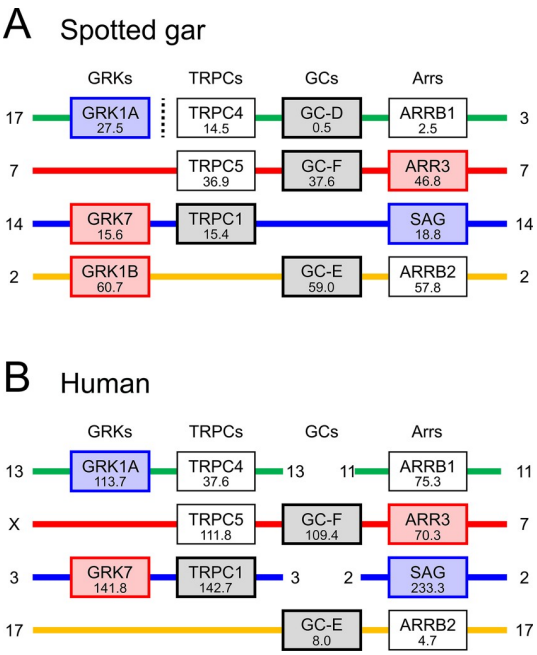

Fig 6. Summary of synteny for 4 gene families from 2 species. Gene locations are shown for TRPCs, visual GRKs, visual GCs, and arrestins. Number under each gene name represents the gene position in Mb on the indicated chromosome. Note that there is strong evidence that each interrupted row (where there is a break in continuity of a chromosome) corresponds to a contiguous set of genes in the ancestral quadruplicate genome. See S7 Fig for synteny across 11 gene families and 4 species. GC, guanylyl cyclase; GRK, G-protein receptor kinase; Mb, megabase; TRPC, transient receptor potential canonical.

https://doi.org/10.1371/journal.pbio.3000750.g006

provides powerful evidence that each of the 4 rows is contiguous and represents the current rearrangement of genes on the 4 ancestral chromosomes that existed shortly after 2R WGD.

In Fig 6, the proximity of TRPC family members to members of the other 3 families is impressive. For example, the distance from *TRPC1* to *GRK7* is just 0.2 megabases (Mb) in both spotted gar (Fig 6A) and chicken (S7B Fig) and is <1 Mb in both human (Fig 6B) and opossum (S7C Fig). Likewise, the distance from *TRPC5* to GC-F (= *GUCY2F*) is <1 Mb in spotted gar (Fig 6A) and <2.5 Mb in human (Fig 6B); in the other 2 species, the loss of the gene for GC-F precludes this comparison (S8 Fig). Furthermore, as shown previously [30], in several cases members of the other 3 families of phototransduction genes are close to each other; for example, *GRK1B*, GC-E, and *ARRB2* are close to each other in spotted gar (Fig 6A). Such proximity in extant chromosomes is an important telltale sign of ancient proximity because of the very low likelihood that random chromosomal rearrangements could bring so many genes into mutual proximity; instead, random rearrangements are likely to obscure any proximity that originally occurred. Therefore, we conclude that it is very likely that in a protovertebrate organism, the ancestral genes (TRPC, visual GRK, visual GC, and arrestin) were arranged in close proximity to each other prior to quadruplication during 2R WGD.

Localization of MSCs in *X. laevis* rods

To better investigate the expression of MSCs Piezo1 and TRPC1 in rods, we stained retinas by immunofluorescence with antibodies for Piezo1 and TRPC1 (see Methods). Immunolabeling for Piezo1 (Fig 7A) shows a clear staining in rods, with a punctate expression in the ellipsoid region of the IS. On the other hand, in Fig 7B, the apparent labeling for TRPC1 along the OS may in fact represent autofluorescence associated with the high density of rhodopsin

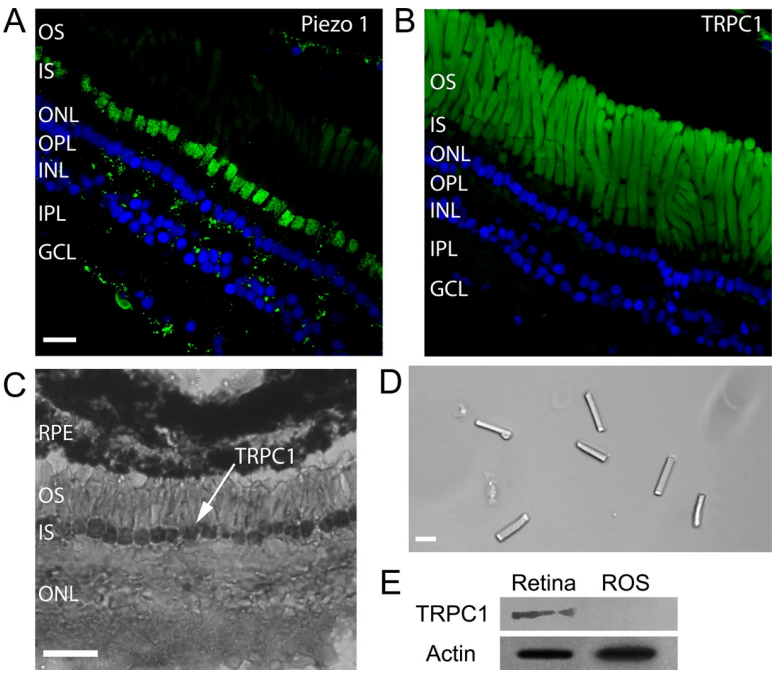

Fig 7. Expression of mechanosensitive channels in the *X. laevis* retina. (A) Immunofluorescence for Piezo1 in green and DAPI in blue. (Scale bar is 20 μm for images A, B, and D.) (B) Immunofluorescence for TRPC1 in green and DAPI in blue. (C) Immunohistochemistry for TRPC1. (Scale bar, 50 μm.) (D) Isolated OS obtained by sucrose centrifugation. (E) WB for TRPC1 from the whole retina and isolated ROS as those shown in D. GCL, Ganglion Cell Layer; INL, Inner Nuclear Layer; IPL, Inner Plexiform Layer; IS, inner segment; ONL, Outer Nuclear Layer; OPL, Outer Plexiform Layer; OS, outer segment; ROS, Rod outer segment; RPE, Retinal Pigment Epithelium; TRPC, transient receptor potential canonical; WB, western blot.

https://doi.org/10.1371/journal.pbio.3000750.g007

molecules [31]; accordingly, these data cannot be taken to show definitive expression of TRPC1 in rod OSs.

Molnar and colleagues [32] have shown that TRPC1 is expressed mostly in rod ISs in mouse, using RNA in situ hybridization with nitroblue tetrazolium. To get clearer evidence on the expression patterns of TRPC1, we decide to perform immunohistochemical staining of *Xenopus* retinas with the same antibody used for the immunofluorescence. Indeed, immunohistochemical staining confirmed that TRPC1 is expressed primarily on the IS membrane of rod photoreceptors (Fig 7C) with possible weaker staining also in the OSs. Moreover, we isolated rod OSs (Fig 7D), IS + OS, by purification on an OptiPrep gradient, [33] and we performed standard western blot (WB) with antibodies for TRPC1 (Fig 7E). This analysis shows that TRPC1 and Piezo1 channels are abundantly present in the retina and in ISs, but not in the OSs (Fig 7D). This conclusion is in agreement with the conclusions of previous proteomic studies [18,19], which did not report the presence of Piezo and TRP channels either in OSs or in disks. We were not able to determine the presence or absence of TRPC1 and Piezo1 channels in a population of isolated and purified disks by WB analysis.

Discussion

The present manuscript shows a number of novel, to our knowledge, features of rod photoreceptors involving mechanosensitivity and mechanosensitive channels. TRPC1 and Piezo1 MSCs are present in rod photoreceptors; in addition, it has long been known that the actomyosin complex is associated with the ciliary machinery linking the light-sensitive OS to the IS

[34]. Interestingly, weak mechanical stimulation—on the order of 10 pN—applied briefly to either the OS or IS evokes clear calcium transients, which are inhibited by the toxin GsMTx-4. Moreover, the inhibition of MSCs through GsMTx-4 decreases the duration of photoresponses to bright flashes, and the magnitude of this effect increases with flash intensity. The genes for the TRPC family appear to have an ancient association with 3 other families of genes that are directly involved in phototransduction in the rod OS. These results suggest that MSCs play an integral role in the regulation of rod phototransduction.

Both TRPC1 and Piezo1 channels are multimodal and have been reported to be gated and modulated by temperature and second messengers. The observation that very weak mechanical stimulation of the IS elicits a transient increase in intracellular calcium concentration is consistent with the view that these ionic channels in the IS are mechanosensitive. Mechanosensitivity in OSs seems to have a more complex origin; weak mechanical stimulations evoke brief calcium transients (Fig 1), but we have not been able to determine in a conclusive way the presence of TRPC1 and Piezo1 and 2 channels in the OS. It is possible, however, that in the OS there are additional MSCs or that mechanosensitivity has a different origin: it is conceivable, indeed, that the small indentation occurring during the applied mechanical stimulations—on the order of some hundreds of nanometers—disrupts disks known to be filled by calcium ions [35] and therefore induces a localized transient calcium increase. In some experiments (see S5 Fig), we observed that in the presence of GsMTx-4, mechanical stimulation did not evoke any calcium transients, but spontaneous calcium transients could be observed. This observation suggests that calcium transients could occur in the absence of any apparent mechanical stimulation and that mechanical stimulations could modulate the frequency of these transients. In conclusion, we are confident that we have identified the molecular origin of mechanosensitivity in the IS, but mechanosensitivity in the OS could involve both MSCs and a direct mechanical action on the disks.

We observed that GsMTx-4 caused a shortening of the duration of bright-flash responses (Fig 5B and 5C). The exposure to GsMTx-4 does not induce any measurable change in the amplitude of the saturating current (Fig 5C), indicating either that MSCs are not activated in dark-adapted conditions (i.e., before the exposure to the bright flash) and/or that the ionic current flowing through MSCs is small and cannot be easily measured. On the basis of these observations, we suggest that in the presence of GsMTx-4, a bright flash results in a more pronounced light-induced drop in calcium concentration because the MSCs are inhibited. Thus, the inhibition of MSCs will block an influx of calcium into the cytoplasm that is normally stimulated by mechanical movement of the OS triggered by the bright flash and thereby result in a larger decline in free calcium concentration. The ensuing shortening of the bright-flash photoresponses could result from an effect of the lowered calcium concentration via either increased cyclase activity [36] or decreased R^* lifetime [37,38] or both.

If MSC channels are activated during phototransduction, a key issue is what mechanical stimulation activates them? Three possibilities spring to mind: activation of the actomyosin complex; a drop of intracellular osmotic pressure caused by the transient abolition of the photocurrent, and dimensional changes such as the light-induced shortening of the rod OS (Fig 3 and [4,24]). We suggest that the first of these is unlikely; although the IS is rich in actin, in the OS actin is present only at its base and not in the whole OS.

We have not been able to estimate the magnitude of any light-induced change in intracellular osmotic pressure, though we expect it will be small. Although suppression of the dark current of 50 pA corresponds to a reduction in the entry into the OS of around 1.5×10^8 monovalent cations per second, this is counterbalanced by an equal reduction of current flow out of the OS and into the IS [39]. Therefore, in response to a saturating flash of light, it is possible that a drop in osmolarity develops, but it seems likely that the reduced efflux of positive charge from the OS to the IS through the ciliary neck may minimize this effect.

In agreement with previous observations [4,24], we confirm that bright flashes of light elicit a transient shortening of the rod OS. These flash-induced movements begin with a delay around 50 ms for a flash of about 2,500 R^*/rod (Fig 3). This transient shortening of OSs, also referred as transient retinal phototropism, is thought to be associated with early, disk-based stages of the phototransduction cascade [4] and is not caused by the light-induced suppression of the photocurrent. Transmission electron microscopy shows that the shrinkage is associated with a decrease in the space between disks rather than any change in thickness of the disks themselves [4], and this decrease in OS cytoplasmic volume will necessarily cause an increase in osmotic pressure. Hence, we propose that activation of MSCs is elicited either directly by the change in interdisk spacing (especially if MSCs are located in the disk membranes) or secondarily by the change in cytoplasmic osmotic pressure. We are aware, however, that this reduction of interdisk spacing will initiate adjustments of the hydrostatic pressure and of water volume that have to be properly addressed and understood.

The transient shortening of rod OS is likely to play a major role in phototransduction, which is, at the moment, not entirely understood. This shortening is associated with the early stages of phototransduction occurring within some tens of milliseconds following rhodopsin activation [4], and it is not clear how the biochemical cascade initiated by photon absorption leads to a shrinkage of the interdisk space; we believe that this shrinkage represents a missing step for a complete and full understanding of phototransduction.

Although it is widely thought that sensory neurons (such as photoreceptors) are specialized to transduce just a single sensory modality, the present investigation not only shows that rods express MSCs but also demonstrates that they display mechanosensitivity. We hypothesize that rod photoreceptors require such mechanosensitivity both for the optimal operation of the phototransduction machinery and for the maintenance of cellular integrity.

Methods

Ethics statement

All the experiments described in this manuscript were performed in accordance with the guidelines of the International School for Advanced Studies ethics committee and according to the Italian and European procedures for animal care (d.l. 116/92; 86/609/C.E.).

Immunofluorescence

Retinas were fixed with 4% paraformaldehyde for 60 min at room temperature, followed by permeabilization with PBS plus 0.1% Triton X-100, blocked with 1% BSA (Bovine Serum Albumin) and incubated overnight with primary antibodies anti-Piezo1 (1:300) or anti-TRPC1 (1:300) from Alomone Labs (Jerusalem, Israel). Retinas were then washed with cold PBS 3 times for 5 min each and incubated with Alexa 488-labeled goat anti-mouse secondary antibody (1:400) or Alexa 594-labeled goat anti-rabbit secondary antibody (1:400) and actin (phalloidin) (1:50) at room temperature for 1 h and then stained with Hoechst (all from Life Technologies, Carlsbad, CA, USA). Retinas were examined with a NIKON A1R confocal microscope (Nikon, Tokyo, Japan) equipped with 405, 488, and 561 excitation lasers, 40× objective (NA 0.75) and 60× oil immersion objective (NA 1.40).

Isolation of photoreceptors and electrical recordings

The eyes of *X. laevis* frogs were enucleated and hemisected under a stereotactic microscope with an IR 820 nm illumination. Dissociated rods were obtained as reported previously [29]. Briefly, the intact rods obtained by mechanical dissociation were immersed in Ringer solution

containing 110 mM NaCl, 2.5 mM KCl, 1 mM CaCl2, 1.6 mM MgCl2, 3 mM HEPES-NaOH, 0.01 mM EDTA, and 10 mM glucose (pH 7.7–7.8, buffered with NaOH). All chemicals were purchased from Sigma-Aldrich (St. Louis, MO, USA). All experiments were performed between 22˚C and 24˚C and images acquired using HCImage software 4.3.1.33 (Hamamatsu Corporation, Bridgewater, NJ, USA).

S1 Fig shows representative images of rods following mechanical dissociation in bright field (B) and in fluorescence (A and C) emitted by our dye CaSiR-1. More than 30% of the isolated rods are composed of an IS and OS where the IS is bright and the base of the OS is dark and its tip more luminous. These ISs + OSs are functional rods because they exhibit a light response (measured as a change in fluorescence).The quality of the preparation varies with the animal and the skill of the experimenter, as shown in panel E of the above figure, but most IS + OS rods are functional, varying from 75% up to 100%.

From our previous experience, toad rods (*Bufo marinus* and *B. bufo*) are rather fragile, but rods from the tiger salamander (*Ambystoma tigrinum*) are much more robust. We have observed that rods from *X. laevis* frogs, properly dissociated, are often functional. In addition, *X. laevis* frogs are easier to keep than tiger salamanders, and they also reproduce well in captivity. These are the reasons we have opted to work with *X. laevis* rods.

After mechanical isolation, electrical recordings were obtained as described in [24]. Rods were viewed under 900-nm light using 2 cameras (Hamamatsu ORCA-Flash 4.0; Hamamatsu Corporation and Jenoptic ProgRes MF; JENOPTIK I Optical Systems, Goeschwitzer, Jena, Germany) at 2 magnifications and stimulated with 491-nm diffuse light (Rapp OptoElectronic, Hamburg, Germany) from the ×10 objective of an inverted microscope (Olympus IX71; Olympus Corporation, Tokyo, Japan). Photoresponses were recorded using an Axopatch 200A (Molecular Devices, San Jose, CA, USA) in voltage-clamp mode. The current was digitized at 10 kHz and low-pass filtered at 20 Hz. All recordings were processed, analyzed, and baseline corrected with Clampfit 10.3 (Molecular Devices).

Calcium imaging

Retinas were loaded with a cell-permeable calcium dye CaSiR-AM (Life Technologies) and Pluronic F-127 20% solution in DMSO (Life Technologies) at a ratio of 1:1 in Krebs-Ringer's solution containing 119 mM NaCl, 2.5 mM KCl, 1 mM NaH_2PO_4, 2.5 mM $CaCl_2$, 1.3 mM $MgCl_2$, 11 mM D-glucose, and 20 mM HEPES (pH 7.4) at 37˚C for 45 min. After incubation, the isolated rods were washed 3 times for at least 15 min total to allow complete intracellular de-esterification of the dye, then transferred to the stage of an Olympus IX-81 inverted microscope equipped with LED illumination (X-Cite XLED1 from Excelitas Technologies, Waltham, MA, USA). The experiments were performed at room temperature (between 22˚C and 24˚C), and images were acquired using Micromanager software with an Apo-Fluor 60×/1.4 NA objective at a sampling rate of 5 Hz for 3–10 min.

Changes of intracellular calcium were quantified by computing DF/F = (F(t = 0)–F(t))/F(0), where F(0) is the fluorescence intensity at the beginning of the experiment and F(t) is the fluorescence intensity at time t. The fluorescence analyzed in panels C, D, G, H, M, and N of Fig 2 was computed in the large region indicated by the white boxes in Fig 2B, 2F and 2L. In panels B, F, and L, the color maps indicate DF/F computed at each pixel within the white box after a spatial averaging in a window of 3 × 3 pixels.

Mechanical stimulation using the oscillatory optical trap

To mechanically stimulate the cell, we used a polystyrene bead with a diameter d = 3.5 μm (G. Kisker GbR, Steinfurt, Germany) optically manipulated in an oscillatory optical trap (OOT)

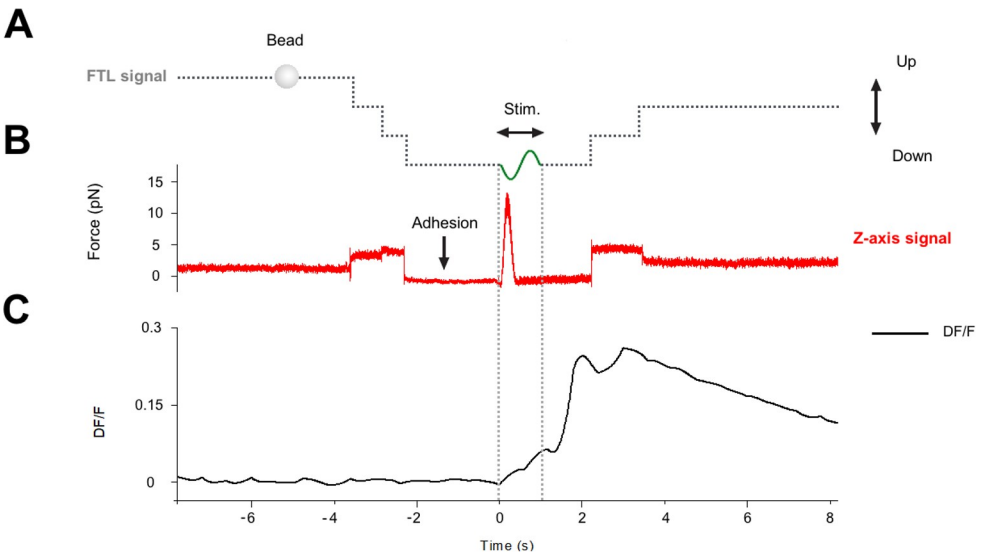

Fig 8. Analysis of the recording of the QPD trace and of DF/F. (A) Voltage command to the FTL, controlling the vertical displacement of the optical trap. The steps in the dotted lines show the lowering of the bead before adhesion and raising of the bead after mechanical stimulation. (B) Force recorded in the vertical direction by the QPD. (C) Fluorescence signal DF/F monitoring the level of intracellular calcium. There was no change in DF/F at the time of the adhesion of the bead (marked by a decrease of noise in the force trace), but DF/F increased following the mechanical stimulation, indicated by "Stim." FTL, Focused Tunable Lens; QPD, quadrant photodetector.

https://doi.org/10.1371/journal.pbio.3000750.g008

(S2 Fig). The main component of the OOT is the Focused Tunable Lens (FTL; EL-10-30-NIR-LD, Optotune AG, Dietikon, Switzerland), of which the focal length can be precisely tuned to change the vertical position of the trapped bead. Cell stimulation is achieved by trapping the bead above the cell and then moving it against the cell membrane. A complete description of all components of the setup are found in [10]. The setup can be used for measuring displacements (Fig 3) and for applying forces (Fig 4), and the shift between the 2 modes of operation is obtained by inserting the FTL into the optical path of the laser when applying forces (see S2 Fig).

Analysis of the recording of the QPD trace and of DF/F (see Fig 8) allows us to determine the moment in which the bead attaches/seals to the membrane and this event is not associated with any change of DF/F. The moment in which the bead seals to the membrane is revealed by a decrease of the noise in the QPD recording, in a way reminiscent of what occurs when a patch pipette seals on the membrane in electrophysiological experiments. We conclude from these experiments that when the bead attaches to the membrane, there is no major response or reaction of the cell.

Measurement of the rod shrinkage by bright-field time-lapse imaging

We used an objective lens with 60× magnification, numerical aperture NA = 1.4, and a Hamamatsu ORCA-D2 camera with a sensor pixel size of 6.5 μm. Considering the light wavelength, λ = 750 nm, the lateral optical resolution is r of approximately 320 nm. The sensor resolution is given by the pixel size. We used binning 2×; thus, 1 image pixel corresponds to about 220 nm on the sample ($p = 6.5 \times 2 \times 1{,}000/60 = 216.7$ nm to approximately 220 nm). The sensor resolution matches the optical resolution at the limit $3p$ is approximately $2p$ (matching condition: $3p \geq 2p$). The experiment consists in recording the image of a piece of retina before and after a flash of light at 2 frames/s and observing potential retraction of the rods. One frame illustrating a piece of retina with rods is shown in Fig 4A. We measure the retraction of the

rods indicated in figure with numbers from 1 to 6. For each rod, we define a segment of the same length (L = 10 μm) along the rod axis (white lines), and we calculate the kymograph. The kymogaph is a graph space versus time, showing how the intensity distribution along the segment varies in time (Fig 4B). This variation is directly related to a potential retraction of the rod. As one can observe from the kymograph, after the flash (indicated by the blue line), there is a clear shift of the gray value, Δ, corresponding to the retraction of the rod. We calculate the values for the shift Δ with subpixel precision. To do this, we first select small regions of interest (white rectangles in Fig 4B) of size ROI = 14 × 20 pixels. Then, using bilinear interpolation, we define a new ROI over a grid with 20 times more points (pixels) in each direction than that of the original ROI (Fig 4C). We then plot the intensities along the green and red lines, corresponding to the darker and lighter regions (after flash). To determine the shift Δ, we calculate the quantity: $A = \int[(Id(x - \Delta) - Il(x)])^2]dx$, where Id(x) and Il(x) represent the intensity profiles for dark and light regions and $\Delta = k \times p/20$, with k = 1:40. The subpixel value of the shift Δ is given by k for which the quantity A is minimized (Fig 4D). We found that the rods shifted by $\Delta > 240$ nm (i.e., more than 1 pixel), except rod 3, for which Δ = 120 μm. The maximum shift Δ max = 330 nm corresponds to rod 6.

Data and statistical analysis

For calcium experiments, the DF/F values were obtained through custom MATLAB (The MathWorks, Natick, MA, USA) code and the ImageJ software v1.6 (National Institutes of Health, Bethesda, MD, USA). All results are presented as mean ± SD, and significant differences were determined using a *t* test with $p < 0.05$ (GraphPad Prism 7, GraphPad software, San Diego, CA, USA). For electrophysiological experiments, the parameters of rod responses were analyzed with Clampfit 10.3, and the statistical significance was determined using the paired *t* test in SigmaPlot 13.0.

Supporting information

S1 Fig. The quality of the preparation. (A and C) Images of the fluorescence emitted by the calcium fluorescent dye CaSiR from rods in the preparation. (B) is a bright-field image obtained with a light source at 750 nm corresponding to the fluorescent image in A. Rods were viewed with a 60× objective, and of the 4 rods viewed in B, 3 were composed of IS + OS (labeled 1, 2, and 3). (D) Photoresponses obtained from the IS + OS shown in A and C. The blue traces are the light stimulus monitor; flash intensity was equivalent to about 10^4 R*. Numbers near the traces in D were obtained from the IS + OS with the same number in A and C. (E) Fraction of IS + OS rods out of the total number of rods in 10 representative preparations (S5 Data). (F) Fraction of IS + OS rods from which photoresponses could be measured out of the total number of ISs + OSs in that preparation (S6 Data). These fractions from each preparation were obtained from 10 random fields of view such as those shown in A–C. CaSiR, Calcium ion detecting probe based on silicon rhodamine; IS, inner segment; OS, outer segment. (TIF)

S2 Fig. Optical manipulation and imaging setup. 1, inverted microscope; 2, OOT; 3, force measurement module. Optical components: L1, L2, convergent lenses, f1 = f2 = 100 mm; M1, mirror; FTL, fFTL = 55–90 mm; FL, f = 150 mm; DM1 (900 dcsp; Chroma, Bellows Falls, VT, USA); DM2 (XF22045, Chroma); TL; MO, Olympus 60×, NA 1.4, oil immersion; DO, 10×, NA 0.3; DM3 (900 dcsp, Chroma); L3, convergent lens, f = 40 mm. dcsp, Dichroic ShortPass; DM, Dichroic Mirror; DO, condenser objective; FL, Fixed focal Lens; FTL, Focused Tunable Lens; MO, Microscope Objective; NA, numerical aperture; OOT, oscillatory optical trap;

QPD, quadrant photodetector; TL, Tube Lens
(TIF)

S3 Fig. The effect of repeated mechanical stimulations. (A) Trapped bead in contact with the base of the rod OS under bright-field IR imaging. (B) Fluorescence change (DF/F) images, showing the ROI (white box) used to quantify the fluorescence change versus time before and during the first mechanical stimulation. (C) Calcium transients evoked by the repeated mechanical stimulations (indicated by the dark arrow). The amplitude of the first and fast calcium transient (indicated by the horizontal red line) is reproducible, while the second and larger component declines. IR, infrared; OS, outer segment; ROI, region of interest
(TIF)

S4 Fig. Video imaging of the effect of light on the length of rod OS. (A) A bright-field view of a piece of retina under IR light at 750 nm. (B) Zoom of the yellow dotted box in A. (C) Zoom of the tips of OS in the yellow dotted squares before illumination, during illumination, and after 20 s. The light-induced shortening of the rod OS corresponds to 2–4 pixels: given that a pixel corresponds to approximately 120 nm, the shortening is on the order of 200–400 nm. The enclosed video provides additional support to the light-induced OS shortening. IR, infrared; OS, outer segment.
(TIF)

S5 Fig. Comparison of the time course of the electrical response measured with suction pipette and shortening measured with OTs. (A) Upper panel, 3 photoresponses to flashes of light equivalent to about 0.5, 1, and 2.5×10^4 R^* (red, blue, and black traces, respectively); lower panel, time course of shortening evoked by a flash of light at 491 nm, equivalent to about 10^4 R^*. (B) As in A, but on a more expanded timescale; (C) superposition of all these traces after normalization of the maximum to 1. Traces in the upper panel of A were obtained from the same cell, and the trace in the lower panel of B was the average of 5 different experiments to the same light flash in different cells. OTs, optical tweezers.
(TIF)

S6 Fig. Comparison of the response to a step of light of 20 s duration and equivalent to about 250 Rh^*/s in control conditions (black) and in the presence of GsMTx-4 (red) from the same cell. Maximal photoresponse to a saturating flash of light was 18 pA. GsMTx-4, M-theraphotoxin-Gr1a.
(TIF)

S7 Fig. Spontaneous calcium transients in the presence of GsMTx-4. (A) A trapped bead in contact with the rod OS under bright-field IR imaging. (B) Fluorescence change (DF/F) images, showing the 2 ROIs used to quantify the fluorescence change versus time. (C) Time course of the evoked DF/F change from the 2 ROIs in B. Mechanical stimulation (black arrow) as indicated in B. In the presence of GsMTx-4, mechanical stimulation did not evoke any calcium transients, but spontaneous calcium transients could be observed. GsMTx-4, M-theraphotoxin-Gr1a; IR, infrared; OS, outer segment; ROI, region of interest.
(TIF)

S8 Fig. Syntenic arrangement for a set of 11 families of genes in the vicinity of *TRPC1*, *TRPC4*, and *TRPC5* across 4 species. Note that only a subset of these families and species was shown in Fig 5. Each panel depicts the arrangement of genes on chromosomes in the named species, and each column depicts a family of paralogous genes. Each row depicts a section of either 1 chromosome or, in several cases, 2 chromosomes, and in one case, 3 chromosomes. Numbers at the ends of each row denote the chromosome, and the numbers under the gene

names give the position of the gene in Mb. For rows that include more than 1 chromosome, dotted vertical bars show breaks between chromosomes, and the chromosome number and gene position are both listed. Expression in photoreceptor classes is indicated by colored shading as follows: red in cones, blue in rods, and gray in both (or uncertain). Gene names are HGNC where present in human, except for the GCs, for which the IUPAR/BPS names are used: GC-E (encoded by *GUCY2D* in human); GC-F (encoded by *GUCY2F*); GC-D (missing from human; olfactory elsewhere). Question mark indicates gene on an unplaced scaffold, and so the presumed chromosomal location is shown. GC, guanylyl cyclase; IUPAR/BPS, International Union of Basic and Clinical Pharmacology/British Pharmacological Society; Mb, megabase; TRPC, transient receptor potential canonical.
(TIF)

S1 Movie. Video imaging of the effect of light on the length of rod OS, presented in S4 Fig. The light-induced shortening of the rod OS corresponds to 2–4 pixels: given that a pixel corresponds to approximately 120 nm, the shortening is on the order of 200–400 nm. The enclosed video provides additional support to the light-induced OS shortening. OS, outer segment.
(AVI)

S1 Data. Original numerical values for Fig 2I.
(CSV)

S2 Data. Original numerical values for Fig 2J.
(CSV)

S3 Data. Original numerical values for Fig 4D.
(XLSX)

S4 Data. Original numerical values for Fig 5.
(XLSX)

S5 Data. Original numerical values for S1E Fig.
(XLSX)

S6 Data. Original numerical values for S1F Fig.
(XLSX)

S1 Raw Image. Raw image of the WB presented in Fig 7E. WB, western blot.
(PDF)

Author Contributions

Conceptualization: Ulisse Bocchero, Fabio Falleroni, Simone Mortal, Vincent Torre.

Data curation: Ulisse Bocchero, Fabio Falleroni, Simone Mortal, Yunzhen Li.

Formal analysis: Simone Mortal.

Investigation: Ulisse Bocchero, Fabio Falleroni, Yunzhen Li.

Resources: Dan Cojoc.

Writing – original draft: Ulisse Bocchero, Fabio Falleroni, Simone Mortal, Trevor Lamb, Vincent Torre.

Writing – review & editing: Ulisse Bocchero, Fabio Falleroni, Simone Mortal, Trevor Lamb, Vincent Torre.

References

1. Zhang P, Zawadzki RJ, Goswami M, Nguyen PT, Yarov-Yarovoy V, Burns ME, et al. In vivo optophysiology reveals that G-protein activation triggers osmotic swelling and increased light scattering of rod photoreceptors. Proceedings of the National Academy of Sciences. 2017; 114: E2937–E2946. https://doi.org/10.1073/pnas.1620572114 PMID: 28320964
2. Hardie RC, Franze K. Photomechanical responses in Drosophila photoreceptors. Science. 2012; 338: 260–264. https://doi.org/10.1126/science.1222376 PMID: 23066080
3. Juusola M, Dau A, Song Z, Solanki N, Rien D, Jaciuch D, et al. Microsaccadic sampling of moving image information provides Drosophila hyperacute vision. Rieke F, editor. eLife. 2017; 6: e26117. https://doi.org/10.7554/eLife.26117 PMID: 28870284
4. Lu Y, Benedetti J, Yao X. Light-induced length shrinkage of rod photoreceptor outer segments. Translational Vision Science & Technologi. 2018; 7: 29.
5. Árnadóttir J, Chalfie M. Eukaryotic mechanosensitive channels. Annual Review of Biophysics. 2010; 39: 111–137. https://doi.org/10.1146/annurev.biophys.37.032807.125836 PMID: 20192782
6. Connelly T, Yu Y, Grosmaitre X, Wang J, Santarelli LC, Savigner A, et al. G protein-coupled odorant receptors underlie mechanosensitivity in mammalian olfactory sensory neurons. Proceedings of the National Academy of Sciences. 2015; 112: 590–595. https://doi.org/10.1073/pnas.1418515112 PMID: 25550517
7. Booth IR. Bacterial mechanosensitive channels: Progress towards an understanding of their roles in cell physiology. Current Opinion in Microbiology. 2014; 18: 16–22. https://doi.org/10.1016/j.mib.2014.01.005 PMID: 24607989
8. Booth IR, Miller S, Müller A, Lehtovirta-Morley L. The evolution of bacterial mechanosensitive channels. Cell Calcium. 2015; 57: 140–150. https://doi.org/10.1016/j.ceca.2014.12.011 PMID: 25591932
9. Rojas ER, Huang KC, Theriot JA. Homeostatic cell growth is accomplished mechanically through membrane tension inhibition of cell-wall synthesis. Cell Systems. 2017; 5: 578–590.e6. https://doi.org/10.1016/j.cels.2017.11.005 PMID: 29203279
10. Falleroni F, Torre V, Cojoc D. Cell mechanotransduction with piconewton forces applied by optical tweezers. Frontiers in Cellular Neuroscience. 2018; 12: 1–11. https://doi.org/10.3389/fncel.2018.00001
11. Delmas P, Coste B. Mechano-gated ion channels in sensory systems. Cell. 2013; 155: 278. https://doi.org/10.1016/j.cell.2013.09.026 PMID: 24120130
12. Minke B, Cook B. TRP channel proteins and signal transduction. Physiological Reviews. 2002; 82: 429–472. https://doi.org/10.1152/physrev.00001.2002 PMID: 11917094
13. Clapham DE. TRP channels as cellular sensors. Nature. 2003; 426: 517–524. https://doi.org/10.1038/nature02196 PMID: 14654832
14. Montell C. The TRP superfamily of cation channels. Science STKE. 2005; 2005: re3. https://doi.org/10.1126/stke.2722005re3 PMID: 15728426
15. Myers BR, Saimi Y, Julius D, Kung C. Multiple unbiased prospective screens identify TRP channels and their conserved gating elements. Journal of General Physiology. 2008; 132: 481–486. https://doi.org/10.1085/jgp.200810104 PMID: 18955590
16. Clapham DE, Runnels LW, Strübing C. The TRP ion channel family. Nature Reviews Neuroscience. 2001; 2: 387–396. https://doi.org/10.1038/35077544 PMID: 11389472
17. Maroto R, Raso A, Wood TG, Kurosky A, Martinac B, Hamill OP. TRPC1 forms the stretch-activated cation channel in vertebrate cells. Nature Cell Biology. 2005; 7: 179–185. https://doi.org/10.1038/ncb1218 PMID: 15665854
18. Panfoli I, Musante L, Bachi A, Ravera S, Calzia D, Cattaneo A, et al. Proteomic analysis of the retinal rod outer segment disks. J Proteome Res. 2008; 7(7): 2654–2669. https://doi.org/10.1021/pr7006939 PMID: 18489131
19. Kwok MCM, Holopainen JM, Molday LL, Foster LJ, Molday RS. Proteomics of photoreceptor outer segments identities a subset of SNARE and rab proteins implication in membrane vesicle trafficking and fusion. Molecular & Cellular Proteomics. 2008; 7: 1053–1066. https://doi.org/10.1074/mcp.M700571-MCP200 PMID: 18245078
20. Neuman KC, Block SM. Optical trapping. Review of Scientific Instruments. 2004;2787. https://doi.org/10.1063/1.1785844 PMID: 16878180
21. Egawa T, Hanaoka K, Koide Y, Ujita S, Takahashi N, Ikegaya Y, et al. Calcium ion and its application to multicolor neuronal Imaging. Journal of the American Chemical Society. 2011; 14157–14159. https://doi.org/10.1021/ja205809h

22. Biernbaum MS, Bownds M. D. Frog rod outer segments with attached inner segment ellipsoids as an in vitro model for photoreceptors on the retina. J Gen Physiol. 1985; 85: 83–105. https://doi.org/10.1085/jgp.85.1.83 PMID: 3871471

23. Wetzel RK, Arystarkhova E, Sweadner KJ. Cellular and Subcellular Specification of Na, K-ATPase and Isoforms in the Postnatal Development of Mouse Retina. 1999; 19: 9878–9889.

24. Lu Y, Wang B, Pepperberg DR, XIncheng Y. Stimulus-evoked outer segment changes occur before the hyperpolarization of retinal photoreceptors. Biomedical Optics Express. 2017; 8: 8139–8145.

25. Suchyna TM, Johnson JH, Hamer K, Leykam JF, Gage DA, Clemo HF, et al. Identification of a peptide toxin from grammostola spatulata spider venom that blocks cation-selective stretch-activated channels. Journal of General Physiology. 2000; 115(5): 583–598. https://doi.org/10.1085/jgp.115.5.583 PMID: 10779316

26. Spassova MA, Hewavitharana T, Xu W, Soboloff J, Gill DL. A common mechanism underlies stretch activation and receptor activation of TRPC6 channels. Proceedings of the National Academy of Sciences. 2006; 103: 16586–16591.

27. Bae C, Sachs F, Gottlieb PA. The mechanosensitive ion channel Piezo1 is inhibited by the peptide GsMTx4. Biochemistry. 2011; 50: 6295–6300. https://doi.org/10.1021/bi200770q PMID: 21696149

28. Gnanasambandam R, Ghatak C, Yasmann A, Nishizawa K, Sachs F, Ladokhin AS, et al. GsMTx4: Mechanism of inhibiting mechanosensitive ion channels. Biophysj. 2017; 112: 31–45. https://doi.org/10.1016/j.bpj.2016.11.013 PMID: 28076814

29. Bocchero U, Tam BM, Chiu CN, Torre V, Moritz OL. Electrophysiological Changes During Early Steps of Retinitis Pigmentosa. Investigative Ophthalmology and Visual Science. 2019; 60: 933–943. https://doi.org/10.1167/iovs.18-25347 PMID: 30840038

30. Lamb TD, Hunt DM. Evolution of the calcium feedback steps of vertebrate phototransduction. Open Biology. 2018; 8(9): 180119. https://doi.org/10.1098/rsob.180119 PMID: 30257895

31. Farrens DL, Gobind KH. Structure and Function in Rhodopsin: Measurement of the Rate of Metarhodopsin II Decay by Fluorescence Spectroscopy. The Journal of Biological Chemistry. 1995; 270: 5073–5076. https://doi.org/10.1074/jbc.270.10.5073 PMID: 7890614

32. Molnar T, Barabas P, Birnbaumer L, Punzo C, Kefalov V, Kriz D. Store-operated channels regulate intracellular calcium in mammalian rods. Journal of Physiology. 2012; 15: 3465–3481. https://doi.org/10.1113/jphysiol.2012.234641 PMID: 22674725

33. Nickell S, Park PSH, Baumeister W, Palczewski K. Three-dimensional architecture of murine rod outer segments determined by cryoelectron tomography. Journal of Cell Biology. 2007; 177: 917–925. https://doi.org/10.1083/jcb.200612010 PMID: 17535966

34. Williams DS, Hallett MA, Arikawa K. Association of myosin with the connecting cilium of rod photoreceptors. Journal of Cell Science. 1992; 190: 183–190.

35. Chen C, Jiang Y, Koutalos Y. Dynamic behavior of rod photoreceptor disks. Biophysical Journal. 2002; 83: 1403–1412. https://doi.org/10.1016/S0006-3495(02)73911-8 PMID: 12202366

36. Burns ME, Mendez A, Chen J, Baylor DA. Dynamics of cyclic GMP synthesis in retinal rods. Neuron. 2002; 36: 81–91. https://doi.org/10.1016/s0896-6273(02)00911-x PMID: 12367508

37. Gross OP, Burns ME. Control of rhodopsin' s active lifetime by arrestin-1 expression in mammalian rods. Journal of Neuroscience. 2010; 30: 3450–3457. https://doi.org/10.1523/JNEUROSCI.5391-09.2010 PMID: 20203204

38. Berry J, Frederiksen R, Yao Y, Nymark S, Chen J, Cornwall C. Effect of rhodopsin phosphorylation on dark adaptation in mouse rods. Journal of Neuroscience. 2016; 36: 6973–6987. https://doi.org/10.1523/JNEUROSCI.3544-15.2016 PMID: 27358455

39. Zuckerman R. Ionic analysis of photreceptor membrane currents. J Physiol. 1973; 235: 333–354. https://doi.org/10.1113/jphysiol.1973.sp010390 PMID: 4763993

Mechanosignaling in hippocampal neurons

(MS under Revision in *iScience*)

Mechanotransduction and mechanosignalling in hippocampal neurons

Fabio Falleroni[1], Simone Mortal[1], Yunzhen Li[1], Zhongye Ye[1], Dan Cojoc[2] & Vincent Torre[1,3]

[1]Neuroscience Area, International School for Advanced Studies (SISSA), 34136 Trieste, Italy
[2]Institute of Materials (IOM-CNR), Area Science Park, Basovizza, 34149, Trieste, Italy
[3]Center of Systems Medicine, Chinese Academy of Medical Sciences, Suzhou Institute of Systems Medicine, Suzhou Industrial Park, Suzhou, China
Corresponding Author: torre@sissa.it

Abstract:

Mechanosignalling among neurons of the central nervous system has not yet been firmly established, and its existence will modify our views of how neuronal networks operate. The force exerted by hippocampal filopodia and lamellopodia varies from 1 pN to tens of pN, therefore, we applied similar forces to hippocampal neurons. These forces evoked an increase in intracellular calcium mediated by calcium entry through mechanosensitive channels (MCSs)—Piezo1, Piezo2 and TRPC1—and the subsequent release of calcium from internal stores. Calcium activates calcium calmodulin kinase II (CAMKKII) and the small G protein RhoA, leading to a reorganization of the cytoskeleton within tens of seconds. These mechanical stimulations when applied to hippocampal Growth Cones (GCs) act as repellent signals inducing GC retraction and turning. Blockage of MCSs alters the formation of neuronal networks. These results show that mechanical signalling operates among hippocampal neurons and outline the molecular events underlying mechanosensitivity.

Introduction

The accepted view of the neuroscience community is that neurons interact with each other primarily through chemical and electrical signalling (*1*, *2*). It is well known, however, that there are also sensory neurons specialized to transduce mechanical stimuli that are the basis of hearing, mechanical sensation and pain (*3*, *4*). Recent investigations have shown that mechanosensitive channels (MSCs) are found almost ubiquitously in cells and tissues (*5*), suggesting that mechanosensitivity is widespread in the nervous system. We have previously shown that filopodia and lamellipodia of neurons of the central nervous system exert small forces in the range of 2-50 pN (*6*, *7*). It is important, therefore, to establish whether central nervous neurons are able to sense forces in the same range of amplitude and in this case mechanical signalling could play a major role in the development and operation of neuronal networks.

Recently, we developed an optical tweezer (OT) method (*8*) based on a tunable optical trap to apply forces in the 5-50-pN range and to measure the indentation produced in the cell and triggering changes in intracellular calcium ($[Ca^{2+}]_i$). Here, to verify whether neurons of the central nervous system respond to mechanical stimulations comparable to those exerted by filopodia and lamellipodia and we applied mechanical forces in the range of 10-50 pN to dissociated hippocampal neurons. We demonstrate that hippocampal neurons have exquisite mechanosensitivity and that their Growth Cones (GCs) can sense very small mechanical forces as low as 10-15 pN. Our results show that mechanical signalling operates in hippocampal neurons for very weak forces.

Results

We examined mechanotransduction in dissociated hippocampal neurons from P2-4 rats. Dissociated neurons were cultured for 1-2 days before the experiments.

Mechanical stimuli trigger an elevation of intracellular calcium

Hippocampal neurons were loaded with the calcium dye Fluo-4-AM (see Methods). If the fluorescence (F) emitted by a neuron was stable for 2-3 min, a polystyrene bead was trapped and positioned above the soma close to the initial segment of the largest neurite (Fig. 1A). Images of the emitted fluorescence F were acquired at 5 Hz for 3-5 min, and if F was stable, we proceeded with the mechanical stimulation. The trapped bead was lowered to touch the cell membrane, and a fixed number (from 1 to 6) of oscillations was then applied to the optical trap. These oscillations had an amplitude of 1 μm and a frequency of 1 Hz. In this way, we applied controlled mechanical stimulations during which both the force and the indentation were independently measured by the Quadrant Position Detector (QPD) (*8*). We monitored possible evoked $[Ca^{2+}]_i$ changes by analysing F, and we focused on the evoked fractional change of fluorescence $DF/F= (F_{stim}-F_{unstim})/F_{unstim}$), where F_{stim} is the fluorescence following mechanical stimulation and F_{unstim} is the fluorescence averaged in a time period of 1 sec before mechanical stimulation (Fig. 1B) in the ROI indicated by the light grey box (the second panel in Fig. 1B). Following a mechanical stimulation composed of 3 pulses with a maximum force of 45 pN and an indentation with a peak of 300 nm, we observed a fast increase in $[Ca^{2+}]_i$ in a highly localized manner near the site of the mechanical stimulation. Then, within some seconds, the initial fast component was followed by a second larger evoked change of DF/F with a mean duration of approximately 60 s (Fig. 1C and F).

Following a single mechanical stimulation, the change in $[Ca^{2+}]_i$ was composed only of the initial and fast increase in DF/F, referred to as the fast component (red trace in Fig. 1C, D and E).

We aligned the time course of the evoked changes in $[Ca^{2+}]_i$ from different neurons (different colours in Fig. 1G for one pulse, n=6 and in Fig. 1H for 3 pulses n=8) to the onset of mechanical stimulation (*8*). A closer inspection of these responses shows several important features of mechanotransduction: first, the onset of the initial component was fast and occurred within 1 or 2 frames, corresponding to 200-400 ms, following mechanical

stimulation regardless of whether 1 or 3 pulses were used; second, the amplitude of the initial component was remarkably similar in different neurons with a DF/F of approximately 0.01; third, the slow and delayed component developed with a variable delay from 1 up to 5 s; fourth, the amplitude of the delayed component was highly variable, in contrast with the amplitude and delay of the initial component, which were reproducible (Fig. 1G and H). The comparison of the DF/F averaged over different neurons for 1 (Fig. 1E) and 3 pulses (Fig. 1F) shows that the response to three mechanical pulses is often larger than 3 times the response to 1 pulse and that it has a more complex shape.

The time course of the second component was different in the soma and in nearby neurites (Fig. 1K), while the initial component was usually localized to the stimulation site. The second component had a different time course in the neurite and the soma (compare orange and light grey trace in Fig. 1K). The second component in the soma was larger and developed with a slower time course, reaching its peak in approximately 28 s, while in the neurite, the second component reached its peak in approximately 10 s.

The occurrence of the initial component was not observed when the bead oscillated in close proximity of the neuron without touching it, as revealed by the QPD. Therefore, the initial component is a genuine biological event and does not originate from optical interference caused by bead motion. These initial and delayed components were observed in 25 of 34 hippocampal neurons responding to mechanical stimulation varying from 10 to 50 pN.

The results shown in Fig. 1 were obtained with a stiffness K of 0.14 pN/nm corresponding to a maximum force of approximately 45 pN. To determine the lowest mechanical force able to activate a detectable response, we applied mechanical stimuli using a trap stiffness of 0.035 pN/nm equivalent to a maximum force of 12 pN referred to as LF (low force). In this case, three pulses evoked a change in $[Ca^{2+}]_i$ corresponding to a value of DF/F on the order of 0.007, but when the applied force was increased to 45 pN (HF), the fluorescence change DF/F increased to 0.028 (Fig. 2A-C).

Collected data from 6 experiments showed that the mean evoked value of DF/F for three pulses is 0.009 ± 0.003 (n=6) with the low force regime, whereas with higher forces, the evoked value of DF/F often increased more than 3 times with an average value of 0.28 ± 0.008 (n=7) (Fig. 3E). A similar result was already observed in NG-108 neuroblastoma cells (*8*). These results indicate that the threshold for evoking a detectable change in $[Ca^{2+}]_i$ is approximately 10 pN.

Having established mechanosensitivity of hippocampal neurons, we decided to verify whether blockage of MSCs eliminated or reduced the amplitude of the evoked calcium transients. Therefore, we used the MSC inhibitor GsMTx-4. GsMTx4 is a small peptide obtained from spider venom and has been shown to inhibit MSCs from both the Piezo and TRP families (*9*, *10*). This inhibitor is thought to act at the interface between the lipids in which the MSC is embedded (*9*), thereby reducing the effective magnitude of the mechanical stimulus acting on the MSC gate; thus, GsMTx4 is a gate modifier rather than an ion pore blocker. In 6 experiments following the observation of calcium transients evoked by mechanical stimuli, 10 µM GsMTx4 was added to the medium, and the mechanical stimulation was repeated (Fig. 2E). In the presence of GSMTx-4, the amplitude of evoked calcium transients was either significantly reduced (Fig. 2D) or abolished (3 experiments over 6). Therefore, we conclude that the mechanosensitivity of hippocampal neurons is mediated by MSCs in the plasma membrane.

We conclude that the initial component originates from calcium inflow through MSCs activated by mechanical stimulation. The second slower and larger calcium increase was more variable in size, duration and location and could be attributed to a subsequent release of calcium from internal stores.

Presence of mechanosensitive channels in hippocampal neurons

The results shown in Fig. 2D indicate that the fast and initial calcium increase is caused by the opening of MSCs in the plasma membrane, i.e., the activation of ionic channels among which there could be members of the TRP and/or Piezo families *(*11-13*)*. Therefore, we examined the presence of Piezo 1, Piezo 2 and TRPC1 in MSCs by immunohistochemistry in hippocampal cultures. Antibodies for Piezo 1, Piezo 2 and TRPC1 produced diffuse staining in the vast majority of neurons and glial cells both in the soma and in the neurites, and we could not detect any preference for specific kinds of neurites (Fig. 3A). Staining for the neuronal marker TuJ-1 shows that Piezo 1 is expressed primarily in neurons (Fig. 3B) and Piezo 2 in glial cells (Fig. 3C); indeed, TuJ-1 staining colocalizes with staining for Piezo 1 but not for Piezo 2 (Fig. 3B and C).

The molecular cascade initiated by mechanical stimuli

We then decided to identify the possible molecular cascade initiated by the entry of calcium ions through MSCs that eventually leads to these morphological changes. Several

molecular cascades initiated by an elevation of $[Ca^{2+}]_i$ involve the activation of CaMKII and of small GTPases as long-term potentiation in synapses and spines (*14–16*). CaMKII is one of the most abundant proteins in the postsynaptic domain (*17*) and plays a fundamental role in synaptic plasticity. When [Ca2+] increases, Ca2+ binds to calmodulin, and the activated Ca2+/calmodulin complex binds to a CaMKII subunit, causing a conformational change. The activation of two CaMKII subunits in contact is necessary for its full enzymatic activity. The Rho family GTPases, including Ras homologue (RhoA), cell division cycle 42 (Cdc42) and Ras-related C3 botulinum toxin substrate (Rac), are key players in regulating the actin cytoskeleton (*18, 19*). Both Cdc42 and RhoA activation is partially inhibited by inhibiting CaMKII signalling, suggesting that these molecules are activated by CaMKII (*15*, *20*).

The activation of CaMKII can be followed by monitoring its conformational changes by intramolecular FRET (*15*). Therefore, we used the intramolecular Camui-CR FRET sensor (Sup. Fig. 1A) (*21*) to verify the possible activation of CaMKII following mechanical stimulation. In this sensor, CAMKII was doubly tagged with green fluorescent protein (GFP, donor) and mRuby2 (acceptor), which are close when CAMKII is inactive; therefore, FRET occurs when CAMKII is not active. Following the activation of CaMKII, GFP and mRuby2 are separated, leading to a decrease in the FRET signal. Images of the donor and acceptor, i.e., of fluorescence emitted by GFP and mRuby2 (Fig. 4B), were captured 48 h post-transfection using a dual-sensor CCD. We measured the ratio of GFP/mRuby2 fluorescence, which was correlated with the activation levels of CAMKII (Fig. 4B). This ratio was stable before the mechanical stimulation, but a clear increase in D/A occurred with a delay of 1-5 s from the mechanical stimulation composed of three pulses with a stiffness of 0.14 pN/nm (Fig. 4C). The time course of the change in D/A was similar when it was computed on a large window or a smaller one centred on the soma, but the change of D/A was larger when computed on a smaller window indicated by the red box in the first panel of Fig. B. Averaged data from 4 experiments indicated that CAMKII was activated by mechanical stimulation (Fig. 4C) with a mean of 0.08 and with a latency varying from 0.5 to 2 s, as shown in Fig. 4D. We repeated similar FRET experiments to probe the possible activation of RhoA. In this case, we transfected hippocampal neurons with the Raichu-RhoA-CR sensor (*21*) **(**Fig. 4E and F*)*.

This intramolecular FRET probe is doubly tagged with green fluorescent protein (GFP, donor) attached to the PKN RhoA binding domain and mRuby2 (acceptor) (Fig. 4F) at-

tached to RhoA-GDP, and the activation of RhoA is signalled by an increase in FRET. Therefore, the activation of CAMKII is indicated by a decrease in FRET (increase in D/A), while the activation of RhoA is indicated by an increase in FRET (increase in A/D). From the images of the donor and acceptor, i.e., of fluorescence emitted by GFP and mRuby2 (Fig. 4E), we measured the ratio of fluorescence A/D (Fig. 4F) following mechanical stimulation using the same parameters in the CAMKII experiments. This ratio was stable before the mechanical stimulation, but we detected a clear increase in A/D with a mean of 0.04 and a delay of approximately 20 s (Fig. 4G, H).

To determine how the cytoskeleton reorganizes following mechanical stimulation, we transfected hippocampal neurons (inset of Sup. Fig. 2A) with fluorescently labelled actin (Sup. Fig. 2A). Fluorescent actin in hippocampal neurons is organized in arcs, some of which are collinear with the boundaries of the soma, and other arcs are perpendicular to the soma boundaries. We applied repetitive mechanical stimulation consisting of 6 pulses with a stiffness of 0.14 pN/nm to the region of the soma connected to the major neurite emerging from it (see the bead in the inset of Sup. Fig. 2A). Tens of seconds after the stimulation, the actin network started to reorganize, and arcs perpendicular to the soma boundary became more visible (Sup. Fig. 2B) and retracted. After approximately 70 s, the soma boundaries retracted, and in the following 2-4 min, the retraction was complete (Sup. Fig. 2B). A retraction of the actin network was observed in a total of 8 experiments in which we consistently observed an overall reorganization of the actin network in which actin arcs perpendicular to soma boundaries retracted first. We quantified the time course of actin reorganization by computing kymographs (Sup. Fig. 2C). Retraction varied from 0.2 to 1 μm.

Growth cones respond to mechanical stimulation

Having established the existence of mechanosensitivity of hippocampal neurons, we next investigated its role. It is possible that mechanosensitivity is involved in fine structural rearrangements and has a limited role in neuronal signalling. However, mechanical signalling may be complementary to chemical and electrical signalling and is a major component of neuronal processing. To test this possibility, we applied weak mechanical stimulation to GCs to verify whether hippocampal GCs respond not only to chemical signalling (*22*, *23*) but also to mechanical stimulation. We first searched for GCs that had filopodia actively moving and exploring the surrounding environment. GCs from hippocampal neurons moving vigorously were routinely found in the dish, and when a GC was active for at least 5

min, a polystyrene bead trapped in the equilibrium position of the laser beam of the OT was moved above it (Fig. 5A). Bright field images of the moving GC were acquired for at least 5 min at 3-5 Hz, and then, the bead was moved up and down, exerting a force varying between 10 and 30 pN with 3 or 6 mechanical stimuli. During mechanical stimulation, bright field images were acquired at 5 Hz for approximately 3 min (Fig. 5B), and the length and orientation of the filopodium were measured and quantified (Fig. 5C). In 5/31 experiments, the GC retracted and turned: turning initiates with a delay of approximately 20 and 10 s later, there is a small and transient retraction (Fig. 5E). Having avoided the site of mechanical stimulation, the filopodium continues to turn and elongate. In 11/31 experiments following mechanical stimulation, the GC turned away from the stimulation site with no detectable transient retraction, and in 7/31 experiments, the GC retracted; in the remaining 8 experiments, the mechanical stimulation was not effective. The collected data showed (Fig. 5D) that 3 repetitive stimuli evoke retraction/turning in approximately 50% of the stimulated GCs. In this case, the mean turning angle was 7.5 ± 2.2 (n=8). Six mechanical stimuli evoked turning in almost 80% of the GCs, and the mean turning angle was 28.0 ± 2.1 (Fig. 5D). We conclude that hippocampal neurons respond to mechanical stimuli similarly to what is observed when a chemorepellent agent is focally applied (*23*), i.e., exhibiting retraction/turning.

Mechanical signalling during the formation of neuronal networks

Having observed GC retraction and turning following mechanical stimulation, we decided to verify the existence of mechanical signalling among neurons. Hippocampal neurons sense mechanical stimulations corresponding to forces larger than 10-15 pN (Figs. 1-3). Therefore, we measured the force exerted by moving filopodia and lamellipodia by trapping a silica bead in front of the GC (Fig. 6A and C) and measuring the displacement (d) of the bead with the QPD (*8*): the force is then given by k*d, where k is the trap stiffness. In agreement with Amin et al. (2013), the force exerted by filopodia (Fig. 6B) varied between 1 and 12 pN with a mean value of 5.3 ± 1.2 pN (n=91), and the force exerted by lamellipodia (Fig. 6D) varied between 1 and 20 pN with a mean value of 8.7 ± 3.2 pN (n=175). Therefore, when a GC touches a nearby neuron, hippocampal filopodia exert a force larger than 10 pN in 5-10% of cases, while lamellipodia exert a force larger than 10 pN with a probability of approximately 30%. The duration of our mechanical stimulation was 1 s (Fig. 6E), while the force exerted by a lamellipodium had a much longer duration varying from 2 s up to 20 s (Fig. 6F), suggesting that a series of 3-6 mechanical stimuli,

such as those used in the experiments illustrated in Fig. 6, is a good mimic of the force exerted by a lamellipodium.

If mechanosignalling plays a role during the formation of neuronal networks, their connectivity will be altered when MCSs are blocked. To test this possibility, we cultured dissociated hippocampal neurons for seven days in control conditions (Fig. 6G) and in the presence of 10 μM GSMTX-4, and after fixation, we analysed the immunostaining for Actin (green), Tubulin (red) and DAPI (blue). When the localization of nuclei was considered by visualizing only the DAPI staining, visual inspection showed that following blockage of MSCs, neurons were more interspersed (compare bottom panels of Fig. 6G). For statistical confirmation, we performed a clustering analysis of the DAPI spots. We used the clustering method (*24*) in which cluster centres are identified as local density maxima that are far away from any points of higher density. We computed the histogram of the fraction of cells forming a cluster, and we verified that in control conditions, the mean fraction of clustered cells was 47%, which was higher than that in the presence of GSTMX-4, i.e., 30%. We also computed the cluster entropy (Fig 6H), and we found that in control conditions, this quantity was 0.96 but in the presence of the inhibitor of MSCs increased to 1.32 (two-sample Kolmogorov-Smirnov $p = 0.03$) indicating a lower degree of cluster formation. The plot of the relation between cluster entropy versus the fraction of clustered cells (Fig. 6I) shows that data from control conditions are statistically separated from those obtained in the presence of the inhibitor (two-sample Kolmogorov-Smirnov $p = 0.03$). Therefore, we conclude that the inhibition of MSCs significantly modified the neuronal connectivity, suggesting a role for mechanosensitivity in the formation of neuronal networks of hippocampal cultures.

Discussion

The present manuscript demonstrates mechanosensitivity in hippocampal neurons and outlines the biochemical cascade underlying it. Very weak mechanical stimuli act as repulsive stimuli, similar to chemical repulsive signalling (*23*), and hippocampal GCs turn away from the site of mechanical stimulation (Fig. 6). Our results showed that hippocampal neurons, in addition to the usual chemical and electrical signals, exchange mechanical signals.

Mechanosensitivity of hippocampal neurons

We previously demonstrated that neuroblastoma cells respond to mechanical stimulations as low as 8-10 pN, causing an indentation of the cellular membrane of 100-200 nm (*8*). The present manuscript shows that hippocampal neurons are sensitive to slightly higher mechanical forces. To evoke similar changes in $[Ca^{2+}]_{i,}$ we used a trap stiffness of k = 0.14 pN nm^{-1}, which was four times larger than that used with neuroblastoma cells (k=0.035 pN nm^{-1}). This difference could be attributed to the different thickness of the plasma membrane, which is approximately 6 and 8 nm in neuroblastoma and hippocampal neurons, respectively (*25*).

Similar to what was observed in neuroblastoma cells, repetitive mechanical stimulation (*8*) evoked a fast and small increase in $[Ca^{2+}]_i$ followed by a second larger and slower calcium wave. The early increase in $[Ca^{2+}]_i$ was localized, but the second wave invaded most of the soma of the neuron and developed in 10-20 s. Both in hippocampal neurons and neuroblastoma cells, $[Ca^{2+}]_i$ increases in two steps: there is a fast (within 200 ms from the mechanical stimulation) and small increase followed by a larger increase reaching its peak in 10-20 s. The initial increase in $[Ca^{2+}]_i$ is attributed to the opening of MSCs, and the second increase is attributed to a delayed release of Ca^{2+} from internal stores considering the dynamics of the event.

The biochemical cascade

The molecular mechanisms of mechanosensitivity and mechanotransduction are in the process of being elucidated, and two main mechanisms have emerged. Mechanosensing can occur in biological systems according to the so-called switch-like manner (*26*) in which the mechanical forces are transmitted with no delay to cellular structures inducing conformation changes in specific proteins. This pathway occurs through the activation receptors of the family of integrins and cadherins, which are coupled on one side to the extracellular matrix and to the surrounding environment and on the other side to the cytoskeleton and to the actomyosin complex (*27*).

The other mechanism underlying mechanotransduction occurs through the activation of MSCs. Since MSCs are mostly cation permeable, the concomitant entry of Ca2+ ions into the cell may be responsible for activating the transduction pathway (*28*, *29*). Indeed, mechanotransduction in hippocampal neurons, described here, seems to be mediated by

the activation of MSCs. By combining data obtained with the fluorescent calcium indicator Fluo-4, FRET measurements for the activation of CamKII and RhoA and experiments with fluorescently labelled actin, we have elucidated some steps of this biochemical cascade (Sup. Fig. 3).

When a weak mechanical force is applied, the neuron feels the combined effect of a force and of the concomitant indentation of its plasma membrane. As a consequence, MSCs open, and because these channels are permeable to Ca^{2+} ions, there is a fast increase in $[Ca^{2+}]_i$ occurring with a delay of 100-300 ms (orange line in Sup. Fig. 3). This localized calcium entry diffuses inside the neuron and is likely to activate several signalling pathways and an additional release of calcium from the intracellular store (see the delayed and slower rise of $[Ca^{2+}]_i$ in Figs. 1 and 2). The elevation of $[Ca^{2+}]_i$ activates CAMKII within 1-5 s (blue line in Sup. Fig. 3), which in turn activates the small GTPase RhoA (green line in Fig. 7) within 10-20 s. As a consequence of the activation of CamKII and RhoA and possibly of other proteins, the cytoskeleton reorganizes (pink box in Sup. Fig. 3) on a time scale ranging from tens of secs up to 2-4 min.

The biochemical cascade initiated by weak mechanical forces is similar to what has already been described in spines (*15*). In these experiments, a brief transient Ca^{2+} pulse causes a rapid activation of CaMKII within approximately 0.5 s, which decays in approximately 10 s. In hippocampal neurons, CAMKII activation occurs in a similar time window, but CAMKII remains activated for a longer time, presumably because of a longer elevation of $[Ca^{2+}]_i$. The activation of CAMKII terminates with a delay of 10-20 s following the return of $[Ca^{2+}]_i$ to its resting level (Fig. 7). In spines, long-term plasticity initiated by a rapid pulse of glutamate and the associated increase in [Ca2+]i activate RhoA and Cdc42 with a delay of some seconds (*16*), similar to what was observed in hippocampal neurons. Additionally, in spines and in other preparations, cytoskeletal reorganization occurs on a time scale of minutes (*30*).

Functional relevance

It is well established that mechanosensing and tissue stiffness control migration, axon growth during morphogenesis and neuronal development (*31*, *32*). These studies show that the MCS channel Piezo1 has a major role in ageing and development, and it is likely that the activation of Piezo1 initiates a biochemical cascade similar to that described here (Sup. Fig. 3).

Our results showed that neurons of the central nervous system, such as hippocampal neurons (*8*), are sensitive to mechanical forces in the range of forces exerted by hippocampal filopodia and lamellipodia (Fig. 6). Therefore, in neuronal networks, in addition to the usual electrical and chemical signalling, mechanical signalling is present. Light mechanical stimulation on GCs acts as repulsive stimuli inducing turning and retraction (Fig. 5), and when a GC encounters the soma of another neuron, it is likely to evoke an increase in [Ca2+]i. We propose that the formation of neuronal networks requires the processing of concomitant mechanical, chemical and electrical signals, giving rise to a complex mechanical computation (*33*), as suggested by the altered neuronal connectivity when MCSs are inhibited (Fig. 6). GCs located at the tip of neurites explore the environment and decode all the encountered mechanical, electrical and chemical clues and then "decide/compute" what to do. Mechanical computation represents the functional understanding of mechanosensitivity and mechanotransduction described in the present manuscript and aims to unravel the strategy used by filopodia and lamellipodia during their exploration and navigation and the mechanical problems that neurons need to solve during development and ageing and in the adult brain.

Understanding the molecular and biophysical mechanism of how cells process concomitant mechanical and chemical signals and regulate their response will clarify how cells change shape and control their migratory behaviour. Therefore, mechanical signalling among cells is important and ubiquitous but still needs to be better clarified.

Materials and Methods

Cell culture

Wistar rats at postnatal days 1 to 2 (P1–P2) were sacrificed by decapitation after anaesthesia with CO_2 in accordance with the Italian Animal Welfare Act. The Ethics Committee of the International School for Advanced Studies (SISSA) approved the protocol. After decapitation, the hippocampus of P1-P2 rats was dissected, cut into pieces and washed twice with the dissection medium. Enzymatic dissociation was performed by treatment of the slices with 5 mg/ml trypsin (Sigma-Aldrich) and 0.75 mg/ml DNase I (Sigma-Aldrich) in digestion medium (5 min, room temperature). Then, trypsin was neutralized by 1 mg/ml trypsin inhibitor (Sigma-Aldrich) in the dissection medium for 10 min on ice. After a wash in the dissection medium, mechanical dissociation was performed in the same dissection medium with 0.6 mg/ml DNase I by approximately 50 passages through a Gilson P1000 tip. The cell suspension was then centrifuged at 800 rpm for 5 min, and the pellet was resuspended in the culture medium. Finally, hippocampal neurons were plated on coverslips coated with 50 µg/ml poly-L-ornithine (Sigma-Aldrich). Hippocampal neuronal cultures were incubated (5% CO_2, 37 °C) for 24-48 h in neurobasal medium (Thermo Fisher) and with B27 supplement (Thermo Fisher).

Calcium experiment

The cells were loaded with the cell-permeable calcium dye Fluo4-AM (Life Technologies) as described in Falleroni et al., 2018. Briefly, the cells were incubated with 20% Fluo4-AM and Pluronic F-127 in Krebs-Ringer's solution containing 119 mM NaCl, 2.5 mM KCl, 1 mM NaH_2PO_4, 2.5 mM $CaCl_2$, 1.3 mM $MgCl_2$, 11 mM D-glucose, 1.3 mM $MgCl_2$, and 20 mM HEPES (pH 7.4) at 37 °C for 30 min. After incubation, the cultures were washed and then transferred to the stage of an Olympus IX-81 inverted microscope. The experiments were performed at 37 °C, and images were acquired using Micromanager software with an ApoFluor 60x/1.2 NA objective at a sampling rate of 5 Hz. Imaging experiments were conducted with Krebs-Ringer's solution (pH 7.4).

Optical manipulation

To mechanically stimulate the cell, we used a custom-built optical tweezer combined with an inverted microscope described in detail in (*8*). Briefly, we used a polystyrene bead with

a 3.5-µm diameter (G. Kisker Biotech Germany) optically trapped in a controllable oscillatory optical trap (OOT). We used an infrared (IR) laser at 1064 nm for trapping (IPG Laser Germany). The axial position of the trap could be adjusted within a range of 0 – 20 µm using a custom designed two-lens system composed of a focus tunable lens (EL-10-30-NIR-LD, Optotune AG, Switzerland), of which the focal length can be varied by computer control (LabVIEW code).

Force and indentation measurement

A complete description of the force and indentation measurements is found in (*8*). In the BFI method, the interference of the laser light scattered by the bead in the optical trap allows for the bead to be used as a position probe and, through the assumption of a parabolic potential for the optical trap, a force probe (17). Thus, the displacement of the bead in the trap was followed from the displacement of the interference pattern on the QPD, which could be measured at frequencies of tens of kHz.

Mechanical stimulation and calcium imaging

All components (FTL, CCD camera and QPD) were synchronised and controlled using custom software written in LabVIEW as well as time-lapse control of the LED system. Data from the FTL and the PD were digitized using an acquisition board (DAQ) from National Instruments.

Immunofluorescence analysis

For the immunofluorescence analysis of Piezo1, Piezo2 and TRPC1, the cells were fixed with 4% paraformaldehyde for 10 min, permeabilized with 0.1% Triton™ X-100 for 10 min, blocked with 1% BSA for 30 min and labelled with mouse primary antibody (1:250 dilution) for 3 h at room temperature. Goat anti-rabbit secondary antibody, P conjugate, was used at a concentration of µg/mL in phosphate buffered saline containing 0.2% BSA for 1 h at room temperature. Nuclei were stained with DAPI. The neuronal component was stained with Tuji-1 (Product # A12379, 1:300) (Panel c: red). The images were captured at 40X magnification.

FRET measurements

Hippocampal neurons were seeded on glass coverslips, coated with polyornithine and transfected 24 h later with the intramolecular CAMKII/RhoA FRET sensor using Lipofectamine 2000. The pcDNA3-Camui-CR (Addgene plasmid # 40256) and pCAGGS-Raichu-RhoA-CR (Addgene plasmid # 40258) were purchased from Addgene.

Actin transfection

The 1 DIV hippocampal neurons were transfected with LifeAct plasmid using Lipofectamine 2000 following the manufacturer's protocol.

Data and statistical analysis

For calcium experiments, the DF/F values were obtained through custom MATLAB (The MathWorks, Natick, MA, USA) code and the ImageJ software v1.6 (National Institutes of Health, Bethesda, MD, USA). All results are presented as mean ± SD, and significant differences were determined using a *t* test with $p < 0.05$ (GraphPad Prism 7, GraphPad software, San Diego, CA, USA).

Bibliography

1. Principles of Neural Science, Fifth Edition | AccessNeurology | McGraw-Hill Medical, (available at https://neurology.mhmedical.com/book.aspx?bookID=1049).

2. Neuroscience - Dale Purves; George J. Augustine; David Fitzpatrick; William C. Hall; Anthony-Samuel LaMantia; Richard D. Mooney; Michael L. Platt; Leonard E. White - Oxford University Press, (available at https://global.oup.com/ushe/product/neuroscience-9781605353807?q=9781605353807&lang=en&cc=us).

3. D. J. Müller, J. Helenius, D. Alsteens, Y. F. Dufrêne, Force probing surfaces of living cells to molecular resolution. *Nature Chemical Biology*. **5**, 383–390 (2009).

4. E. A. Lumpkin, M. J. Caterina, Mechanisms of sensory transduction in the skin. *Nature*. **445**, 858–865 (2007).

5. P. Delmas, J. Hao, L. Rodat-Despoix, Molecular mechanisms of mechanotransduction in mammalian sensory neurons. *Nature Reviews Neuroscience*. **12**, 139–153 (2011).

6. D. Cojoc, F. Difato, E. Ferrari, R. B. Shahapure, J. Laishram, M. Righi, E. M. D. Fabrizio, V. Torre, Properties of the Force Exerted by Filopodia and Lamellipodia and the Involvement of Cytoskeletal Components. *PLOS ONE*. **2**, e1072 (2007).

7. L. Amin, E. Ercolini, J. Ban, V. Torre, Comparison of the Force Exerted by Hippocampal and DRG Growth Cones. *PLOS ONE*. **8**, e73025 (2013).

8. F. Falleroni, V. Torre, D. Cojoc, Cell Mechanotransduction With Piconewton Forces Applied by Optical Tweezers. *Front. Cell. Neurosci.* **12** (2018), doi:10.3389/fncel.2018.00130.

9. R. Gnanasambandam, C. Ghatak, A. Yasmann, K. Nishizawa, F. Sachs, A. S. Ladokhin, S. I. Sukharev, T. M. Suchyna, GsMTx4: Mechanism of Inhibiting Mechanosensitive Ion Channels. *Biophysical Journal*. **112**, 31–45 (2017).

10. C. Bae, F. Sachs, P. A. Gottlieb, The Mechanosensitive Ion Channel Piezo1 Is Inhibited by the Peptide GsMTx4. *Biochemistry*. **50**, 6295–6300 (2011).

11. G. Barritt, G. Rychkov, TRPs as mechanosensitive channels. *Nature Cell Biology*. **7**, 105–107 (2005).

12. B. Coste, B. Xiao, J. S. Santos, R. Syeda, J. Grandl, K. S. Spencer, S. E. Kim, M. Schmidt, J. Mathur, A. E. Dubin, M. Montal, A. Patapoutian, Piezo proteins are pore-forming subunits of mechanically activated channels. *Nature*. **483**, 176–181 (2012).

13. A. H. Lewis, J. Grandl, Mechanical sensitivity of Piezo1 ion channels can be tuned by cellular membrane tension. *eLife*. **4**, e12088 (2015).

14. B. Xu, G. Song, Y. Ju, X. Li, Y. Song, S. Watanabe, RhoA/ROCK, cytoskeletal dynamics, and focal adhesion kinase are required for mechanical stretch-induced tenogenic differentiation of human mesenchymal stem cells. *Journal of Cellular Physiology*. **227**, 2722–2729 (2012).

15. H. Murakoshi, H. Wang, R. Yasuda, Local, persistent activation of Rho GTPases during plasticity of single dendritic spines. *Nature*. **472**, 100–104 (2011).

16. N. G. Hedrick, R. Yasuda, Regulation of Rho GTPase proteins during spine structural plasticity for the control of local dendritic plasticity. *Current Opinion in Neurobiology*. **45**, 193–201 (2017).

17. J. W. Hell, CaMKII: Claiming Center Stage in Postsynaptic Function and Organization. *Neuron*. **81**, 249–265 (2014).

18. S.-T. Sit, E. Manser, Rho GTPases and their role in organizing the actin cytoskeleton. *J Cell Sci*. **124**, 679–683 (2011).

19. S. Etienne-Manneville, A. Hall, Rho GTPases in cell biology. *Nature*. **420**, 629–635 (2002).

20. H. J. Haws, M. A. McNeil, M. D. H. Hansen, Control of cell mechanics by RhoA and calcium fluxes during epithelial scattering. *Tissue Barriers*. **4**, e1187326 (2016).

21. A. J. Lam, F. St-Pierre, Y. Gong, J. D. Marshall, P. J. Cranfill, M. A. Baird, M. R. McKeown, J. Wiedenmann, M. W. Davidson, M. J. Schnitzer, R. Y. Tsien, M. Z. Lin, Improving FRET dynamic range with bright green and red fluorescent proteins. *Nature Methods*. **9**, 1005–1012 (2012).

22. E. A. Vitriol, J. Q. Zheng, Growth Cone Travel in Space and Time: the Cellular Ensemble of Cytoskeleton, Adhesion, and Membrane. *Neuron*. **73**, 1068–1081 (2012).

23. G. Pinato, D. Cojoc, L. T. Lien, A. Ansuini, J. Ban, E. D'Este, V. Torre, Less than 5 Netrin-1 molecules initiate attraction but 200 Sema3A molecules are necessary for repulsion. *Scientific Reports*. **2**, 675 (2012).

24. A. Rodriguez, A. Laio, Clustering by fast search and find of density peaks. *Science*. **344**, 1492–1496 (2014).

25. N. Galvanetto, Single-cell unroofing: probing topology and nanomechanics of native membranes. *Biochimica et Biophysica Acta (BBA) - Biomembranes*. **1860**, 2532–2538 (2018).

26. B. D. Hoffman, C. Grashoff, M. A. Schwartz, Dynamic molecular processes mediate cellular mechanotransduction. *Nature*. **475**, 316–323 (2011).

27. J. S. Park, C. J. Burckhardt, R. Lazcano, L. M. Solis, T. Isogai, L. Li, C. S. Chen, B. Gao, J. D. Minna, R. Bachoo, R. J. DeBerardinis, G. Danuser, Mechanical regulation of glycolysis via cytoskeleton architecture. *Nature*. **578**, 621–626 (2020).

28. N. Murata, S. Ito, K. Furuya, N. Takahara, K. Naruse, H. Aso, M. Kondo, M. Sokabe, Y. Hasegawa, Ca2+ influx and ATP release mediated by mechanical stretch in human lung fibroblasts. *Biochemical and Biophysical Research Communications*. **453**, 101–105 (2014).

29. S.-K. Han, W. Wouters, A. Clark, W. Herzog, Mechanically induced calcium signaling in chondrocytes in situ. *Journal of Orthopaedic Research*. **30**, 475–481 (2012).

30. Y. Nakahata, R. Yasuda, Plasticity of Spine Structure: Local Signaling, Translation and Cytoskeletal Reorganization. *Front. Synaptic Neurosci.* **10** (2018), doi:10.3389/fnsyn.2018.00029.

31. D. E. Koser, A. J. Thompson, S. K. Foster, A. Dwivedy, E. K. Pillai, G. K. Sheridan, H. Svoboda, M. Viana, L. da F. Costa, J. Guck, C. E. Holt, K. Franze, Mechanosensing is critical for axon growth in the developing brain. *Nature Neuroscience*. **19**, 1592–1598 (2016).

32. E. H. Barriga, K. Franze, G. Charras, R. Mayor, Tissue stiffening coordinates morphogenesis by triggering collective cell migration in vivo. *Nature*. **554**, 523–527 (2018).

33. J. Laishram, D. Avossa, R. Shahapure, V. Torre, Mechanical computation in neurons. *Developmental Neurobiology*. **69**, 731–751 (2009).

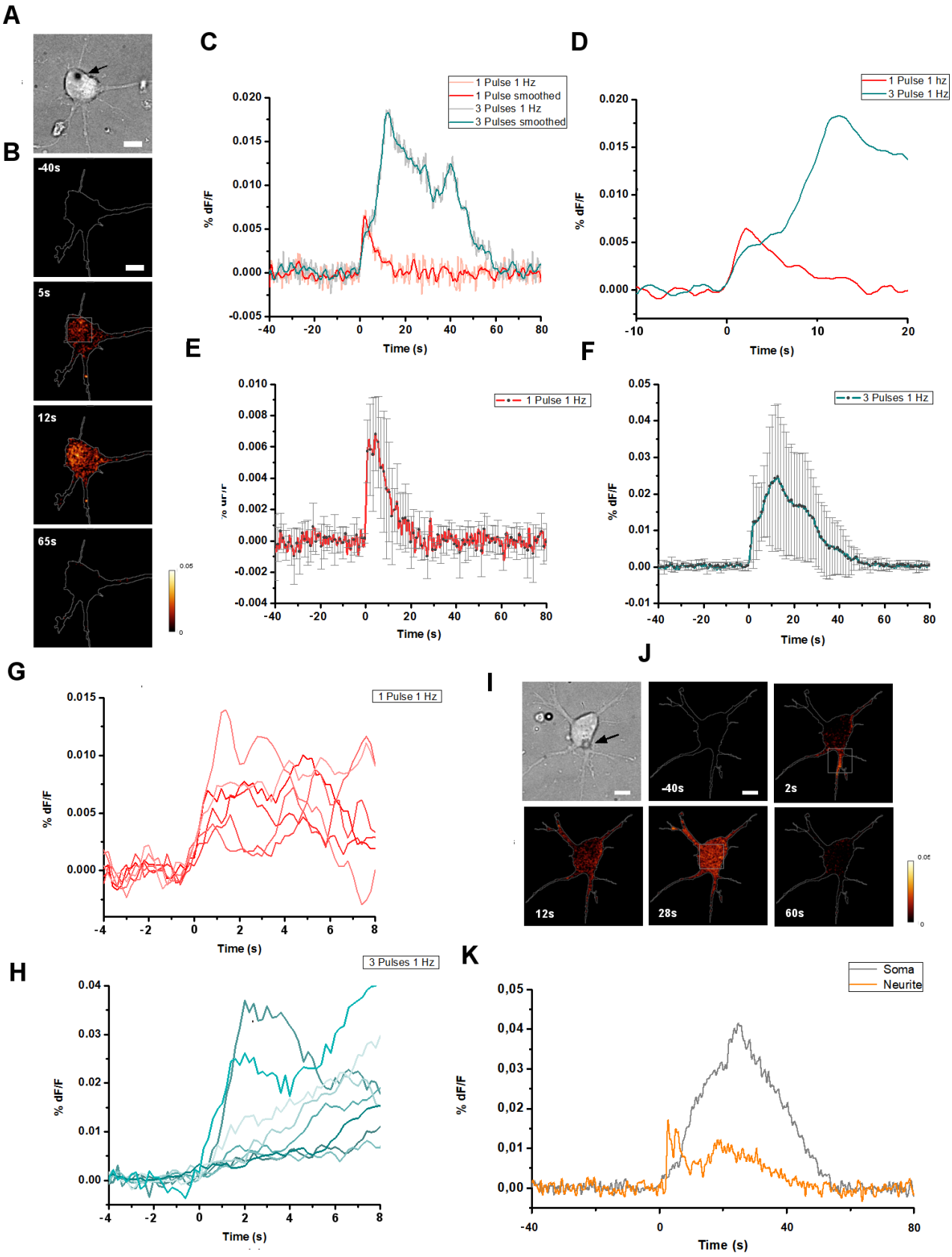

Figure 1. Calcium signals (DF/F) evoked by mechanical stimulation. *A: Bright field image of hippocampal neurons with a trapped bead above the soma. B: Time course of calcium transients evoked by three mechanical stimulations. C: Comparison of calcium transients evoked by one (red) and three (cyan) mechanical stimulations. The smoother lines represent running averages taken over a 2 sec window. D: Enlargement of the*

smoothed traces in E for t= -10 s:20 s. E: Average and standard deviation of calcium signals obtained with one mechanical pulse (n=6). F: As in I but for three pulses (n=10). G: Superimposed calcium signals obtained with one mechanical pulse. H: As in G but for three mechanical stimulations. I and J: As in A and B but for one experiment showing a calcium signal, both in the soma and neurite. K: Time course of calcium signals computed from the two ROIs shown in L. Scale bar 5 µm.

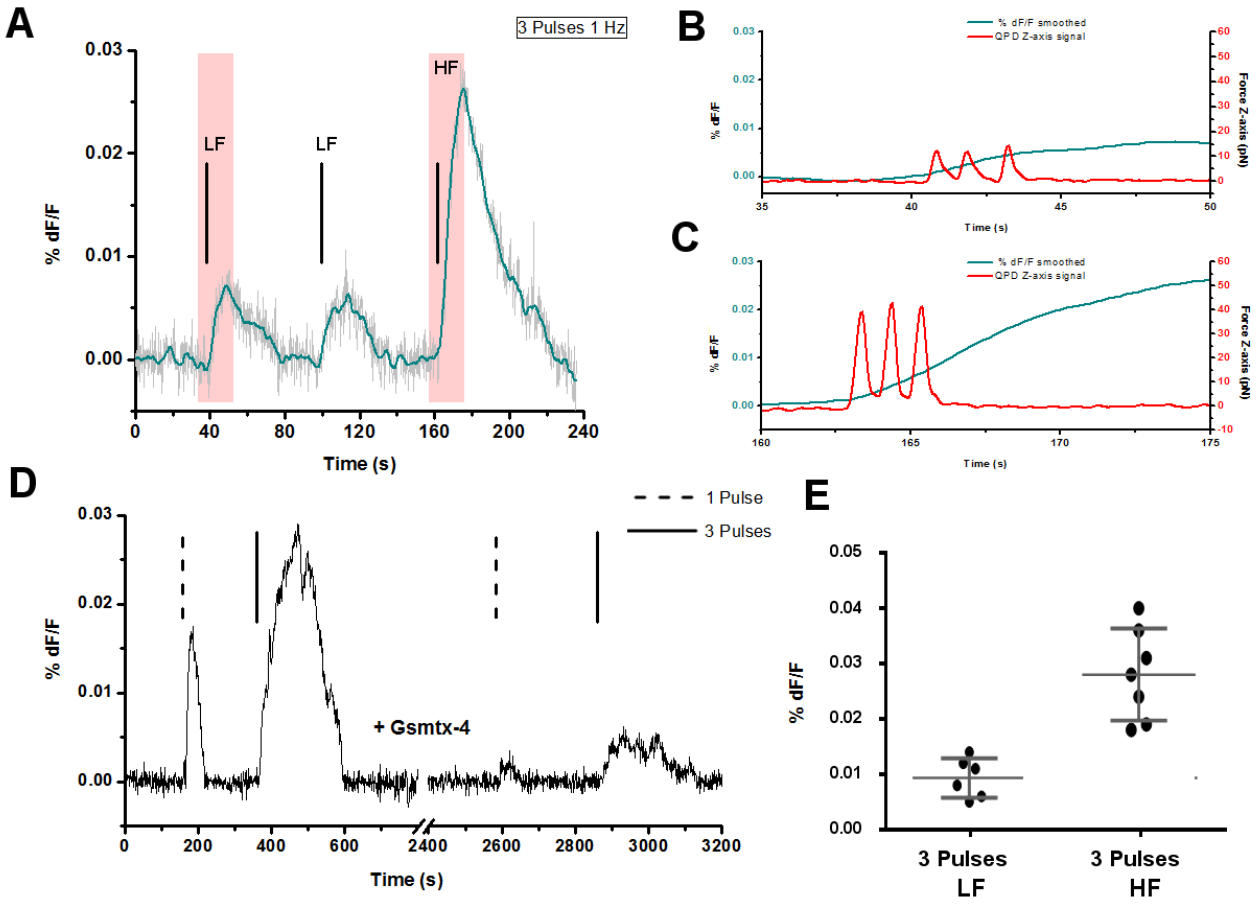

Figure 2. Calcium signals evoked by mechanical stimulations with different strengths. *A: Time course of the evoked calcium signals by mechanical stimulation with a low force (LF) equivalent to 10.5 pN and a high force (HF) equivalent to 42 pN. B and C: Enlargement of the traces in A (red light boxes) showing the time course of the mechanical stimulations and of the induced calcium signals. D: Effect of Gsmtx4 (10 µM) on mechanically induced calcium signals. The broken line in the x-axis indicates the time of drug application (2400 s). E: Statistics of calcium transient D/F for 3 pulses with an indentation of approximately 300 nm and a trap stiffness of k = 0.035 pN nm^{-1} (low force) and k = 0.14 pN nm^{-1} (high force).*

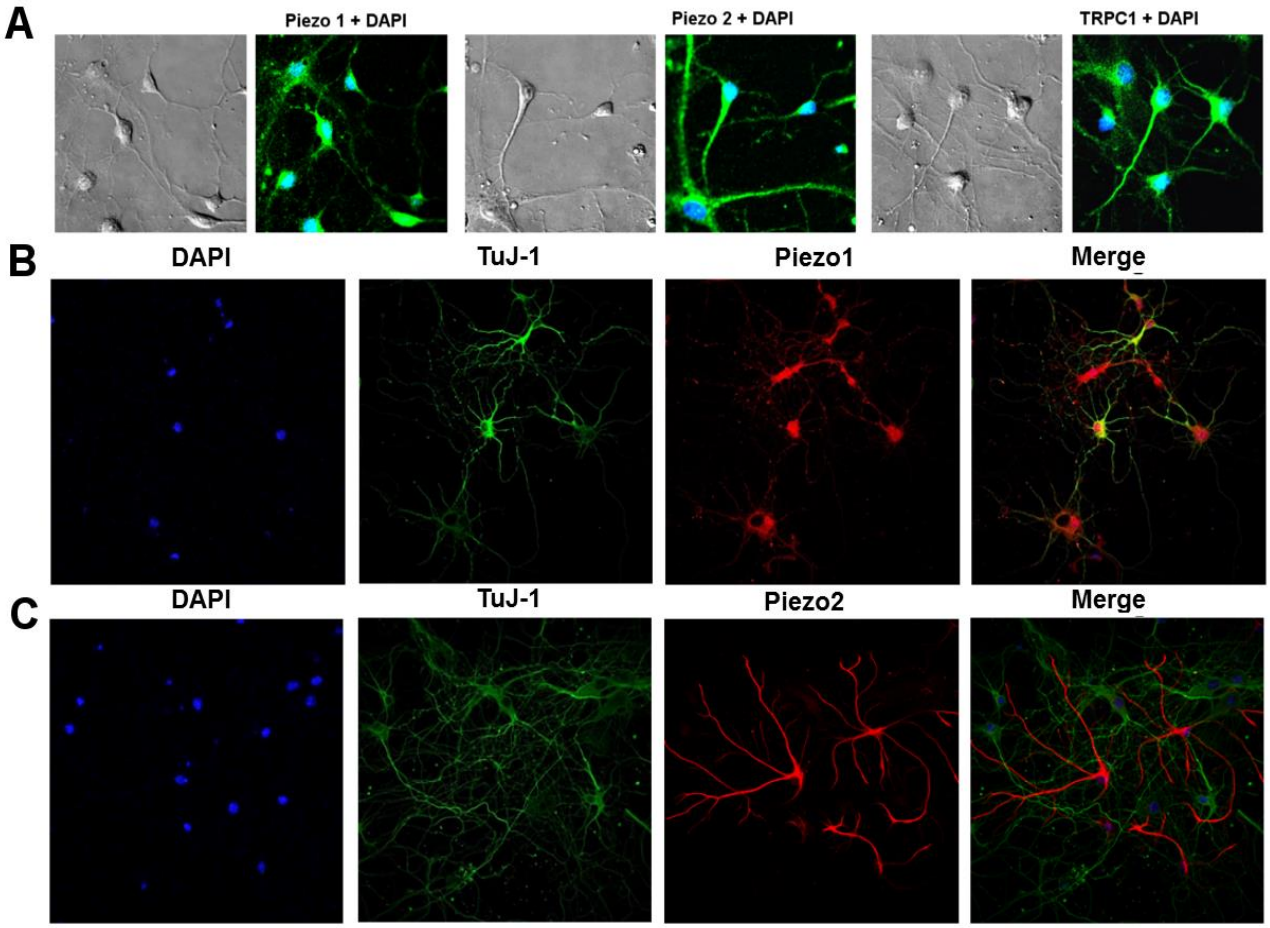

Figure 3. Expression of mechanosensitive channels in hippocampal neuronal cultures. *A: Neurons stained at 2 DIV with Piezo 1, Piezo 2 and TRPC1 antibodies (green) and DAPI (blue). The Piezo1 channels are expressed both at the tip of the neuronal process (red arrow) and soma (white arrow). B: Immunofluorescence images showing the neuronal markers TuJ-1, Piezo 1, and DAPI and the merged signals. The staining of Piezo 1 colocalizes with TuJ-1. C: As in B but for Piezo 2. Piezo 2 is mainly expressed in glial cells and to a lesser extent in neurons.*

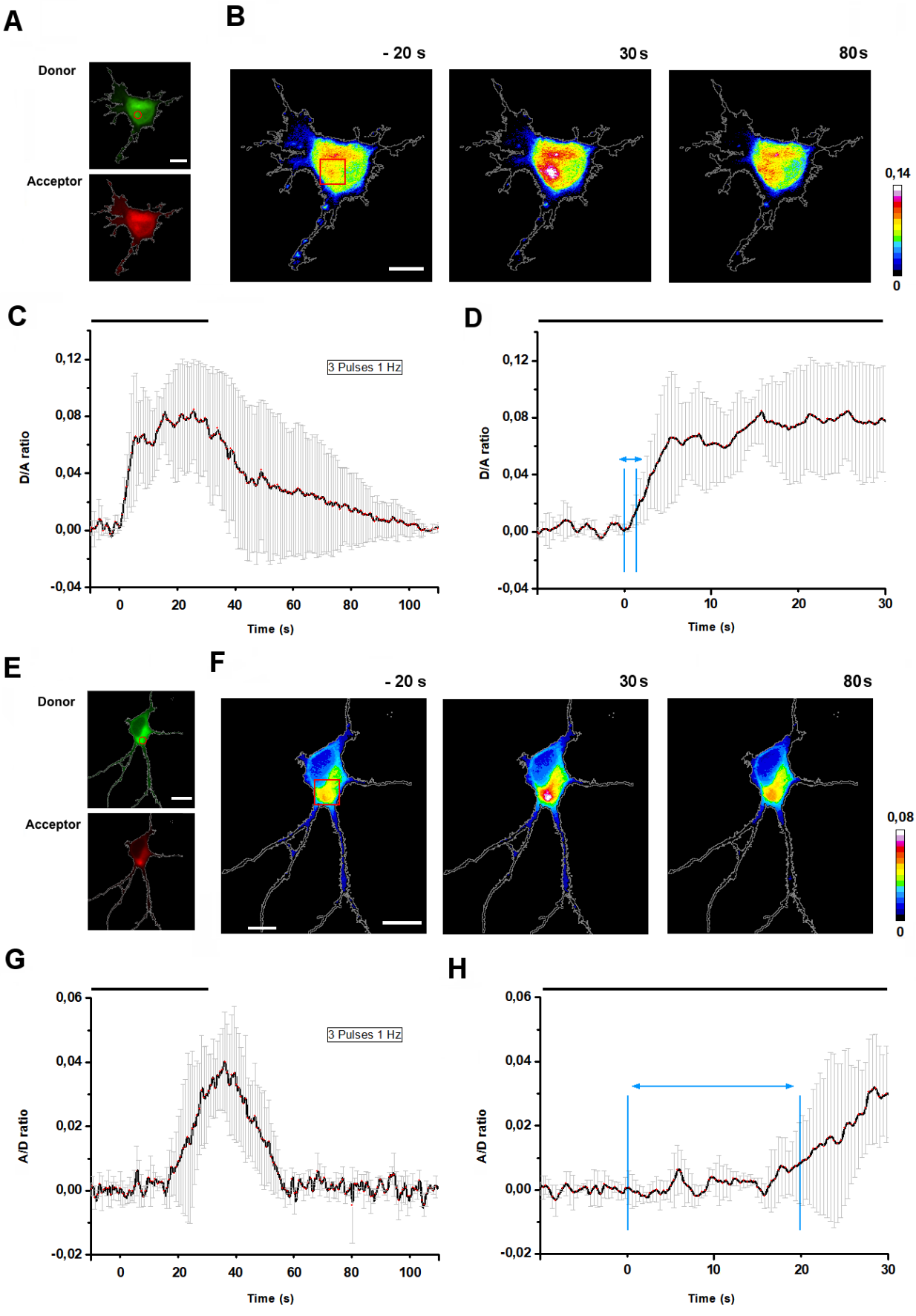
A
Donor
Acceptor
B
- 20 s
30 s
80 s
0,14
0
C
3 Pulses 1 Hz
D/A ratio
0,12
0,08
0,04
0,00
-0,04
0
20
40
60
80
100
Time (s)
D
D/A ratio
0,12
0,08
0,04
0,00
-0,04
0
10
20
30
Time (s)
E
Donor
Acceptor
F
- 20 s
30 s
80 s
0,08
0
G
3 Pulses 1 Hz
A/D ratio
0,06
0,04
0,02
0,00
-0,02
0
20
40
60
80
100
Time (s)
H
A/D ratio
0,06
0,04
0,02
0,00
-0,02
0
10
20
30
Time (s)

Figure 4. The activation of CAMKII and RhoA by mechanical stimulation*. A: Fluorescence images of the donor and acceptor used for the FRET measurement for the detection of CAMKII activation. Scale bar, 10 µm. B: Ratiometric images (D/A ratio) before and after (30 and 80 s) mechanical stimulation. The red square is the ROI used to compute the FRET signal. Scale bar, 10 µm. C: Time course of the FRET signal for the activation of CAMKII averaged from 4 experiments. The time zero indicates the mechanical stimulation (three pulses with high stiffness); D: Enlargement of C for t = -10 s : 30 s. E: Fluorescence images of the donor and acceptor used for the FRET measurement for the detection of RhoA activation. Scale bar, 10 µm. F: Ratiometric images (A/D ratio) before and after (30 and 80 s) stimulation with one ROI used to compute the FRET signal. Scale bar, 10 µm. G: Statistical analysis of RhoA activation (n=4). H: As in D but for RhoA experiments (n=4). Time zero indicates OT stimulation.*

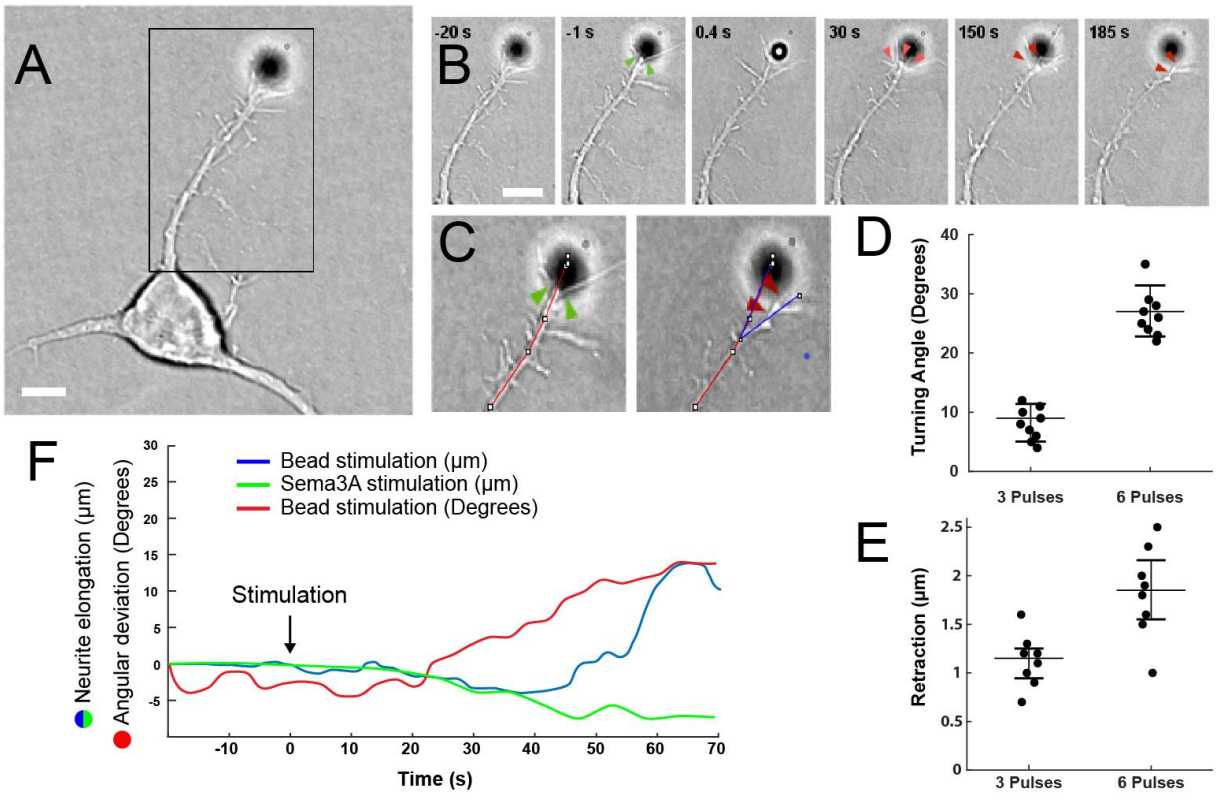

Figure 5. Response of hippocampal GC to mechanical stimulation*. A: Bright field image of hippocampal neurons and a trapped bead near the GC. Scale bar, 10 µm. B: Time course of GC response: before (green arrow) and after (red arrow) mechanical stress retraction of GCs. Scale bar, 5 µm. C: Zoom of the GC before and after the termination of the mechanical stimulation. The angle between the red and blue segments is the turning angle. D: Relation between the amplitude of the turning angle and the number of applied pulses. The turning angles were determined by measuring the angle between the GC's initial trajectory and the final trajectory of that GC after mechanical stimulation. E: Relationship between the retraction of GC and the number of applied pulses. F: Tracking of the GC over time; blue indicates neurite elongation before and after bead stimulation (black arrow); green indicates neurite elongation before and after Sema3A administration (black arrow); and red indicates angular deviation before and after bead stimulation (black arrow). The data for the effect of Sema3A administration were redrawn from Pinato* et al. *(23)*.

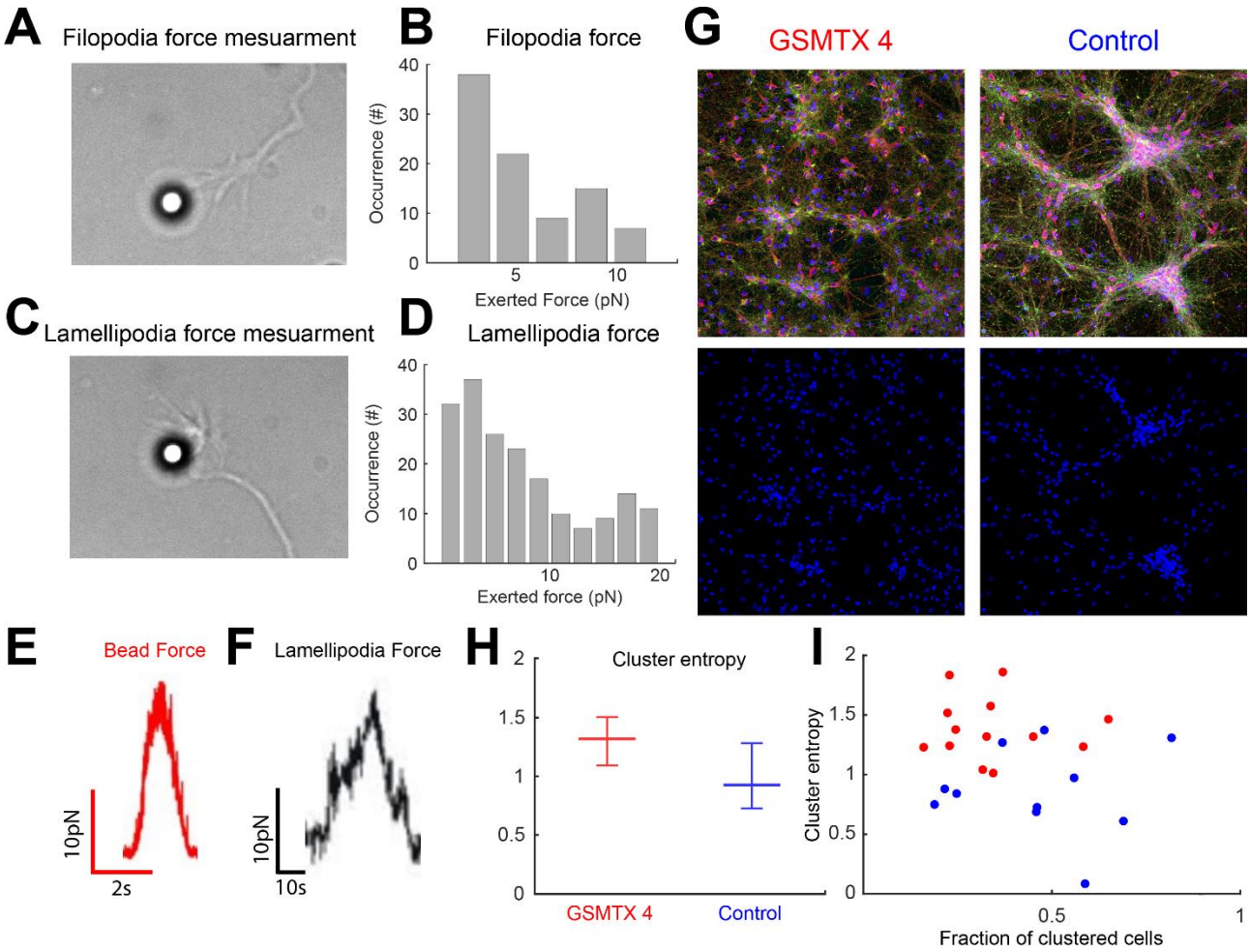

Figure 6. Forces during the formation of neuronal networks*. A: Bright field image of a hippocampal filopodium colliding with a trapped bead. B: Distribution of the force exerted by filopodia. Data from 27 experiments. C: Bright field image of a hippocampal lamellipodium colliding with a trapped bead. D: Distribution of the force exerted by lamellipodia. Data from 35 experiments. E: Example of the force exerted by the bead on a hippocampal lamellipodium. F: Example of the force exerted by the lamellipodium on the bead. G: Immunostaining of hippocampal culture 7 days in vitro, with GsMtx-4 and in control condition. Actin is in green, tubulin in red and DAPI in blue. H) Cluster entropy computed on DAPI staining of neurons 7 days in vitro (bottom panels of Fig. 6G). I: Relationship between cluster entropy versus the fraction of clustered cells.*

Ca^{2+} flares & Cl^{-} flux in GBM mechanosensitivity and replication

(MS under Preparation)

Calcium Flares and Chloride Flux in Glioblastoma Mechanosensitivity and Replication

Yunzhen Li[*1], Andres Hernandes*[*1],Cesar Trivino*[*1],Simone Mortal[1], Kevin Gonzalez[1], Renza Spelat[1], Vincent Torre[1], Anna Menini*[+]

[1] *International School for Advanced Studies (SISSA), via Bonomea 265, Trieste 34136, , Italy.*

**equally contributed*
+ corresponding author: email: menini@sissa.it

Abstract

Replication of glioblastoma (GBM) cells in the brain of patients is the main cause of their death. We combined optical tweezer, multi-channel fluorescence imaging for both calcium and chloride ions, live cell imaging, electrophysiology and histochemistry. Firstly, we characterized spontaneous Ca^{2+} flares and their coupling with the chloride flux. Secondly, we studied these events in normal flat GBM cells not undergoing mitosis and in mitotic round GBM cells. Mechanical stimulations with OT with forces in the 10-50 pN range evoked either local calcium transients or increased the frequency and amplitude of calcium flares. The simultaneous multichannel imaging for both calcium and chloride dyes showed that large spontaneous global calcium flares are coupled with chloride signals. These chloride signals, however, were - unexpectedly - localized. In round cells presumably undergoing mitosis, large calcium flares could not be detected during metaphase/anaphase transition, but large calcium flares were frequently seen during telophase and cytokinesis. Histochemistry analysis show the existence on GBM membranes of TMEM16A, TMEM16B and VRAC Cl^- channels. These results provided a link between GBM replication, Ca^{2+} flares and Cl^- fluxes, setting the basis for a better understanding of GBM replication and blockage.

Introduction

Replication of cells and in particular of high grade glioma, usually referred as glioblastoma (GBM), is a complex phenomenon at the basis of life and of death in patients suffering of brain cancers composed by GBM. Replication and cell cycle is controlled by events occurring primarily in the nucleus associated to duplication and rearrangements of chromosomes ***(N Prevarskaya et al. 2010 Trends Mol Med)***.

GBM has a high proliferative capacity. Genetic changes in the growth signaling that impair tightly regulated normal cell homeostasis has been widely accepted as the fundamental reason, leading to transformation of normal cells into malignant type with uncontrolled proliferative potential ***(N Prevarskaya et al. 2010 Trends Mol Med)***. In this respect, ion channels were considered to play a pivotal role in tumor biology and are involved in regulation of tumor cell characteristics like uncontrolled growth ***(VA Cuddapah et al. 2011 Am J Physiol Cell Physiol)***, while it suggested abnormal calcium signals and dynamics plays an important role in the uncontrolled growth ***(GR Monteith et al. 2017 Nat Rev Cancer)***. On the other respect, several lines of evidence suggest that chloride (Cl^-) and potassium (K^+) channels have a major role in cell volume shrinking and swelling, fundamental steps during mitosis and replication***(CW Habela et al. 2007 Cell Cycle)***.

We have previously shown the existence of calcium flares in GBM ***(X Li et al. 2020 J Cell Sci)***, we hypothesized that calcium flares and Cl^- channels could play an important role during GBM migration and mitosis. In this thesis, I am trying to investigate the calcium signals and dynamics related to mechanosensitivity and its coupling with the chloride flux in either normal flat and mitotic round GBM cells and then discuss roles of the calcium flares and chloride flux in GBM replication, by using multi-channel imaging of Calcium and chloride, ratiometric calcium imaging, and additionally, electrophysiological methods.

My data show that pN forces can either evoke local calcium transients or increase of the frequency and amplitude of calcium flares in normal flat cells, while global calcium flares can last stably for at least one hour without significantly changing the morphology of the cell, and more importantly are able to activate chloride fluxes. In round cells undergoing mitosis, I could not detect clear calcium flares at the initial phase before the cell divides into two, but I was able to detect calcium flares at the final steps end of mitosis, i.e. during telophase and

cytokinesis. These calcium flares are further increased by the Piezo 1 agonist Yoda 1, increasing also the associated chloride influxes.

Results

We used U87 cell lines as a suitable model of GBM and we checked the obtain results with glioblastoma, i.e. Grade IV from patients. In fact during surgery aiming to remove brain tumors, the excised tissue was cultured and Glioma Stem Cells (GSC) and Glioma Associated Stem Cells (GASC) were frozen. GSC and GASC from operated patients were prepared and cultured for imaging and electrophysiological experiments ***(L Andolfi et al. 2014 PLoS One, E Bourkoula et al. 2014 Stem Cells)***.

Spontaneous Ca^{2+} flares and during mitosis

We loaded U87 MG GBM with the calcium fluorescent dye of high sensitivity, Fluo-4 or Oregon Green 488 BAPTA-1,AM (OGB-1), we looked for calcium flares or oscillations in flat cells, i.e. in GBM (See Fig.1A). GBM during mitosis are easily distinguishable because of their almost perfect round shape and a much higher height than flat GBM (see Fig.2A). We observed large calcium oscillations with an almost perfect periodicity in many flat GBM (See Fig.1B). These spontaneous calcium oscillations could last some tens of minutes and were neither associated to cell death nor any loss of cellular integrity as mentioned in previous review article ***(S Patergnani et al. 2020 Int J Mol Sci)***. In other GBM we observed intermittent and almost random calcium flares which were not synchronous in neighboring GBM (Fig.1B).

We investigate whether Ca^{2+} flares trigger glioma migration, as previously proposed ***(S Patergnani et al. 2020 Int J Mol Sci)***. We monitored the profile of glioma exhibiting large and frequent oscillations and we looked to its migration, i.e. to the displacement of its profile in a given time window. As shown in Fig.1D-F we did not observed any significant motion in a time scale of some minutes although in the presence of sustained and large calcium oscillations.

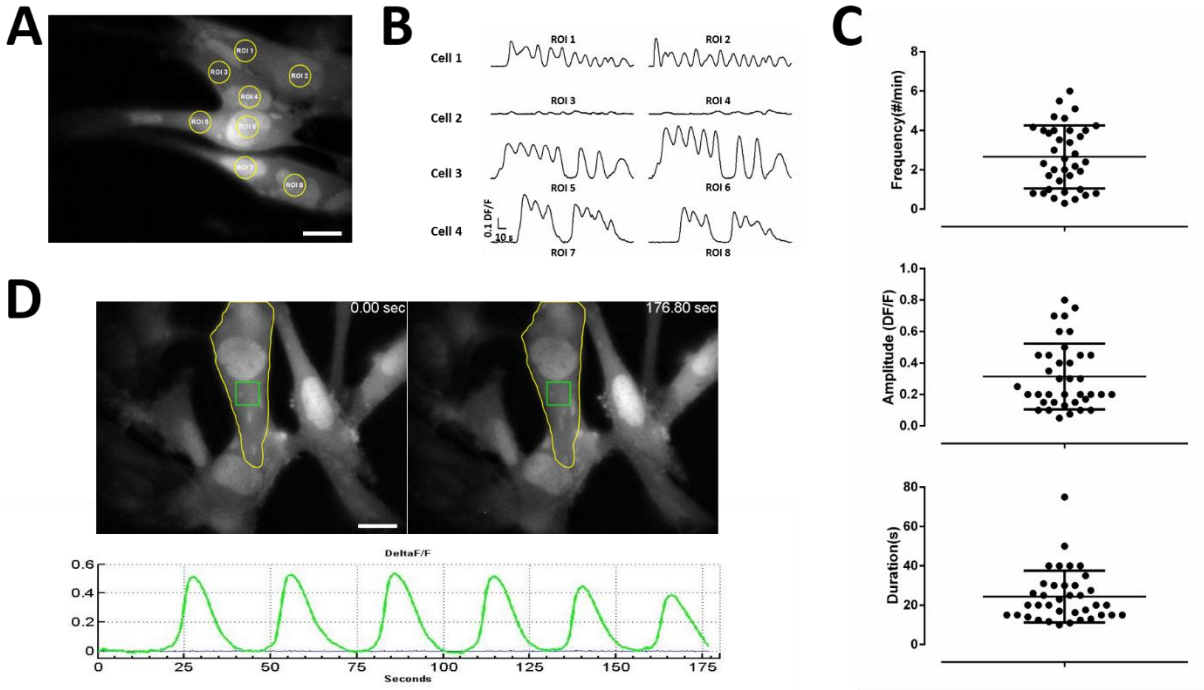

Figure 1 Spontaneous calcium flares *A: group of gliomas stained with OGB-1. Colored squares are Region Of Interest (ROI) which are analyzed in B. B: fractional change of fluorescence DF/F for the corresponding ROI in A. C: from top to bottom are collected data from U87 glioma showing the frequency of spontaneous calcium flares (#/min), their amplitude (DF/F) and their duration (sec). D: images of glioma taken at approximately 3 minutes of time interval, during which clear and large spontaneous calcium flares were observed in the green box (bottom panel) and no clear displacement of the glioma contour (indicated in yellow) was observed. Scale bar:10 μm.*

We decided to focus on GBM during mitosis and we looked for healthy GBM which have entered in the condensed state of mitosis, or anaphase with a perfectly round shape and with a height of 5-10 μm (See inset in Fig.2A).

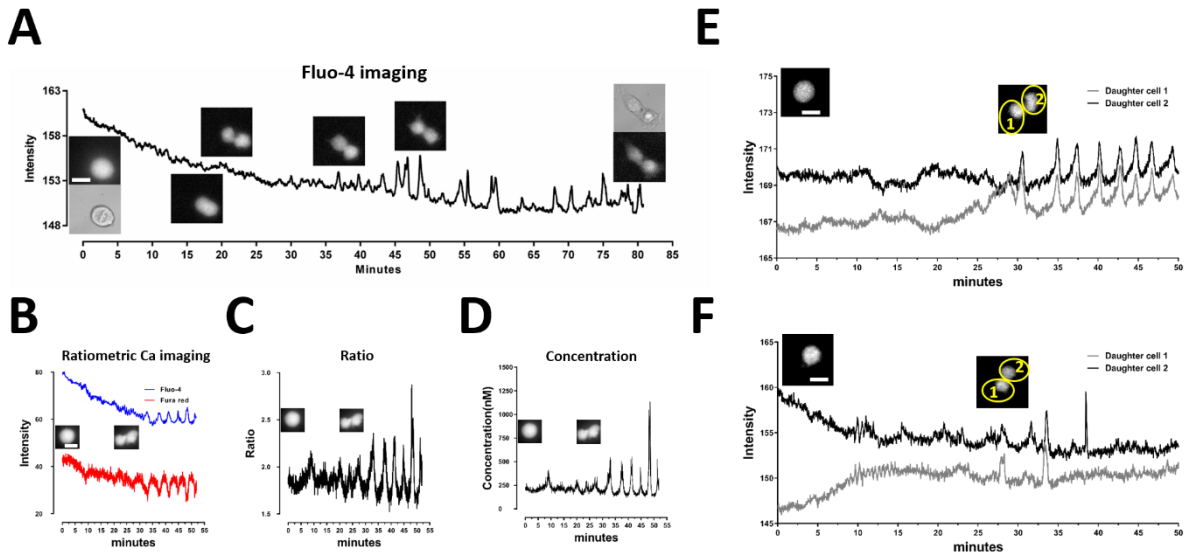

Figure 2 Calcium flares during mitosis *A: decay of the emitted fluorescence from the glioma stained with Fluo-4. During the transition from anaphase and metaphase only the expected dye bleaching was observed and no calcium flares were observed. Clear Calcium flares were observed during telophase and cytokinesis. B: Ratiometric calcium imaging with Fluo-4 (blue trace) and Fura Red (red trace). C: fluorescence ratio R between Fluo-4 and Fura Red. D: Estimation of the absolute change of the concentration of intracellular Calcium using the calibration data reported in Li et al 2020. E,F: synchronous and non-synchronous calcium flares from the two daughter cells of dividing glioma. Scale bar:10* μ*m*

Having found an appropriate condensed GBM, we started imaging the calcium fluorescence at 1 Hz acquiring also bright field images every 5 minutes so to better visualize the mitotic cycle. At the beginning of the experiment shown in Fig. 2A the GBM was in anaphase as demonstrated by the more dense vertical signature seen in bright field (see first inset in Fig. 2A.) and changes of intracellular calcium were monitored for almost 1 hour, during which, as expected, the calcium dye bleached at some extent. When the GBM maintained a perfect round shape we could not detect any significant change of the emitted fluorescence, with the exception of the exponential decline associated to dye bleaching.

However, after the initiation of the telophase, when two new GBM started to divide, large calcium flares were observed (see Fig. 2A). These calcium flares continued to appear for the following 10-20 minutes until the two new GBM almost detached from each other.

We repeated these experiments with plasmids expressing a calcium dyes and in this ways we could follow changes of Ca^{2+} for several hours, up to 4 hours, and we were able to observed almost periodic oscillations with a frequency of 0.2 /0.4 per minute which were associated to slow motion of the GBM occurring with a migratory speed of less than 1 mm per hour (see SI) and a complete cycle of mitosis encompassing shrinking, rounding and cytokinesis (see SI). Also in these experiments we observed large calcium flares occurring primarily during the late stage of telophase and completion of cytokinesis.

Mitotic GBMs often move and shed some portion of their cellular content through blebbing and these biological events dot not allow an exact monitoring of the calcium levels with one single calcium sensitive dye. We decided to confirm these observations using ratiometric calcium imaging using Fura Red and Fluo-4 or OGB-1. Fura Red decreases its emitted fluorescence but OGB-1 increase their emission when Ca^{2+} goes up. Therefore if we see a drop of the fluorescence of Fura Red and concomitant, increase for Fluo-4, there is a genuine increase of Ca^{2+}. By ratiometric calcium imaging and an appropriate calibration procedure (see the reference)***(X Li et al. 2020 J Cell Sci)***, it is possible to quantify the level reached by Ca^{2+} during the observed flares. As shown in Fig. 2D ratiometric calcium imaging

demonstrate large calcium flares during the late phase of the telophase and beginning of cytokinesis reaching levels above 1 μM, the range for which Ca^{2+}-activate Cl^- channels open***(Q Xiao et al. 2011 Proc Natl Acad Sci U S A)***.

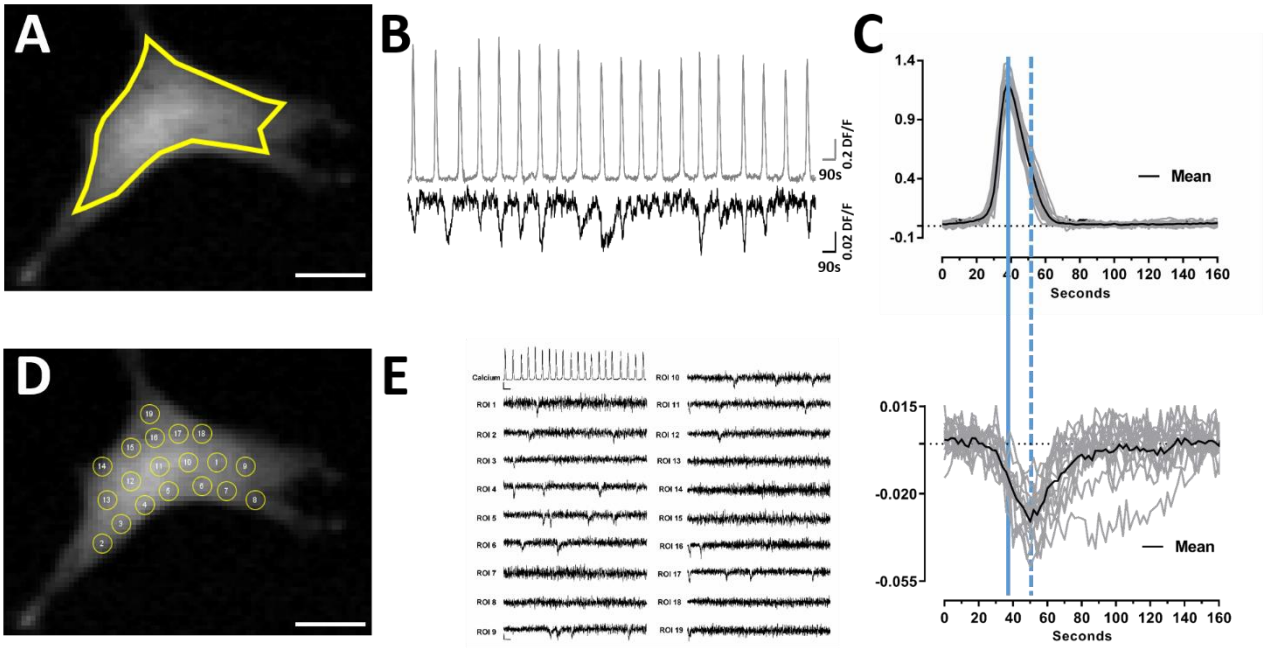

Figure 3 Coupling of Calcium Flares with Cl signals *A: Fluorescence image of a glioma simultaneously expressed genetically encoded sensors for both calcium chloride. The yellow region is the ROI, where DF/F for calcium was measured B: spontaneous calcium flares (in black) observed in the glioma in A and the associated Cl signals (in red).C: mean DF/F in black and single fluorescence changes in grey for Calcium (upper panel) and Cl (lower panel). The peak of the calcium flare proceeds the peak of the Cl signal by about 12 sec. D and E: localization of Cl signals. Yellow circles in D indicate the ROIs individually analyzed in E. Scale bar:10 μm*

As [Ca^{2+}] can reach levels above 1 μM therefore likely to activate a variety of Cl^- channels, such as TMEM16A, TMEM16B, VRAC and possibly other types of Cl channels, we decided to perform similar experiments but using two dyes one sensitive to Ca^{2+} and the other sensitive to Cl^-. Ca^{2+} dyes have been optimized during the last decades, but Cl^- dyes are less sensitive, such as the N-(6- methoxyquinolyl) acetoethyl ester (MQAE) and genetically-encoded Cl^- sensor mClY***(S Zhong et al. 2014 PLoS One)***, so that, at the moment, it is more difficult to detect changes of Cl^- than of Ca^{2+}. The fluorescence emitted by MQAE is quenched by encounters with Cl^- ions, so that an increase of Cl^- is associated to a decrease of the MQAE fluorescence***(Y Ikeuchi et al. 2018 J Physiol Sci)***.

Nonetheless we were able to detect a coupling between calcium flares and increases of Cl^- occurring with a delay varying between 2 and 10 sec (see Fig.3C). The mean amplitude of DF/F for Ca^{2+} flares could be up to 100-150%, but the associated drop of the fluorescence

of mClY was below 10 %. In successful experiments (n=7) during which fluorescence changes were observed for at least 2 hours the averaged maximum value of DF/F calcium flares was 125 +/- 23 % and the associated maximum change of DF/F for chloride was 4.5 +/- 2 %

The maximum Cl^- change followed the peak of the Ca^{2+} flare by 7 +/- 2 sec and the Cl^- fluorescent signal returned to its original level with a time constant of 50-100 sec (Fig.3C), indicating that Cl^- returned to its original level presumably because of the action of the Cl^- exchangers and transporters.

Mechanical stimulation of GBM

Recent studies suggest mechanical cues contribute to the proliferation by triggering rapid cell division, which is mediated by Piezo 1***(SA Gudipaty et al. 2017 Nature)***. Motivated by this observation, I investigated the effect of mechanical stimulation on GBM cells, by using optical tweezer (OT) combined with dual channel imaging for Ca^{2+} and Cl^-. I used also the recently discovered agonist of Piezo 1 – a well known mechanosensitive channel, Yoda 1.

The experiments showed that the stimulations of mechanical forces by OT and the simultaneous exposure to Yoda 1 generates large Ca^{2+} flares. Particularly, pN forces(~15 pN) applied with OT evoked localized Ca^{2+} transients, the amplitudes of which increased with forces(~30 pN) (Fig.4 A and C). Stimulations of pN forces were able to increase both frequencies and amplitudes of the Ca^{2+} flares (Fig.4 B and C). Then I repeated the calcium imaging experiment but with applying also Yoda 1 to the GBM cells. As the result, I saw larger Ca^{2+} flares, Then I performed dual channel imaging for Ca^{2+} and Cl^- , trying to see how Yoda 1 affect that. As expected, the application of Yoda 1 can reliably evoked both significant Ca^{2+} and Cl^- flares within U87 MG GBM cells, which were tightly coupled (Fig.4 D). Afterwards, I repeated this experiment in the primary GBM cells from a patient and I got the similar result. More, I saw that the application of Yoda 1 could make the patient GBMs to be active and able to produce larger spontaneous Ca^{2+} flares, which also activated coupled Cl^- flares (see SI). I found that primary GBM cells from different patients had different responses, especially the Ca^{2+} activated Cl^- flares, which exhibiting different kinetics (see SI). These observations suggest that mechanical cues or stimulations could significantly affect the behavior of GBM cells.

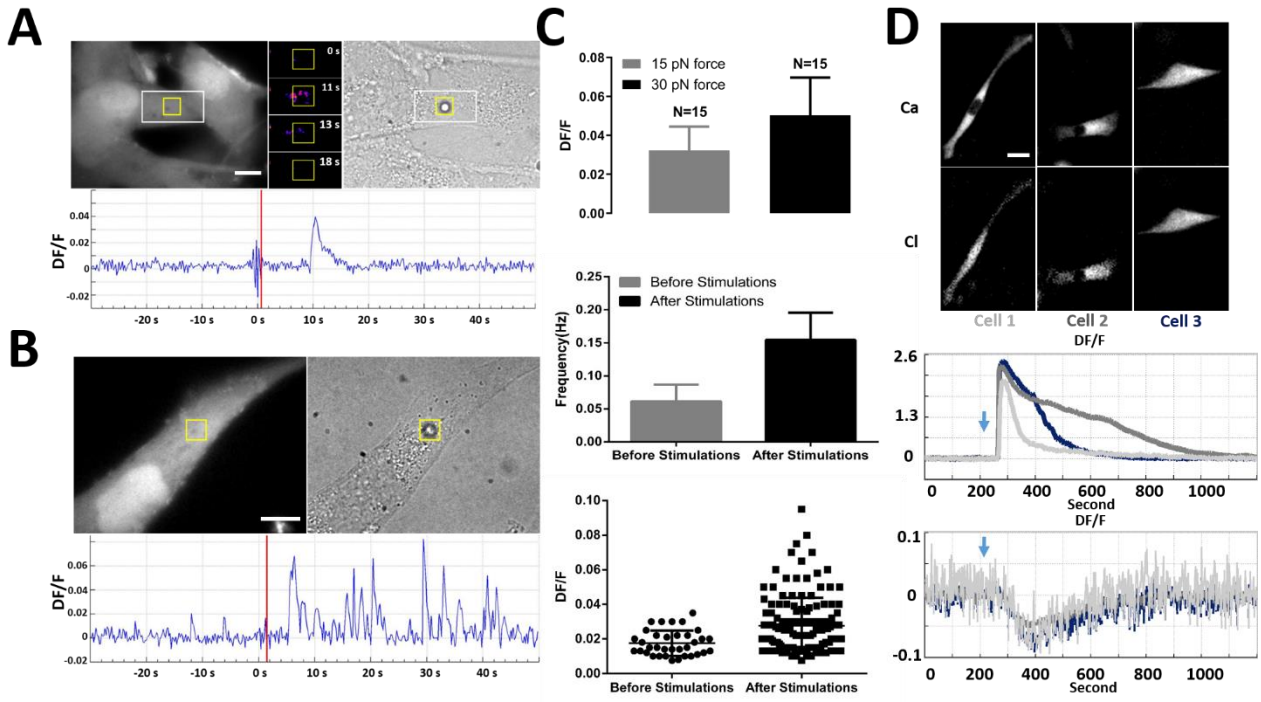

Figure 4: Effect of mechanical stimulation on GBM and associated Ca^{2+} and Cl^- signals. *A: Local Ca^{2+} transient evoked by pN forces using OT. B: Increased frequencies and amplitude of Ca^{2+} flares upon pN forces stimulations. red lines indicate timing of stimulations C: Statistics for local Ca^{2+} (upper), frequencies (center), amplitudes (bottom). D: Ca^{2+} activated Cl influx induced by application Yoda 1 (blue arrow indicating the timing). Scale bar:10 μm*

Coupling of Ca^{2+} flares and Cl^- signals during mitosis

We repeated the same experiment try to visualize the chloride transients during the calcium flares seen during mitosis (Fig.5). Consistently, instead of during metaphase/anaphase, the calcium flares are nearly exclusively found after the anaphase (Fig. 5B) but no clearly coupled Cl^- signals were observed. We further analyzed the coupling of Ca^{2+} flares and Cl^- signals in U87 glioblastoma with Yoda 1. In this case during the late stages of telophase and cytokinesis we observed clear Ca^{2+} flares (Blue trace) (Fig.5A) which were clearly getting bigger by the help of Yoda 1 so to couple with decrease of the Cl^- fluorescence indicating transients elevation of intracellular Cl^- which were likely associated to a welling of the dividing glioblastoma.

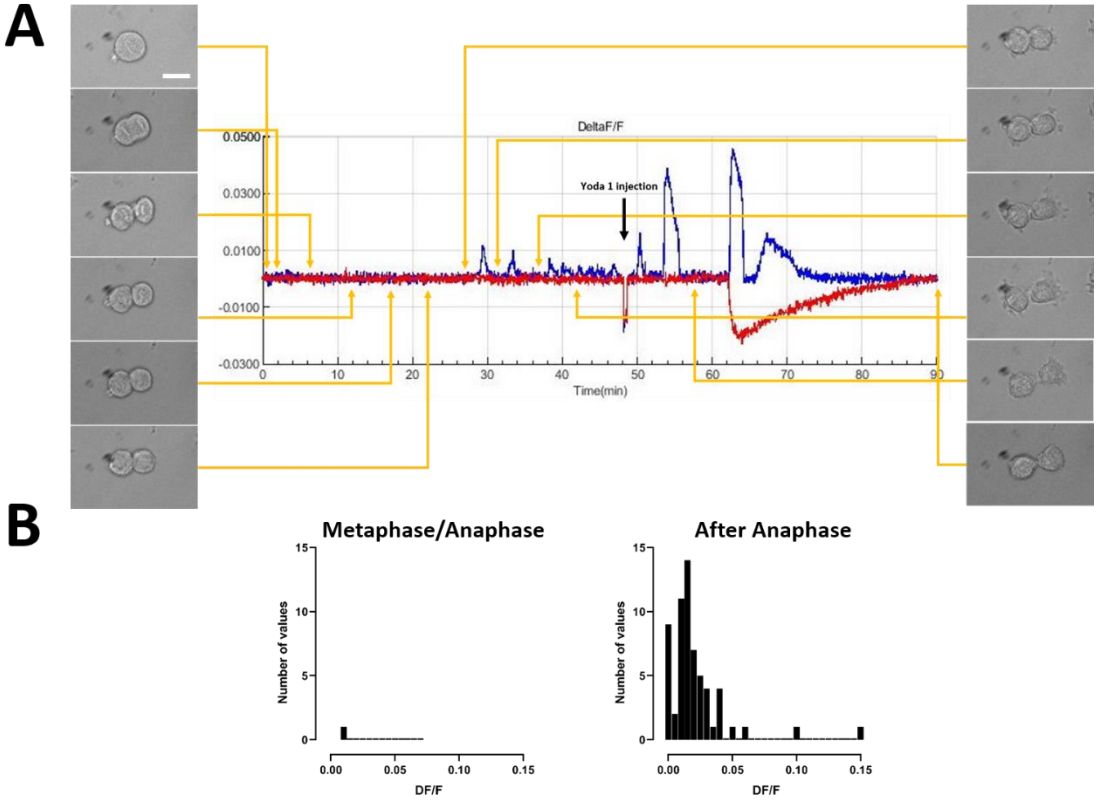

Figure 5: Coupling of Calcium Flares with Cl signals during mitosis *A: Bright field images and DF/F after bleach compensation for Calcium (Blue) and Chloride (red). The addition to the bathing medium of Yoda 1 – an activator of mechanosensitive channels Piezo1 – increases the amplitude of calcium flares and lead to the appearance of a large Cl^- signal triggered by the Calcium flares. The appearance of the Cl^- signal allows a better separation of the two dividing glioma. B:distribution of calcium flares during metaphase/ anaphase and after anaphase. Scale bar:10 μm*

We repeated the same experiments with glioma cells from patients by adding to the medium bathing glioma Yoda 1 for Piezo1 mechanosensitive channels. And we observed, as expected, the similar results. Interestingly, experiments performed with a variety of glioblastoma from patients showed a variable coupling between Calcium flares and Cl^- signals (see SI).

Immunohistochemistry of Cl channels in glioma

In order to determine the identity of the Cl^- channels present in the plasma membrane of GBM and to verify whether some Cl^- channels are specifically expressed during mitosis, we performed immunohistochemical analysis of U87 MG cell lines focusing on possible differences between rounded and flat glioma. Rounded glioma with inside two clear DAPI staining have completed metaphase and are entering in telophase and cytokinesis.

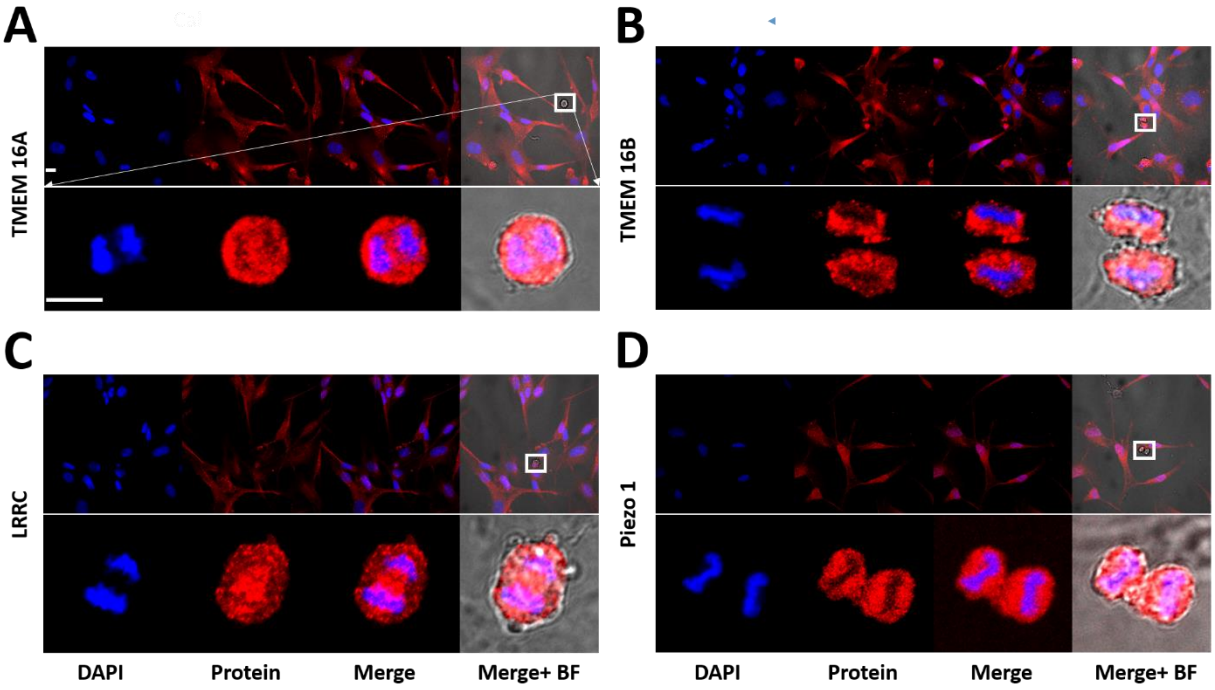

Figure 6: Histochemical analysis of TMEM16A (A) ,TMEM16B (B), VRAC (C) and Piezo1 (Piezo1) channels in U87 glioma in flat cells an in rounded glioma during mitosis. *In each panel from left to right staining with DAPI (blue), staining of specific antibody in red, superposition of the staining of DAPI and of the antibody and finally the superposition of these staining with a bright field image. The section in the white bow is zoomed in the lower portion of each panel and shows a glioma during mitosis where the chromosomes have already divided, but the glioma is still in its perfectly rounded conformation. Scale bar:10 μm*

The expression of the two Cl^- channels of the TMEM16 family, i.e. TMEM16A and TMEM16B were similarly expressed in rounded and flat glioma (Fig.6). We repeated the same observation with the antibody for LRRC, a known subunit of the VRAC channel.

Therefore our immunohistochemical investigation did not find any significant difference of the expression of the TMEM16A, TMEM16B and VRAC channels in flat U87 glioma and in those which have entered mitosis and therefore have a rounded shape and two blue staining indicating chromosome division.

Piezo1 is mechanosensitive channel permeable to Ca^{2+} ions and is thought to play a major role in glioma replication, indeed its opening and the concomitant elevation of intracellular Ca^{2+} could lead to the activation of a variety of Cl^- channels ***(L Gao et al. 2021 ACS Omega)***.

Discussion

The present manuscript describes some mayor and novel biophysical properties of replication of GBM occurring at the membrane level of dividing GBM. Firstly we show that during mitosis the transition from a perfectly rounded GBM (from prometaphase to anaphase) to the telophase occurs in the absence of significant – or more appropriately detectable - changes of $[Ca^{2+}]_i$. Secondly, the activation of Ca-sensitive Cl channels is necessary for the completion of mitosis and in particular of cytokinesis occurring in the presence of large Ca spontaneous flares. Thirdly, Piezo1 play a major role in glioma replication as its opening and the concomitant elevation of intracellular Ca^{2+} could lead to the activation of a variety of Cl^- channels, contributing to glioblastoma fast and deadly mitotic cycle.

Ca^{2+} flares in GBM

We have previously observed large spontaneous Ca flares in U87 GBM and in GBM from patients ***(X Li et al. 2020 J Cell Sci)***. These flares can reach values in the order of 1-5 μM a range where several mayor biological processes are activated such as the activation of Ca-sensitive K+ and Cl^- ionic channels, cell death and a several other biological process. The biological mechanisms at the origin of these flares is unknown but could involve intracellular proteins involved in Ca^{2+} homeostasis such as the mitochondrial Ca^{2+} uniporter (MCU) and membrane proteins such as calcium channels. All these proteins are likely to be regulated and triggered by the expression of genes involved in mitosis, i.e. events occurring in GBM nucleus.

The functional role of these flares is likely to be variable and complex. For instance, these flares could be involved in GBM migration but we observed long and large Ca^{2+} flares in static GBM and some GBM migration can be observed only after prolonged Ca^{2+} flares lasting for tens of minutes.

Cl^- channels in GBM far from mitosis and during mitosis

During mitosis all cells profoundly modify their cellular interior and it is possible that also membrane proteins and in particular Cl^- channels undergo changes of their expression level and/or of their properties. Therefore we looked in details with electrophysiological means to the properties of Cl^- channels in rounded and flat GBM: flat GBM are from mitosis, while perfectly rounded GBM with a height of more than 5-7 μM are likely to be in some mitotic stages such as prophase, metaphase and anaphase. Under bright field illumination a

straight line observed in the middle of the GBM suggests that the GBM has entered metaphase and is proceeding in mitosis.

In collaboration with Andres Hernandez, Cesar Trivino and Anna Menini, we found that the electrical properties of flat and rounded GBM differ in a significant and possibly very important way. In rounded GBM cells – during the mitotic cycle - from one patient we observed clear – and not expected - voltage gated _Na+ currents, not observed in flat GBM far from the mitotic cycle. Rounded GBM exhibit significant Cl^- activated by levels of intracellular Ca^{2+} less than 500 nM, i.e. around the its resting level.

GBM swelling during telophase and cytokinesis

My recordings of changes of Ca^{2+} with usual calcium dyes, with ratiometric Ca^{2+} dyes and with plasmid-based Calcium sensors (Fig.1, 2, 3) show large Ca flares occurring primarily – and possibly only – during the late steps of the telophase and cytokinesis, i.e. when GBM have to divide and ultimately duplicate their volume. When a protocol specifically developed to analyze Ca^{2+}-activated Cl^- currents in other cells, such as chemoreceptors, is used we observed Ca^{2+}-activated Cl^- currents with a kinetics and properties reminiscent of what observed with TMEM16A.TMEM16B and VRAC channels.

Immunohistochemistry analysis shows that these ionic channels are present in the cellular membrane of rounded and flat cells (Fig. 6), but their sensitivity to Ca^{2+} is lost, presumably because of a subtle control from the nuclear events occurring during mitosis.

Calcium flares and chloride flux in GBM replication, from the view of mechanosensitivity

Mitosis in all cells have similar properties and in many other kinds of cancers, such as the colon rectal cancer, mitotic cancer cells round, divide and then becomes flat, during stretching forces could likely activate related Ca^{2+} channels like Piezo 1 so that Cl- channels most likely Ca^{2+}-activated channels operate to support dividing at the end of mitosis. In this respect, replication is controlled and regulated in a much more complex way where mechanosensitive channels, such as Piezo 1 (see Fig.4, 5, 6) have a much important role. It is also possible that Cl^- channels, most likely with different structures and properties play a similar role.

Methods

Cell culture

U87 GBM cells (#89081402, Sigma-Aldrich) were cultured in DMEM supplemented with 10% fetal bovine serum (FBS; Invitrogen, Life Technologies, Gaithersburg, MD), 1% PenStrep (100 U/ml penicillin and 100 µg/ml streptomycin; Invitrogen).

To obtain human GSCs, human GBM samples were collected by the Neurosurgery Department of the Azienda Ospedaliera Universitaria of Udine, after informed consent was obtained, in accordance with the Declaration of Helsinki, and with approval by the Independent Ethics Committee of the University Hospital of Udine (Approval 196/2014Em). Human GSCs were expanded in adherent culture following the protocol optimized by Dirk's group to maintain undifferentiated GSCs in adherent condition ***(SM Pollard et al. 2009 Cell Stem Cell, L Andolfi et al. 2014 PLoS One, E Bourkoula et al. 2014 Stem Cells)***. Briefly, tissue samples were mechanically enzymatically dissociated and single-cell suspensions were cultured with adhesion on laminin-coated dishes in a growing medium composed of the following: Neurobasal™-A Medium (#10888, Gibco by Invitrogen) supplemented with 2 mM L-glutamine (#G7513, Sigma-Aldrich), 1× N2 supplement [7.5% bovine serum albumin (BSA), 0.63 µg/ml progesterone, 1.6 mg/ml putrescine dihydrochloride, 0.52 µg/ml sodium selenite], 25 µg/ml insulin (#I2643, Sigma-Aldrich), 1× penicillin-streptomycin (#15140122, Gibco by Invitrogen), 100 µg/ml h-apo-transferrin (#P4333, Sigma-Aldrich), 1× B-27 supplement (#17504-044, Gibco by Invitrogen), 20 ng/ml h-FGF-basic (#100-18B, Peprotech), 20 ng/ml h-EGF (#AF-100-15, Peprotech).

All the cells were cultured in an incubator at 37°C, 5%O2/5% CO2, 95% relative humidity and medium was replaced every 3 days. Once 70–80% of confluence had been reached, the cells were re-plated at a density of $2.5\times10^3/cm^2$.

Transfection

mClY-N1 and pGP-CMV-NES-jRCaMP1b was Addgene plasmid #90457 and #63136. Twenty-four hours after plating the cells, cells were transfected with plasmids sensors using the empty vector as a control; U87 GBM cells were transfected with Lipofectamine 3000® transfection reagent (Invitrogen), following the manufacturer's protocol.

Live-cell imaging

Cells were plated at a density of 8.0×10^4 cells into 35-mm dishes with a glass bottom and cultured for 2 days. Live-cell imaging experiments were performed on an epi-fluorescence microscope (Olympus IX-83, Olympus) equipped with a chamber incubator (Okolab, Pozzuoli, Italy) and light-emitting diode (LED) illumination (λ=365 nm for MQAE; λ=480 nm for OGB-1; λ=500 nm for mClY; λ=560 nm for jRCaMP1b,). During all imaging experiments, cells were kept at 37°C, 5% CO2 and 95% humidity. Time-lapse images were taken with 300-500 ms of exposure time. Images were acquired with a charge-coupled device (CCD) sensor at 12-bit depth (ORCA-D2, Hamamatsu) using a 20× air objective (Olympus, NA=0.75) or a 40× oil objective (Olympus, NA=1.3) with a spatial resolution of 1280×960 pixels.

Ca^{2+} imaging

In Ca^{2+}-imaging experiments, 2.0×10^4 cells were plated on a flat coverslip and cultured for 1–6 days, and subsequently were loaded with the membrane-permeable Ca^{2+} dye Fluo-4 AM or Oregon Green 488 BAPTA, AM (Life Technologies) by incubation with 4 μM Fluo-4 or OGB-1 (dissolved in anhydrous DMSO, 4 mM stock solution) in DMSO (Life Technologies) at a ratio of 1:1 in Ringer's solution (145 mM NaCl, 3 mM KCl, 1.5 mM $CaCl_2$, 1 mM $MgCl_2$, 10 mM glucose and 10 mM Hepes, pH 7.4) at 37°C for 30 min. After incubation, the cultures were washed with Ringer's solution for 20 min and then transferred to the stage of a Nikon Eclipse Ti-U inverted microscope equipped with a piezoelectric table (Nano-ZI Series 500 μm range, Mad City Labs), an HBO 103 W/2 mercury short arc lamp (Osram, Munich, Germany), a mirror unit (465–495 nm excitation bandpass filter, 505 nm dichroic, 515–555 nm emission bandpass filter) and an Electron Multiplier CCD Camera C9100-13 (Hamamatsu Photonics, Japan). Ca^{2+}-imaging recordings were performed at room temperature and images were acquired using the NIS Element software (Nikon, Japan) with an S-Fluor 20×/0.75 NA objective, at a sampling rate of 3–10 Hz, with a spatial resolution of 256×256 pixels for 15 min. To avoid saturation of the signals, excitation light intensity was attenuated by ND4 and ND8 neutral density filters (Nikon, Tokyo, Japan).

For ratiometric Ca^{2+}-imaging experiments, cells were loaded with 1.5 μM Fluo-4 or OGB-1 AM [dissolved in anhydrous DMSO (Sigma-Aldrich), 1.5 mM stock solution], 2.5 μM Fura Red AM [dissolved in anhydrous DMSO (Sigma-Aldrich), 2.5 mM stock solution] in DMSO (Life Technologies) in 1 ml Ringer's solution for 30 min. After incubation, the cultures were washed with Ringer's solution for 20 min and then transferred to the stage of an epi-

fluorescence microscope (Olympus IX-83, Olympus) equipped with a chamber incubator (Okolab, Pozzuoli, Italy), LED illumination (λ=490 nm for both Fluo-4/OGB-1 and Fura Red AM) and a CCD camera (ORCA-D2, Hamamatsu) with a dual sensor to record the fluorescence images from OGB-1 (520±17.5 nm) and Fura Red AM (640±37.5 nm) simultaneously. During all imaging experiments, cells were kept at 37°C, 5% CO2 and 95% humidity. Time-lapse images were taken with 300 ms of exposure time. All acquisitions were operated with a 20× air objective (Olympus, NA=0.75) or a 40× oil objective (Olympus, NA=1.3).

Immunofluorescence

Cells were grown on coverslips for 2 days and subsequently washed with ice-cold PBS, then fixed with 4% paraformaldehyde for 10 min at room temperature, followed by permeabilization with PBS plus 0.1% Triton X-100, blocked with 3% BSA and incubated overnight with primary antibody anti-TMEM 16A, TMEM 16B, LRRC and Piezo1, which are all rabbit monoclonal (1:500). The cells were then washed with PBS three times for 5 min each, and incubated with Alexa Fluor 488-labelled goat anti-mouse secondary antibody (1:1000; Life Technologies) at room temperature for 1 h. The cells were examined with a confocal microscope (Nikon A1R).

Optical manipulation

To mechanically stimulate the cell, I used a custom-built optical tweezer combined with an inverted microscope described in detail in (8). Briefly, I used a polystyrene bead with a 3.5-μm diameter (G. Kisker Biotech Germany) optically trapped in a controllable oscillatory optical trap (OOT). We used an infrared (IR) laser at 1064 nm for trapping (IPG Laser Germany). The axial position of the trap could be adjusted within a range of 0 – 20 μm using a custom designed two-lens system composed of a focus tunable lens (EL-10-30-NIR-LD, Optotune AG, Switzerland), of which the focal length can be varied by computer con-trol (LabVIEW code).

Data and statistical analysis

For calcium and chloride experiments, the DF/F values were obtained through custom MATLAB (The MathWorks, Natick, MA, USA) code and the ImageJ software v1.6 (National Institutes of Health, Bethesda, MD, USA). All results are presented as mean ± SD, and significant differences were determined using a t test with $p < 0.05$ (GraphPad Prism 7, GraphPad soft-ware, San Diego, CA, USA).

References

N Prevarskaya, et al. (2010). "Ion channels and the hallmarks of cancer." Trends Mol Med **16**(3): 107-121.

VA Cuddapah, et al. (2011). "Ion channels and transporters [corrected] in cancer. 2. Ion channels and the control of cancer cell migration." Am J Physiol Cell Physiol **301**(3): C541-549.

GR Monteith, et al. (2017). "The calcium-cancer signalling nexus." Nat Rev Cancer **17**(6): 367-380.

CW Habela, et al. (2007). "Cytoplasmic volume condensation is an integral part of mitosis." Cell Cycle **6**(13): 1613-1620.

X Li, et al. (2020). "Mechanisms of malignancy in glioblastoma cells are linked to mitochondrial Ca(2) (+) uniporter upregulation and higher intracellular Ca(2+) levels." J Cell Sci **133**(6).

L Andolfi, et al. (2014). "Investigation of adhesion and mechanical properties of human glioma cells by single cell force spectroscopy and atomic force microscopy." PLoS One **9**(11): e112582.

E Bourkoula, et al. (2014). "Glioma-associated stem cells: a novel class of tumor-supporting cells able to predict prognosis of human low-grade gliomas." Stem Cells **32**(5): 1239-1253.

S Patergnani, et al. (2020). "Various Aspects of Calcium Signaling in the Regulation of Apoptosis, Autophagy, Cell Proliferation, and Cancer." Int J Mol Sci **21**(21).

Q Xiao, et al. (2011). "Voltage- and calcium-dependent gating of TMEM16A/Ano1 chloride channels are physically coupled by the first intracellular loop." Proc Natl Acad Sci U S A **108**(21): 8891-8896.

S Zhong, et al. (2014). "A genetically-encoded YFP sensor with enhanced chloride sensitivity, photostability and reduced ph interference demonstrates augmented transmembrane chloride movement by gerbil prestin (SLC26a5)." PLoS One **9**(6): e99095.

Y Ikeuchi, et al. (2018). "Measurement of [Cl(-)]i unaffected by the cell volume change using MQAE-based two-photon microscopy in airway ciliary cells of mice." J Physiol Sci **68**(2): 191-199.

SA Gudipaty, et al. (2017). "Mechanical stretch triggers rapid epithelial cell division through Piezo1." Nature **543**(7643): 118-121.

L Gao, et al. (2021). "Suppression of Esophageal Squamous Cell Carcinoma Development by Mechanosensitive Protein Piezo1 Downregulation." ACS Omega **6**(15): 10196-10206.

SM Pollard, et al. (2009). "Glioma stem cell lines expanded in adherent culture have tumor-specific phenotypes and are suitable for chemical and genetic screens." Cell Stem Cell **4**(6): 568-580.

Conclusion & Future Perspectives

Ca^{2+} signaling and dynamics is surprisingly versatile at regulating nearly every aspect of key cellular functions, which also reflects complexity of calcium Signaling and dynamics. This complexity has been attracting us to pursue the significance of calcium signaling and dynamics regarding specific biological processes. Therefore, in this thesis, we are trying to conclude the significance reflected by the calcium signaling and dynamics, which is specific to distinct cellular processes such as phototransduction, mechanotransduction and glioma malignancy, within different type CNS cells including rod photoreceptors, primary hippocampal neurons, and glioblastoma cells. The conclusions as well as corresponding brief future perspectives are summarized as follows depending on the cells investigated:

1. Rod photoreceptors

The work on rod photoreceptors guided by calcium imaging using CaSiR-1 AM, revealed and confirmed several functional and structural properties of the rod OS vary longitudinally: there is a sharp gradient of $[Ca^{2+}]_i$, responsiveness, the occurrence of calcium flares, and the structural components of OS. It suggests the rod OS is not a homogeneous structure and displays both a functional and a structural gradient, where new discs are synthetized and shed. Of note, the existence of spontaneous and light-induced calcium flares, i.e., highly localized increases in $[Ca^{2+}]_i$ is a, to some extent, unexpected feature of the rod OS. Calcium flares colocalize with discs inside the OS, indicating that they probably originate from the discs. Therefore, that calcium flares may be part of the disk renewal and shedding process and could signal retinal pigmented epithelium cells to trigger phagocytosis of aged and shedding discs.

Another remarkable feature of Ca^{2+} dynamics in rods is summarized as the strong compartmentalization of calcium dynamics between the IS and OS which is likely to be caused by the high density of mitochondria present in the IS near the cilium. This leads to the hypothesis that presence of the inner segment affects activities in the outer segment as calcium flares are rarely observed in isolated OS.

Finally, it is believed the functional and structural gradient of the phototransduction machinery is developed to maximize the detection of photons, as photons arrives from the external world impinge first on the OS base. Indeed, this could be one of the reasons for the geometrical arrangement of the retina inside the eye in which photons travel through the entire retina before reaching the rods: In this way, the first encountered rhodopsin molecules are those located at the OS base that efficiently initiate phototransduction.

The work on the mechanosensitivity of the rods, showed that 1) mechanosensitive

channels (MSCs), transient receptor potential canonical 1 (TRPC1), and Piezo1 are present in rod inner segments (ISs); 2) mechanical stimulation of the order of 10 pN—applied briefly to either the OS or IS evokes calcium transients; 3) inhibition of MSCs decreases the duration of photoresponses to bright flashes; 4) bright flashes of light induce a rapid shortening of the OS; and 5) the genes encoding the TRPC family have an ancient association with the genes encoding families of protein involved in phototransduction. These results suggest that MSCs play an integral role in rods' phototransduction.

Future work will be focus on the molecular basis underling the structural and functional gradient of the phototransduction machinery and especially figure out how the Ca^{2+} are involved in this molecular basis as well as potent pathways coupling the mechanotransduction of rods.

2. Primary hippocampal neurons

The investigation on the pN forces sensing and transduction by the optical tweezer (OT) showed very weak mechanical stimuli act as repulsive stimuli, similar to chemical repulsive signaling, and hippocampal GCs turn away from the site of mechanical stimulation. It suggests mechanical signaling operates in hippocampal neurons for very weak forces. Therefore, it can be summarized that hippocampal neurons, in addition to the usual chemical and electrical signals, exchange mechanical signals.

For future perspectives on this topic, it is necessary to detail and dissect the roles of different calcium signaling components like mitochondria, ER, within mechanotransduction of pN forces and the related behaviors occurring in the neurons. With this, more intact and larger network of calcium signaling need to be established.

3. Glioblastoma cells

The preliminary work on glioblastoma cells showed large Ca^{2+} flares unexpectedly occur primarily and possibly only during the late steps of the telophase and cytokinesis, though these calcium flares can be increased by Yoda 1 to activate favorable chloride signals. Immunohistochemistry analysis shows that these ionic channels including TMEM 16A, TMEM 16B and VRAC are present in the cellular membrane of rounded and flat cells. It may suggest sensitivity of the above related channels to Ca^{2+} is lost, presumably because of a subtle control from the nuclear events occurring during mitosis. On the other hand, it is also possible that in the tissue, replication is controlled and regulated in a much more complex way where

mechanosensitive channels, such as Piezo 1 have a much important role.

The future work needs to address the questions about how Ca^{2+} take part in the cell volume regulations, especially those related to mitosis, and how activities TMEM 16 A/B are the different between normal cells and cells undergoing mitosis, especially their interactions with Ca^{2+}. In addition, it is necessary to develop quantitative analysis methods for both chloride signals and its coupling with Ca^{2+}.

References

D. Aguilar-Morante, et al. (2015). "CCAAT/enhancer binding protein beta induces motility and invasion of glioblastoma cells through transcriptional regulation of the calcium binding protein S100A4." Oncotarget **6**(6): 4369-4384.

L. Arenillas, et al. (2016). "Considering Bone Marrow Blasts From Nonerythroid Cellularity Improves the Prognostic Evaluation of Myelodysplastic Syndromes." J Clin Oncol **34**(27): 3284-3292.

G. J. Augustine, et al. (2003). "Local calcium signaling in neurons." Neuron **40**(2): 331-346.

R. Bagur and G. Hajnoczky (2017). "Intracellular Ca(2+) Sensing: Its Role in Calcium Homeostasis and Signaling." Mol Cell **66**(6): 780-788.

K. G. Baimbridge, et al. (1992). "Calcium-binding proteins in the nervous system." Trends Neurosci **15**(8): 303-308.

G. S. Baird (2011). "Ionized calcium." Clin Chim Acta **412**(9-10): 696-701.

A. Bartok, et al. (2019). "IP3 receptor isoforms differently regulate ER-mitochondrial contacts and local calcium transfer." Nat Commun **10**(1): 3726.

M. J. Berridge, et al. (2003). "Calcium signalling: dynamics, homeostasis and remodelling." Nat Rev Mol Cell Biol **4**(7): 517-529.

M. J. Berridge, et al. (2000). "The versatility and universality of calcium signalling." Nat Rev Mol Cell Biol **1**(1): 11-21.

T. Boczek, et al. (2021). "Crosstalk among Calcium ATPases: PMCA, SERCA and SPCA in Mental Diseases." Int J Mol Sci **22**(6).

M. D. Bootman, et al. (2001). "Calcium signalling--an overview." Semin Cell Dev Biol **12**(1): 3-10.

L. Boyman, et al. (2013). "NCLX: the mitochondrial sodium calcium exchanger." J Mol Cell Cardiol **59**: 205-213.

E. Bozler (1954). "Interactions between magnesium, pyrophosphate, and the contractile elements." J Gen Physiol **38**(1): 53-58.

M. Brini and E. Carafoli (2011). "The plasma membrane Ca(2)+ ATPase and the plasma membrane sodium calcium exchanger cooperate in the regulation of cell calcium." Cold Spring Harb Perspect Biol **3**(2).

M. Brini, et al. (1999). "Targeted recombinant aequorins: tools for monitoring [Ca2+] in the various compartments of a living cell." Microsc Res Tech **46**(6): 380-389.

F. Bronner (2001). "Extracellular and intracellular regulation of calcium homeostasis." ScientificWorldJournal **1**: 919-925.

E. Carafoli (2002). "Calcium signaling: a tale for all seasons." Proc Natl Acad Sci U S A **99**(3): 1115-1122.

L. Chen, et al. (2019). "Annexin A2 regulates glioma cell proliferation through the STAT3cyclin D1 pathway." Oncol Rep **42**(1): 399-413.

X. Cheng, et al. (2010). "Mucolipins: Intracellular TRPML1-3 channels." FEBS Lett **584**(10): 2013-2021.

W. Cho and R. V. Stahelin (2005). "Membrane-protein interactions in cell signaling and membrane trafficking." Annu Rev Biophys Biomol Struct **34**: 119-151.

D. E. Clapham (2007). "Calcium signaling." Cell **131**(6): 1047-1058.

V. A. Cuddapah and H. Sontheimer (2011). "Ion channels and transporters [corrected] in cancer. 2. Ion channels and the control of cancer cell migration." Am J Physiol Cell Physiol **301**(3): C541-549.

C. Cui, et al. (2019). "Progress in understanding mitochondrial calcium uniporter complex-mediated calcium signalling: A potential target for cancer treatment." Br J Pharmacol **176**(9): 1190-1205.

E. Dagdan, et al. (2011). "Functional assessment of a promoter polymorphism in S100B, a putative risk variant for bipolar disorder." Am J Med Genet B Neuropsychiatr Genet **156B**(6): 691-699.

S. Das, et al. (2021). "The role of cGMP-signalling and calcium-signalling in photoreceptor cell death: perspectives for therapy development." Pflugers Arch **473**(9): 1411-1421.

D. De Felice and A. Alaimo (2020). "Mechanosensitive Piezo Channels in Cancer: Focus on altered Calcium Signaling in Cancer Cells and in Tumor Progression." Cancers (Basel) **12**(7).

R. A. de Melo Reis, et al. (2020). "Cell Calcium Imaging as a Reliable Method to Study Neuron-Glial Circuits." Front Neurosci **14**: 569361.

D. De Stefani, et al. (2016). "Enjoy the Trip: Calcium in Mitochondria Back and Forth." Annu Rev Biochem **85**: 161-192.

M. L. Delco and L. J. Bonassar (2021). "Targeting calcium-related mechanotransduction in early OA." Nat Rev Rheumatol **17**(8): 445-446.

I. Delvendahl, et al. (2015). "Reduced endogenous Ca2+ buffering speeds active zone Ca2+ signaling." Proc Natl Acad Sci U S A **112**(23): E3075-3084.

Björn-Philipp Diercks and Andreas H (2020). "Unexpected players for local calcium signals: STIM and ORAI proteins." Current Opinion in Physiology **17**: 17-24.

X. Ding, et al. (2010). "Essential role of TRPC6 channels in G2/M phase transition and development of human glioma." J Natl Cancer Inst **102**(14): 1052-1068.

A. N. Dodd, et al. (2010). "The language of calcium signaling." Annu Rev Plant Biol **61**: 593-620.

S. Ebashi (1961). "Calcium binding activity of vesicular relaxing factor." J Chir (Paris) **82**: 236-244.

S. Ebashi and A. Kodama (1965). "A new protein factor promoting aggregation of tropomyosin." J Biochem **58**(1): 107-108.

S. Ebashi and F. Lipmann (1962). "Adenosine Triphosphate-Linked Concentration of Calcium Ions in a Particulate Fraction of Rabbit Muscle." J Cell Biol **14**(3): 389-400.

G. C. Faas and I. Mody (2012). "Measuring the kinetics of calcium binding proteins with flash photolysis." Biochim Biophys Acta **1820**(8): 1195-1204.

R. Fairless, et al. (2019). "Calcium-Binding Proteins as Determinants of Central Nervous System Neuronal Vulnerability to Disease." Int J Mol Sci **20**(9).

J. K. Foskett, et al. (2007). "Inositol trisphosphate receptor Ca2+ release channels." Physiol Rev **87**(2): 593-658.

A. Galione (2015). "A primer of NAADP-mediated Ca(2+) signalling: From sea urchin eggs to mammalian cells." Cell Calcium **58**(1): 27-47.

J. C. Gilliam, et al. (2012). "Three-dimensional architecture of the rod sensory cilium and its disruption in retinal neurodegeneration." Cell **151**(5): 1029-1041.

C. Grienberger and A. Konnerth (2012). "Imaging calcium in neurons." Neuron **73**(5): 862-885.

N. Grillet, et al. (2009). "The mechanotransduction machinery of hair cells." Sci Signal **2**(85): pt5.

C. W. Habela and H. Sontheimer (2007). "Cytoplasmic volume condensation is an integral part of mitosis." Cell Cycle **6**(13): 1613-1620.

J. Hao and P. Delmas (2011). "Recording of mechanosensitive currents using piezoelectrically driven mechanostimulator." Nat Protoc **6**(7): 979-990.

W. Harley, et al. (2010). "Dual inhibition of sodium-mediated proton and calcium efflux triggers non-apoptotic cell death in malignant gliomas." Brain Res **1363**: 159-169.

W. Hasselbach and M. Makinose (1961). "[The calcium pump of the "relaxing granules" of muscle and its dependence on ATP-splitting]." Biochem Z **333**: 518-528.

L. V. Heilbrunn and F. J. Wiercinski (1947). "The action of various cations on muscle protoplasm." J Cell Comp Physiol **29**(1): 15-32.

A. Hernandez-Cruz, et al. (1990). "Subcellular calcium transients visualized by confocal microscopy in a voltage-clamped vertebrate neuron." Science **247**(4944): 858-862.

U. C. Hoppe (2010). "Mitochondrial calcium channels." FEBS Lett **584**(10): 1975-1981.

H. J. Hu, et al. (2019). "Blockade of the forward Na(+) /Ca(2+) exchanger suppresses the growth of glioblastoma cells through Ca(2+) -mediated cell death." Br J Pharmacol **176**(15): 2691-2707.

N. Huang, et al. (2013). "Overexpression of S100A9 in human glioma and in-vitro inhibition by aspirin." Eur J Cancer Prev **22**(6): 585-595.

E. Jarratt-Barnham, et al. (2021). "The Complex Story of Plant Cyclic Nucleotide-Gated Channels." Int J Mol Sci **22**(2).

L. Kang, et al. (2010). "C. elegans TRP family protein TRP-4 is a pore-forming subunit of a native mechanotransduction channel." Neuron **67**(3): 381-391.

U. B. Kaupp and R. Seifert (2002). "Cyclic nucleotide-gated ion channels." Physiol Rev **82**(3): 769-824.

J. M. Kefauver, et al. (2020). "Discoveries in structure and physiology of mechanically activated ion channels." Nature **587**(7835): 567-576.

K. S. Kindt, et al. (2007). "Caenorhabditis elegans TRPA-1 functions in mechanosensation." Nat Neurosci **10**(5): 568-577.

G. G. Kovacs, et al. (2005). "Changes in intracellular Ca2+ and pH in response to thapsigargin in human glioblastoma cells and normal astrocytes." Am J Physiol Cell Physiol **289**(2): C361-371.

D. Krizaj and D. R. Copenhagen (2002). "Calcium regulation in photoreceptors." Front Biosci **7**: d2023-2044.

F. O. Lemos and B. E. Ehrlich (2018). "Polycystin and calcium signaling in cell death and survival." Cell Calcium **69**: 37-45.

G. Li, et al. (2013). "Suppression of STIM1 inhibits human glioblastoma cell proliferation and induces G0/G1 phase arrest." J Exp Clin Cancer Res **32**: 20.

J. Li, et al. (2014). "Piezo1 integration of vascular architecture with physiological force." Nature **515**(7526): 279-282.

L. H. Li, et al. (2013). "The Golgi Apparatus: Panel Point of Cytosolic Ca(2+) Regulation." Neurosignals **21**(3-4): 272-284.

T. Li, et al. (2018). "The interactome and spatial redistribution feature of Ca(2+) receptor protein calmodulin reveals a novel role in invadopodia-mediated invasion." Cell Death Dis **9**(3): 292.

X. Li, et al. (2021). "Overexpression of Annexin A2 promotes proliferation by forming a Glypican 1/c-Myc positive feedback loop: prognostic significance in human glioma." Cell Death Dis **12**(3): 261.

Xiaoyun Li, et al. (2020). "Mechanisms of malignancy in glioblastoma cells are linked to mitochondrial Ca(2) (+) uniporter upregulation and higher intracellular Ca(2+) levels." J Cell Sci **133**(6).

P. A. Liebman, et al. (1982). "Lateral diffusion of visual pigment in rod disk membranes." Methods Enzymol **81**: 660-668.

E. Lloyd-Evans (2016). "On the move, lysosomal CAX drives Ca2+ transport and motility." J Cell Biol **212**(7): 755-757.

J. J. Lopez, et al. (2020). "TRPC Channels in the SOCE Scenario." Cells **9**(1).

E. A. Lumpkin and M. J. Caterina (2007). "Mechanisms of sensory transduction in the skin." Nature **445**(7130): 858-865.

R. Ma, et al. (2020). "Structural basis for diamide modulation of ryanodine receptor." Nat Chem Biol **16**(11): 1246-1254.

D. H. Marxhall, et al. (1976). "Calcium, phosphorus and magnesium requirement." Proc Nutr Soc **35**(2): 163-173.

C. Mathes (2007). "CRACking ion channel targets: 2nd annual Ion Channel Targets Conference. 12-13 September 2006, Boston, MA, USA." Expert Opin Ther Targets **11**(1): 101-104.

E. A. Matthews and D. Dietrich (2015). "Buffer mobility and the regulation of neuronal calcium domains." Front Cell Neurosci **9**: 48.

F. Maule, et al. (2016). "Annexin 2A sustains glioblastoma cell dissemination and proliferation." Oncotarget **7**(34): 54632-54649.

M. Mazumder, et al. (2014). "Prediction and analysis of canonical EF hand loop and qualitative estimation of Ca(2)(+) binding affinity." PLoS One **9**(4): e96202.

S. M. McMahon and M. B. Jackson (2018). "An Inconvenient Truth: Calcium Sensors Are Calcium Buffers." Trends Neurosci **41**(12): 880-884.

L. Y. M. Michel, et al. (2014). "Function and regulation of the Na+-Ca2+ exchanger NCX3 splice variants in brain and skeletal muscle." J Biol Chem **289**(16): 11293-11303.

J. Mishra, et al. (2017). "The Mitochondrial Ca(2+) Uniporter: Structure, Function, and Pharmacology." Handb Exp Pharmacol **240**: 129-156.

G. R. Monteith, et al. (2017). "The calcium-cancer signalling nexus." Nat Rev Cancer **17**(6): 367-380.

C. Moreno and L. Vaca (2011). "SOC and now also SIC: store-operated and store-inhibited channels." IUBMB Life **63**(10): 856-863.

S. E. Murthy, et al. (2018). "OSCA/TMEM63 are an Evolutionarily Conserved Family of Mechanically Activated Ion Channels." Elife **7**.

K. Nakatani, et al. (2002). "Calcium diffusion coefficient in rod photoreceptor outer segments." Biophys J **82**(2): 728-739.

S. Nakayama and R. H. Kretsinger (1994). "Evolution of the EF-hand family of proteins." Annu Rev Biophys Biomol Struct **23**: 473-507.

G. K. Natarajan, et al. (2021). "LETM1: A Single Entity With Diverse Impact on Mitochondrial Metabolism and Cellular Signaling." Front Physiol **12**: 637852.

T. R. Neelands, et al. (2000). "Functional expression of L-, N-, P/Q-, and R-type calcium channels in the human NT2-N cell line." J Neurophysiol **84**(6): 2933-2944.

B. Nilius, et al. (2011). "Irritating channels: the case of TRPA1." J Physiol **589**(Pt 7): 1543-1549.

Y. Pankratov and U. Lalo (2014). "Calcium permeability of ligand-gated Ca2+ channels." Eur J Pharmacol **739**: 60-73.

T. Parpaite and B. Coste (2017). "Piezo channels." Curr Biol **27**(7): R250-R252.

S. Patel and X. Cai (2015). "Evolution of acidic Ca(2)(+) stores and their resident Ca(2)(+)-permeable channels." Cell Calcium **57**(3): 222-230.

M. Patron, et al. (2013). "The mitochondrial calcium uniporter (MCU): molecular identity and physiological roles." J Biol Chem **288**(15): 10750-10758.

P. Pinton, et al. (1998). "The Golgi apparatus is an inositol 1,4,5-trisphosphate-sensitive Ca2+ store, with functional properties distinct from those of the endoplasmic reticulum." EMBO J **17**(18): 5298-5308.

P. Pizzo, et al. (2011). "Ca(2+) signalling in the Golgi apparatus." Cell Calcium **50**(2): 184-192.

N. Prevarskaya, et al. (2010). "Ion channels and the hallmarks of cancer." Trends Mol Med **16**(3): 107-121.

A. Raffaello, et al. (2016). "Calcium at the Center of Cell Signaling: Interplay between Endoplasmic Reticulum, Mitochondria, and Lysosomes." Trends Biochem Sci **41**(12): 1035-1049.

I. S. Ramsey, et al. (2006). "An introduction to TRP channels." Annu Rev Physiol **68**: 619-647.

S. Ringer (1883). "A further Contribution regarding the influence of the different Constituents of the Blood on the Contraction of the Heart." J Physiol **4**(1): 29-42 23.

G. Santoni, et al. (2012). "Functional role of T-type calcium channels in tumour growth and progression: prospective in cancer therapy." Br J Pharmacol **166**(4): 1244-1246.

J. Schittenhelm, et al. (2009). "Comparative analysis of annexin-1 in neuroepithelial tumors shows altered expression with the grade of malignancy but is not associated with survival." Mod Pathol **22**(12): 1600-1611.

B. Schwaller (2010). "Cytosolic Ca2+ buffers." Cold Spring Harb Perspect Biol **2**(11): a004051.

B. Shabnam, et al. (2018). "Sorcin a Potential Molecular Target for Cancer Therapy." Transl Oncol **11**(6): 1379-1389.

Z. X. Shi, et al. (2015). "Modeled microgravity suppressed invasion and migration of human glioblastoma U87 cells through downregulating store-operated calcium entry." Biochem Biophys Res Commun **457**(3): 378-384.

Y. Shono, et al. (2010). "Change in intracellular pH causes the toxic Ca2+ entry via NCX1 in neuron- and glia-derived cells." Cell Mol Neurobiol **30**(3): 453-460.

M. Song, et al. (2014). "The TRPC channel blocker SKF 96365 inhibits glioblastoma cell growth by enhancing reverse mode of the Na(+) /Ca(2+) exchanger and increasing intracellular Ca(2+)." Br J Pharmacol **171**(14): 3432-3447.

N. C. Strynadka and M. N. James (1989). "Crystal structures of the helix-loop-helix calcium-binding proteins." Annu Rev Biochem **58**: 951-998.

K. Takenaga, et al. (2007). "Modified expression of Mts1/S100A4 protein in C6 glioma cells or surrounding astrocytes affects migration of tumor cells in vitro and in vivo." Neurobiol Dis **25**(3): 455-463.

A. Takeuchi, et al. (2015). "The destiny of Ca(2+) released by mitochondria." J Physiol Sci **65**(1): 11-24.

E. F. Talarico, Jr. and N. J. Mangini (2007). "Alternative splice variants of plasma membrane calcium-ATPases in human corneal epithelium." Exp Eye Res **85**(6): 869-879.

J. L. Thompson and T. J. Shuttleworth (2013). "Molecular basis of activation of the arachidonate-regulated Ca2+ (ARC) channel, a store-independent Orai channel, by plasma membrane STIM1." J Physiol **591**(14): 3507-3523.

Tianhua Feng, et al. (2018). "L-type calcium channels: structure and functions." Ion Channels in Health and Sickness **77305**.

R. W. Tsien and R. Y. Tsien (1990). "Calcium channels, stores, and oscillations." Annu Rev Cell Biol **6**: 715-760.

K. Venkatachalam, et al. (2015). "The role of TRPMLs in endolysosomal trafficking and function." Cell Calcium **58**(1): 48-56.

A. Verkhratsky and A. Shmigol (1996). "Calcium-induced calcium release in neurones." Cell Calcium **19**(1): 1-14.

F. Vinberg and V. J. Kefalov (2018). "Investigating the Ca(2+)-dependent and Ca(2+)-independent mechanisms for mammalian cone light adaptation." Sci Rep **8**(1): 15864.

A. Visa, et al. (2019). "T-Type Cav3.1 Channels Mediate Progression and Chemotherapeutic Resistance in Glioblastoma." Cancer Res **79**(8): 1857-1868.

R. Wong, et al. (2020). "Inhibition of TRPM7 with waixenicin A reduces glioblastoma cellular functions." Cell Calcium **92**: 102307.

R. Wong, et al. (2017). "Activation of TRPM7 by naltriben enhances migration and invasion of glioblastoma cells." Oncotarget **8**(7): 11239-11248.

Wu Y, et al. (2021). "Lysosomal Calcium Channels in Autophagy and Cancer." Cancers **13(6): 1299**.

L. Xiao, et al. (2020). "Enzyme-digested Colla Corii Asini (E'jiao) accelerates wound healing and prevents ultraviolet A-induced collagen synthesis decline and wrinkle formation in three-dimensional skin equivalents." Hum Cell **33**(4): 1056-1067.

Z. Xu, et al. (2016). "Transport of Calcium Ions into Mitochondria." Curr Genomics **17**(3): 215-219.

Z. Yan, et al. (2013). "Drosophila NOMPC is a mechanotransduction channel subunit for gentle-touch sensation." Nature **493**(7431): 221-225.

J. Yang, et al. (2019). "Release and uptake mechanisms of vesicular Ca(2+) stores." Protein Cell **10**(1): 8-19.

Y. Zhang, et al. (2012). "Inhibition of T-type Ca(2)(+) channels by endostatin attenuates human glioblastoma cell proliferation and migration." Br J Pharmacol **166**(4): 1247-1260.

Y. Zhou, et al. (2013). "Calciomics: integrative studies of Ca2+-binding proteins and their interactomes in biological systems." Metallomics **5**(1): 29-42.

Acknowledgements

First and foremost I am extremely grateful to my supervisors, Prof. Vincent Torre for his invaluable advice, continuous support, and patience during my PhD study. His immense knowledge and plentiful experience have encouraged me in all the time of my academic research and daily life. It is also necessary to appreciate the help from my co-supervisor, Dan Cojoc.

I would also like to thank the people who helped and worked along with me during my PhD life, Fabio Falleroni, Ulisse Bocchero, Simone Mortal, et al.

Finally, I would like to express my gratitude to my parents, my wife and my son. Without their tremendous understanding and encouragement in the past few years, it would be impossible for me to complete my study.